A FIELD-WISE WIND RETRIEVAL ALGORITHM FOR SEAWINDS

by

Stephen L. Richards

A thesis submitted to the faculty of

Brigham Young University

in partial fulfillment of the requirements for the degree of

Master of Science

Department of Electrical and Computer Engineering

Brigham Young University

August 1999

BRIGHAM YOUNG UNIVERSITY

GRADUATE COMMITTEE APPROVAL

of a thesis submitted by

Stephen L. Richards

This thesis has been read by each member of the following graduate committee and by majority vote has been found to be satisfactory.

Date	David Long, Chair
Date	Brian Jeffs
Date	Lee Swindlehurst

BRIGHAM YOUNG UNIVERSITY

As chair of the candidate's graduate committee, I have read the thesis of Stephen L. Richards in its final form and have found that (1) its format, citations, and bibliographical style are consistent and acceptable and fulfill university and department style requirements; (2) its illustrative materials including figures, tables, and charts are in place; and (3) the final manuscript is satisfactory to the graduate committee and is ready for submission to the university library.

Date

David Long
Chair, Graduate Committee

Accepted for the Department

Michael D. Rice
Graduate Coordinator

Accepted for the College

Douglas M. Chabries
Dean, College of Engineering and Technology

ABSTRACT

A FIELD-WISE WIND RETRIEVAL ALGORITHM FOR SEAWINDS

Stephen L. Richards

Department of Electrical and Computer Engineering

Master of Science

In the spring of 1999 NASA will launch the scatterometer *SeaWinds*, beginning a 3 year mission to measure the ocean winds. SeaWinds is different from previous spaceborne scatterometers in that it employs a rotating pencil-beam antenna as opposed to fixed fan-beam antennas. The scanning beam provides greater coverage but causes the wind retrieval accuracy to vary across the swath. This thesis develops a field-wise wind retrieval algorithm to improve the overall wind retrieval accuracy for use with SeaWinds data.

In order to test the field-wise wind retrieval algorithm, methods for simulating wind fields are developed. A realistic approach interpolates the NASA Scatterometer (NSCAT) estimates to fill a SeaWinds swath using optimal interpolation along with linear wind field models.

The two stages of the field-wise wind retrieval algorithm are field-wise estimation and field-wise ambiguity selection. Field-wise estimation is implemented using a 22 parameter Karhunen-Loeve (KL) wind field model in conjunction with a maximum likelihood objective function. An augmented multi-start global optimization is developed which uses information from the point-wise estimates to aid in a global search of

the objective function. The local minima in the objective function are located using the augmented multi-start search techniques and are stored as field-wise ambiguities

The ambiguity selection algorithm uses a field-wise median filter to select the field-wise ambiguity closest to the true wind in each region. Point-wise nudging is used to further improve the field-wise estimate using information from the point-wise estimates. Combined, these two techniques select a good estimate of the wind 95% of the time.

The overall performance of the field-wise wind retrieval algorithm is compared with the performance of the current point-wise techniques. Field-wise estimation techniques are shown to be potentially better than point-wise techniques. The field-wise estimates are also shown to be very useful tools in point-wise ambiguity selection since 95.8%-96.6% of the point-wise estimates closest to the field-wise estimates are the correct aliases.

ACKNOWLEDGMENTS

This thesis would not have been possible without the help and support of many people. Specifically, I would like to thank Dr. David Long for his constant encouragement and insightful guidance during this research. Thanks to all the members of the MERS lab for wonderful memories and friendships. A special thanks to my dad who, at a very early age, instilled in me a love of science. Finally, this thesis is dedicated to my sweet wife, Rebekah, whose love and faith inspires me to be the best I can be. Thank you all.

Contents

List of Tables

List of Figures

Chapter 1

Introduction

In late spring 1999, NASA is scheduled to launch the first of a new generation of scatterometers called *SeaWinds* [1]. This marks the beginning of a 3 year mission to measure the near-surface ocean winds using the SeaWinds scatterometer. SeaWinds is the first operational spaceborne scatterometer to employ a scanning pencil-beam antenna. The pencil-beam design has many advantages but also offers unique challenges in estimating ocean winds. As a result of the new measurement geometry, current wind retrieval techniques may not be adequate and consequently improved methods for estimating the oceans winds are needed.

1.1 Motivation

Nearly 70% of the Earth's surface is covered by oceans. As a result, accurate ocean wind data is mandatory in better understanding the Earth's global climate. Unfortunately, this data is very hard to obtain. Currently, ships are used to measure the ocean winds but these measurements have poor global coverage and are prone to error. Ocean buoys have also been used to measure winds but are few in number and the resulting data is too sparse to be of use in studying global phenomena [2]. An alternative approach uses spaceborne radar systems which measure the roughness of the ocean. From these measurements we can indirectly infer the wind speed and direction. These systems are very valuable because they are unaffected by cloud cover and can provide global coverage in a matter of days.

The first extended test of spaceborne wind retrieval occured in 1978 when the scatterometer SASS was launched aboard the remote sensing satellite Seasat.

Unfortunately, there was a power failure 90 days into the mission; however, enough data was gathered to verify that ocean winds can be estimated using spaceborne radar data. In 1991 and 1995 the European Space Agency sponsored two remote sensing satellites which included scatterometers. The most recent scatterometer is the NASA Scatterometer (NSCAT) which went into space aboard the Japanese spacecraft ADEOS [2]. During its mission NSCAT supplied meteorological researchers with unprecedented amounts of ocean wind data. Tragically the NSCAT mission was cut short when the solar panel of the ADEOS spacecraft broke nine months into the mission.

As a replacement for NSCAT, the Jet Propulsion Laboratory (JPL) has designed and built a new scatterometer, SeaWinds. Unlike the previous scatterometers, which have employed fixed fan-beam antennas to measure the Earth's scattering properties, SeaWinds uses a rotating parabolic dish to scan the surface. The scanning pencil-beam has the advantages of being more compact and having a greater coverage area. However, as a result of the scanning beam the measurement geometry varies across the swath [1]. This can have adverse effects on the accuracy of wind estimation. For this reason, new wind estimation algorithms must be developed to improve the overall accuracy of SeaWinds ocean wind estimates.

1.2 Contributions

The purpose of this thesis is to develop a field-wise wind retrieval algorithm for SeaWinds. Field-wise wind retrieval uses the satellite σ^o measurements along with linear wind field models to estimate the wind on a field-wise scale. Outlined below are the contributions made to the field of scatterometer-based wind retrieval by this thesis.

The first contribution is a method for simulating the SeaWinds data sets which are later used to evaluate the algorithm performance. The most realistic form of simulated wind is found by interpolating NSCAT wind estimates. NSCAT winds offer realistic wind features but cover a smaller swath and contain missing data points within the swath due to calibration cycles and gridding errors. In order to map the

wind to the larger SeaWinds swath the wind must be interpolated. For this purpose, an optimal interpolation technique is developed using the autocorrelation of the wind and model fit to the data. Using this interpolation two different forms of simulated wind are created.

The next contribution is the extension and optimization of field-wise estimation [3] to the SeaWinds geometry. The linear wind field models used in [3] are enlarged to cover a 24×24 wind vector cell area. For these large models, the maximum likelihood objective function is shown to the best estimator for SeaWinds wind estimates and the augmented multi-start search is shown to provide the best method for searching the objective function. The wind field model providing the best trade-off between modeling accuracy and computational complexity for use in field-wise estimation is shown to the be the 22 parameter Karhunen-Loeve (KL) model.

A new field-wise ambiguity selection algorithm is developed to select the wind field that corresponds to the true winds. To do this a field-wise median filter, modeled after the point-wise median filter, is developed. A point-wise nudging technique which uses information in the point-wise estimates is also developed to further improve the results of the field-wise median filter. The point-wise estimates are generated using the same point-wise estimation used for NSCAT. Based on a test case of 1060 wind field regions, the ambiguity selection algorithm has a selection accuracy of 95%.

Lastly, the field-wise estimation algorithm and the field-wise ambiguity selection algorithm are combined to form an end-to-end wind estimation algorithm, the performance of which is shown to be potentially superior to the current point-wise wind retrieval methods. The accuracy of the field-wise estimates is a function of the simulated wind variability and the performance of the ambiguity selection step. The field-wise estimates are also shown to be a good point-wise ambiguity selection tool. Using interpolated NSCAT winds, 95.8% of the point-wise estimates closest to the field-wise estimates are the correct ambiguities. This percentage increases to 96.6% for modeled NSCAT winds.

1.3 Overview

This thesis is organized as follows. Chapter 2 provides a background for ocean wind estimation, describing the relationship between scatterometer measurements and the wind speed and direction. The differences between point-wise estimation and field-wise estimation are discussed and methods for implementing each type of wind estimation are described.

Chapter 4 describes in detail the field-wise estimation process for SeaWinds data. Here different estimation techniques are explored and the optimal methods are determined. The result of the wind estimation process is a set of possible wind estimates for each region of wind vector cells.

Chapter 5 develops an ambiguity selection algorithm for selecting the closest estimate from the set of possible wind fields in each region. This method uses a field-wise median filter in conjunction with a point-wise nudging process to select the aliases closest to the true wind.

Chapter 6 describes the end-to-end field-wise wind retrieval algorithm developed using the results of Chapter 4 and Chapter 5 and tests it on several simulated data sets. The results are then compared to the point-wise results.

Chapter 7 contains a final summary and conclusions along with suggestions for future work.

Chapter 2

Background

This chapter provides a brief tutorial on the fundamental principles behind scatterometry and current wind retrieval methods. First, a description of the class of radars known as scatterometers is given. Next, the relationship between the measurements taken by scatterometers (σ^o) and the wind speed and direction is discussed. The current methods used in estimating the wind speed and direction from scatterometer σ^o measurements for both the point-wise and field-wise cases are given. Finally, a brief overview of NASA's new instrument, SeaWinds, is given, considering both its strengths and weaknesses as they relate to wind retrieval.

2.1 Scatterometry

Remotely measuring the near-surface ocean winds requires a class of instruments known as scatterometers. A scatterometer is defined as a "radar that measures the scattering or reflective properties of surfaces and/or volumes" [4]. Specifically, the scattering property measured is the normalized radar cross section, given the symbol σ^o. Figure 2.1 shows a typical system geometry for a scatterometer. The antenna transmits a radar signal at an incidence angle, θ, to the surface. The amount of backscattered power is a function of the roughness of the surface. The more rough the surface, the more power that is scattered back to the antenna. The relationship between the the power transmitted, P_t, the power received, P_r, and σ^o is given by the radar equation [4]

$$\sigma^o = \frac{(4\pi)^3 R^4 L P_r}{P_t G^2 \lambda^2 A_{eff}}, \tag{2.1}$$

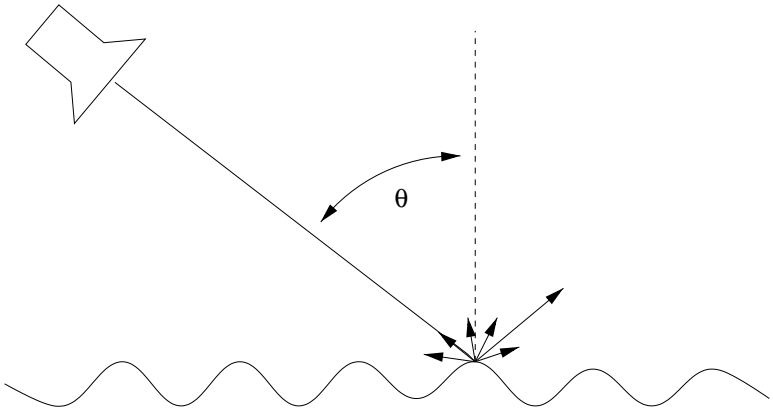

Figure 2.1: *A scatterometer transmits a radar beam incident to the surface at an angle θ. The amount of radiation reflected back to the antenna is related to the roughness of the surface*

where R is the range to the surface, L is the system loss, G is the gain of the antenna, λ is the wavelength and A_{eff} is the effective area of the antenna. From this equation it is apparent that the value of σ^o is essentially the ratio of the power returned (adjusted for spreading loss) and the power transmitted. While not explicitly given it is also important to note that σ^o varies with θ.

2.2 The Relationship Between Wind and σ^0

For σ^o to be of value in estimating the surface wind speeds and directions there must be a well defined relationship between the two. This relationship was first noticed during World War II when scanning radars were first placed on naval ships and the radar operators noticed that the amount of sea clutter was a function of the wind speed [5]. After the war scientists working for the Naval Research Lab and at Kansas University began to study in detail the effect of near-surface winds on σ^o.

The result of this research has been the development of the geophysical model function (GMF) which relates the wind to values of σ^o. The GMF is an empirical nonlinear model usually designated as

$$\sigma^o = \mathcal{M}(U, \chi, \theta, f, \text{pol}). \tag{2.2}$$

Thus, σ^o is a function of wind speed, U, relative direction, χ (the angle between the wind direction and the look direction of the scatterometer), instrument incidence angle, θ, frequency, f, and polarization (either vertical or horizontal). While many other factors effect the relationship between wind and σ^o such as ocean salinity, temperature, atmospheric absorption etc., these factors are not well understood. Hence they are ignored and any resulting inaccuracies are treated as geophysical modeling noise.

Figure 2.2 shows two plots of σ^o as a function of wind direction for wind speeds of 5, 10 and 15 m/s. The plot on the left is for a vertically polarized radar while the plot on the right is the result of a horizontally polarized radar. In these two plots the $\cos(2\chi)$ nature of the GMF is very evident. This general structure of the GMF is due to the symmetry of the wind driven waves. Figure 2.3 illustrates a simplistic model of ocean waves. As the wind blows, ridges form perpendicular to the wind direction. For a scatterometer looking head on into these waves the returned power is greater than for the case where the instrument is rotated 90° and looking down the trough. Thus, there is a high value of σ^o at a relative azimuth of 0° and a minimum at 90°. Because the waves are nearly symmetrical this pattern is repeated for relative azimuths of 180° and 270°, though the peak at 180° is slightly smaller.

Over the years several different model functions have been developed as this relationship has become better understood through experimentation. The most recent Ku-band GMF to be developed, the one currently in use, is the NSCAT2 model function [6].

2.3 Estimating the Wind

Wind retrieval or wind estimation is the process of inverting the geophysical model function to determine the wind speed and direction that caused the measured value of σ^o. From Figure 2.4 it is evident that there are an infinite number of possible winds that could have generated this value of σ^o. To determine the correct wind, multiple measurements must be taken at different relative azimuth angles and the point of intersection is at the true wind speed and direction (see Figure 2.5).

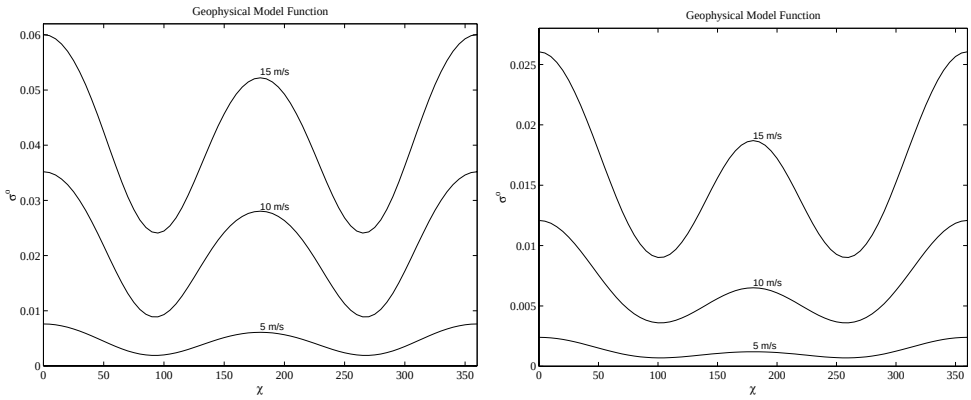

Figure 2.2: *Plots of the geophysical model function (GMF). The plot on the left is the GMF for a vertically polarized radar beam while the plot on the right is for a horizontally polarized beam. These two plots illustrate the* $\cos(2\chi)$ *nature of the GMF which is due to the near symmetry of the ocean waves.*

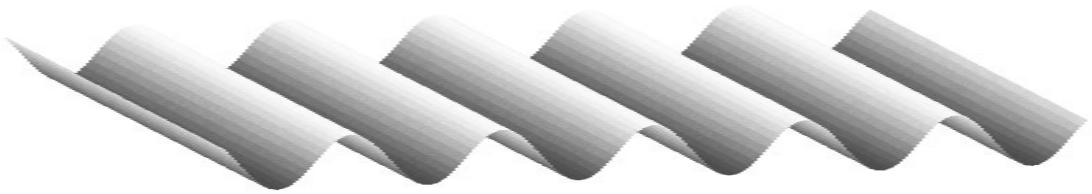

Figure 2.3: *Idealized waves formed by wind blowing across the surface of the ocean.*

Wind estimation as described above would be easy to implement if the measured values of σ^o were noiseless. However, the noise associated with measuring σ^o blurs the GMF curves creating several possible intersections between the different measurements as in Figure 2.6. Wind estimation is thus an ill-posed problem, meaning that the mapping from σ^o to wind is a many-to-one mapping. Statistical tools must be used to choose the most probable wind from the set of choices. The possible wind vectors are known as ambiguities or aliases and there can be anywhere from 2 to 6 ambiguities for each wind vector cell. The noise model used to estimate the noise in σ^o is described in greater detail below [7].

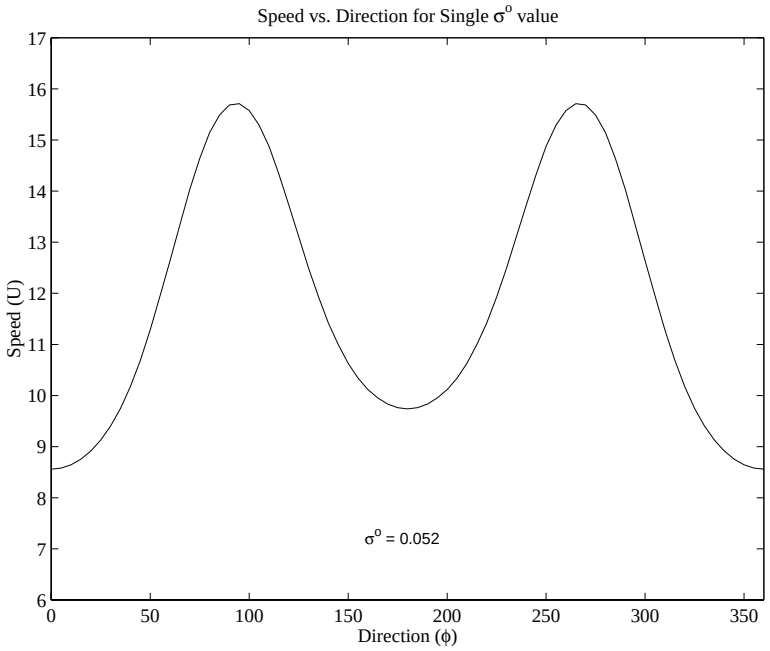

Figure 2.4: *For a single measurement of σ^o there are an infinite number of combinations of wind speeds and directions that could correspond to σ^o. This ambiguity requires multiple measurement to be take in order estimate the wind. This σ^o was obtained using $\theta = 40°$ and vertical polarization.*

2.3.1 Noise Model

Figure 2.7 shows the true wind passed through the geophysical model function to generate the estimate σ^o_m. The observed σ^o_T values vary from the ideal because of inaccuracies in the GMF and this variation is treated as a zero mean Gaussian noise distribution with the variance determined by K_{PM} as follows

$$\sigma^o_m = \mathcal{M} \cdot (1 + K_{PM}\nu_1), \tag{2.3}$$

with $\mathcal{M}$ representing the GMF estimate of σ^o (note that the explicit reference to θ, U, χ and so forth, have been dropped), and ν is a zero mean unit variance random variable. Communication noise is added when the observed σ^o_T is measured by the instrument. This noise is better understood and is a zero mean Gaussian distribution. The normalized standard deviation of the noise is denoted K_{PC} and is computed using the noise parameters α, β and γ, which are estimated when the measurements

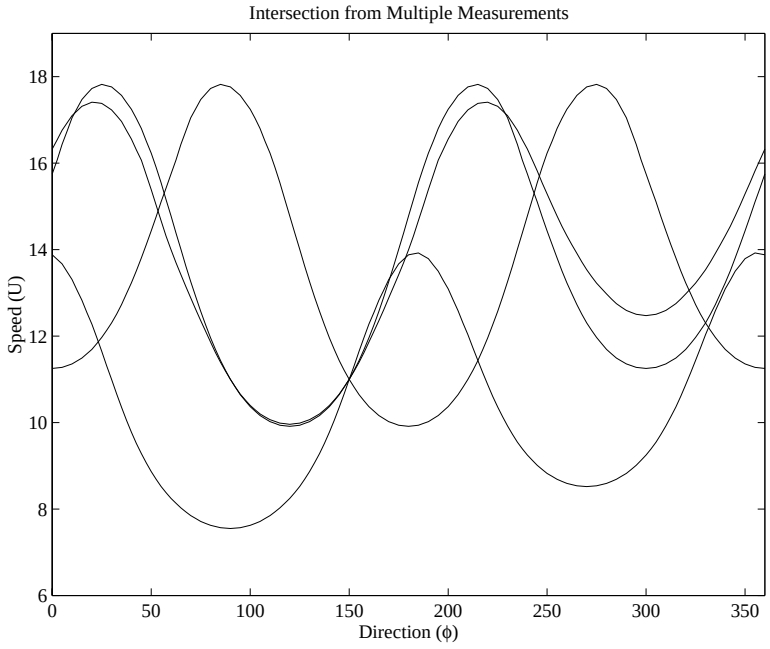

Figure 2.5: *Using multiple measurements the true wind speed and direction can be found using the intersection of the curves resulting from each measurement. Here the true wind is 11 m/s at* $150°$.

are taken. Using these parameters,

$$K_{PC}^2 = \alpha + \frac{\beta}{\sigma_T^o} + \frac{\gamma}{\sigma_T^{o\,2}}. \tag{2.4}$$

The final variance for the noise using both K_{PM} and K_{PC} is

$$\varsigma^2 = \epsilon \mathcal{M}^2 + (1 + K_{PM}^2)(\beta \mathcal{M} + \gamma), \tag{2.5}$$

where

$$\epsilon = \alpha + K_{PM}^2 + \alpha K_{PM}^2. \tag{2.6}$$

While K_{PM} effects the measurements and consequently our estimate of the wind, it is not well understood [8]. As a result, the simulations performed in this thesis treat K_{PM} as negligible and set it to zero. Thus, measurement variance is

$$\varsigma^2 = \alpha \mathcal{M}^2 + \beta \mathcal{M} + \gamma. \tag{2.7}$$

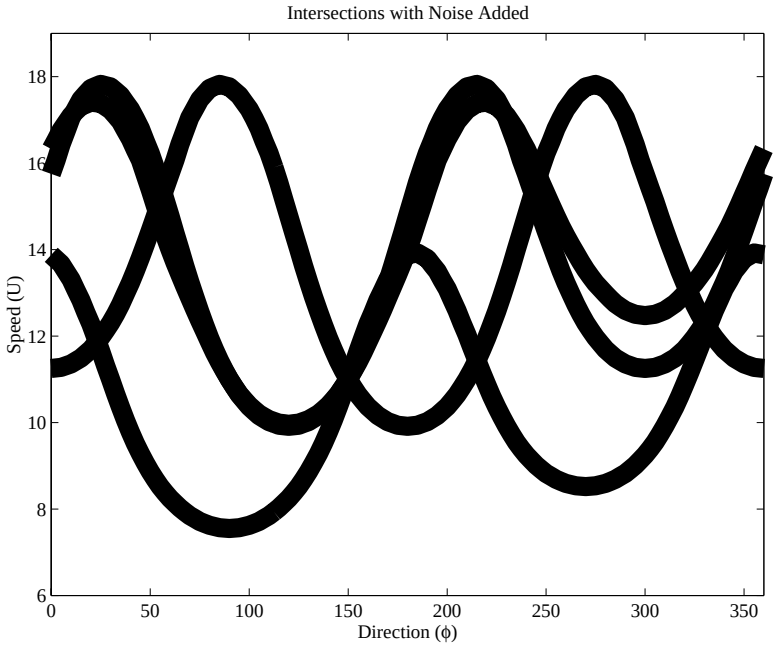

Figure 2.6: *With noise added there are now several possible intersections between the curves. This results in several possible wind aliases or ambiguities.*

Due to noise, all forms of wind retrieval have two fundamental steps. The first step is wind estimation which calculates all the aliases for a given location. Once the aliases are generated an ambiguity removal step is required to estimate which ambiguity corresponds to the correct wind speed and direction.

There are also two different approaches to wind estimation. Point-wise estimation is the oldest method and is based on determining the wind at a single wind vector cell independent of the σ^o measurements in adjacent cells. More recently methods have been developed to perform field-wise estimation which assumes a correlation between each wind vector in a region or field of cells. The wind is then estimated for the entire field. Both of these estimation methods have their strengths and weaknesses as discussed below.

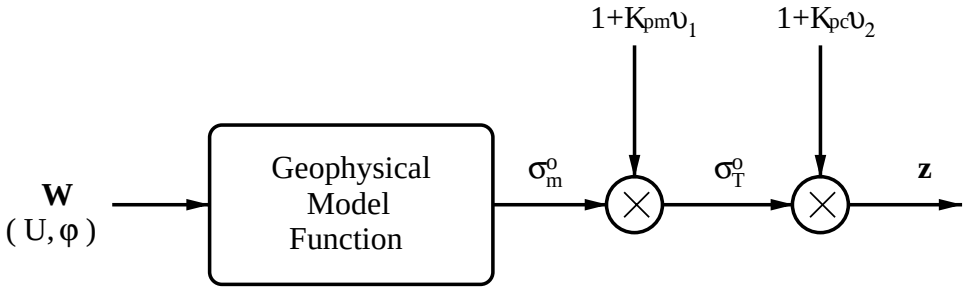

Figure 2.7: *A near-surface ocean wind roughens the water resulting in a value of σ^o predicted by the GMF and denoted, σ^o_m. This value of σ^o varies from the actual observed σ^o, denoted σ^o_T, by a Gaussian distribution with zero mean and standard deviation of K_{PM}. The measured σ^o is further distorted by communication noise which is again modeled as a Gaussian zero-mean distribution with standard deviation of K_{PC}. Thus the final measurement, z, is a noisy version of the wind generated σ^o.*

2.3.2 Point-Wise Estimation

As mentioned, point-wise estimation is based on calculating the wind for a single cell independent of the surrounding cells. The wind estimation step for point-wise retrieval is based on the maximum likelihood estimate where

$$\hat{\mathbf{w}} = \arg\max_{\mathbf{w}} p_{\mathbf{z}}(\mathbf{z}|\mathbf{w}). \tag{2.8}$$

To formulate the conditional probability, $p_{\mathbf{z}}, (\mathbf{z}|\mathbf{w})$ we refer back to the noise model for the measurements, z. From this model z is defined as a deterministic signal, σ^o_m with additive Gaussian noise of variance ς^2 defined in Eq. 2.5. Thus for a single measurement

$$p_z(z|\mathbf{w}) = \frac{1}{\varsigma_z\sqrt{2\pi}} \exp\left[\frac{-(z-\mathcal{M})^2}{2\varsigma_z^2}\right], \tag{2.9}$$

where $\mathbf{w} = [U, \phi]$ and $\mathcal{M}$ is shorthand for $\mathcal{M}(U, \chi, \theta, f, \text{pol})$. As mentioned before, multiple measurements must be used to uniquely define a wind vector. Using $\mathbf{z} = [z_1, z_2 \ldots z_K]$ and assuming the noise from each of the measurements is independent the the joint probability becomes

$$p_{\mathbf{z}}(\mathbf{z}|\mathbf{w}) = \prod_{k=1}^{K} \frac{1}{\varsigma_{z_k}\sqrt{2\pi}} \exp\left[\frac{-(z_k-\mathcal{M}_k)^2}{2\varsigma_{z_k}^2}\right]. \tag{2.10}$$

Here $p_{\mathbf{z}}(\mathbf{z}|\mathbf{w})$ is simply the product of Gaussian distributions with a mean of $\mathcal{M}_k$, and variance, $\varsigma^2_{\mathbf{z}_k}$. K is the number of measurements taken in each wind vector cell. In practice this objective function is implemented by minimizing the negative log-likelihood values.

The problem of ambiguities arises while optimizing the objective function, $p_{\mathbf{z}}(\mathbf{z}|\mathbf{w})$. As a result of noise, the relative amplitude of each local minimum of the objective function yields very little information. Therefore, instead of choosing the global minimum to represent the true wind, each local minimum is selected as a possible alias. The aliases are then sorted according to objective function value and saved until one is chosen to represent the true wind during the ambiguity removal step. It is also worth noting that it is common practice to refer to each alias by its rank, with the first alias corresponding to the highest objective function value, the second alias corresponding to the next highest value and so on.

Figure 2.8 illustrates the point-wise objective function. The objective function values are plotted versus the u and v rectangular components of the wind. Note that the minima lie in a circle of constant radius. One of the valuable aspects of the point-wise estimate is that the speeds for all the aliases are generally close to the true speed, the ambiguity is in determining the direction of the wind. This point-wise speed accuracy is exploited in subsequent chapters.

The final step in point-wise wind retrieval is ambiguity removal. The purpose of ambiguity removal is to select the most likely alias from the set of aliases generated during the estimation step. Ambiguity removal can be thought of as putting a puzzle together with each alias in each cell being a possible piece of the puzzle. The goal is to choose the aliases so that the final wind field best matches the true wind field. The tool used by JPL in processing scatterometer data is median filter based ambiguity removal [9]. This median filter is based on the principle of choosing the wind alias that minimizes the error between it and the wind vectors in a window surrounding it. The implementation of the median filter for a 7×7 wind vector cell window centered

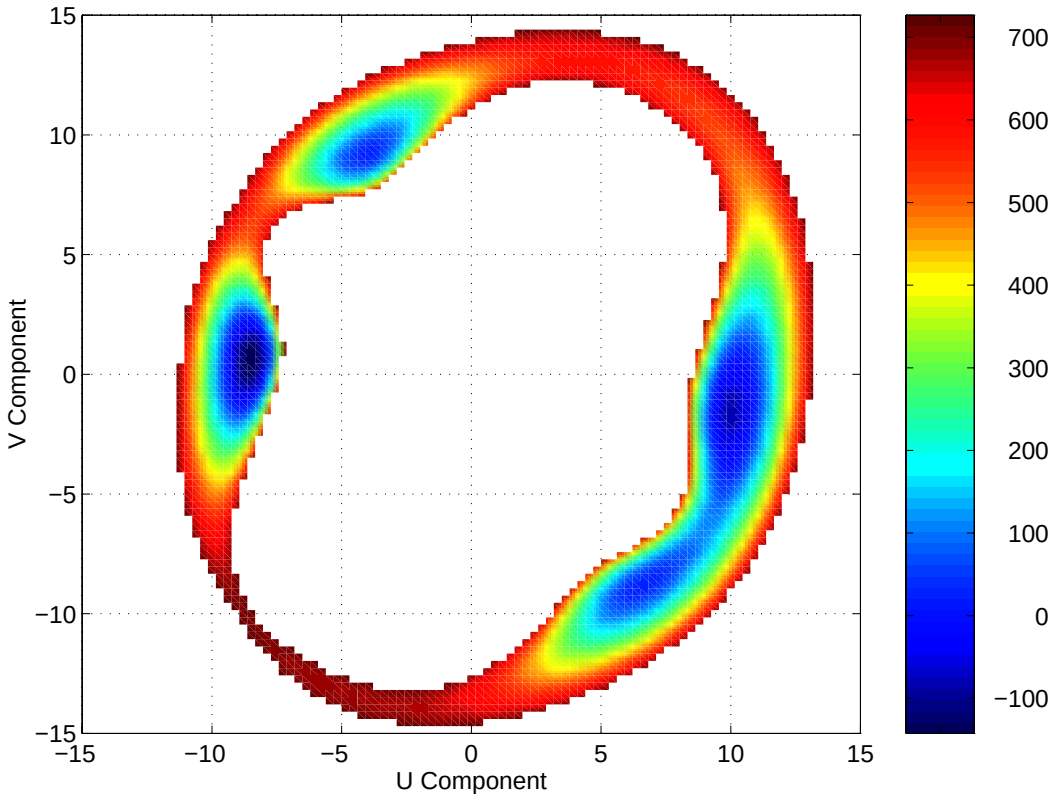

Figure 2.8: *An example of the point-wise objective function. Note that the minima lie in circle of constant speed, the wind ambiguity is primarily in the direction.*

at (i, j) is

$$\hat{n} = \arg\min_{n} \sum_{m=i-3}^{i+3} \sum_{m=j-3}^{j+3} ||w_{ij}^{n} - U_{mn}|| \tag{2.11}$$

where U_{mn} are the surrounding wind vectors and the resulting selected wind alias is $w_{ij}^{\hat{n}}$. This method takes advantage of the fact that the wind is correlated from one cell to the next and the difference in wind direction from cell to cell should be quite small.

To implement the median filter on a wind field the field must first be initialized. Most often the wind field is initialized to all the first aliases since the first alias is most likely the correct one. Once the field is initialized, a median filter is run for each cell in the field and the number of vectors that change is recorded. This process is then iterated until either no vectors change or a very small number of them do, ensuring that the chosen ambiguities form the best fitting wind field.

Point-wise wind retrieval is good for several reasons. First, the point-wise estimates are very accurate. There is almost always an alias that is close to the true wind. Perhaps one of the greatest advantages of point wise retrieval is that it is not computationally intensive, meaning that algorithms and software can process data very quickly. The single biggest shortcoming of point-wise retrieval is the ambiguity removal step. The median filter approach is only successful if a significant majority of the initial aliases correspond to the true wind [10].

2.3.3 Field-Wise Estimation

Field-wise wind retrieval is similar to point-wise retrieval in many ways but is done on a much larger scale. Instead of calculating the wind for a single location at a time, wind field estimates are generated for an entire region. This approach takes advantage of the fact that there is some correlation in the wind from cell to cell within the region.

To take advantage of the correlation, wind field models are employed. For this reason, field-wise estimation is also referred to as model-based estimation. Linear wind field models were first developed by Long [11] and have since been extended by

Oliphant [7]. These linear wind field models are of the form

$$W = FX \tag{2.12}$$

where, W, is the wind field vector, F, is the model matrix and X is the vector of model parameters. To form the wind vector a $M \times N$ wind field is converted into rectangular coordinates u, v from the polar coordinates U, ϕ_c (ϕ_c is the wind direction converted from the oceanographic convention, which is relative to north, to the conventional coordinates which is relative to the satellite sub-track). The u component points in the cross-track direction and v points in the along-track direction and are defined below:

$$u = U\cos(\phi_c), \tag{2.13}$$

$$v = U\sin(\phi_c). \tag{2.14}$$

The $2MN$ long wind vector is now defined as

$$W = \begin{bmatrix} U \\ V \end{bmatrix} \tag{2.15}$$

where U and V are MN length column scanned vectors of u and v from the $M \times N$ region.

Several different wind field models have been developed, each based on different principles. The first models developed was the Parameterized Boundary Conditions (PBC) model based on physical properties of the wind, such as curl and divergence [11]. Other model have been made based on Fourier and Legendre polynomials [7]. The model used in this paper is the Karhunen-Loeve (KL) model originally used by Oliphant [7]. The KL model is a data driven model formed by taking the eigenvectors of the autocorrelation of the wind. The autocorrelation matrix of the wind is approximated using the sample average of the wind for L different regions:

$$R = E[WW^T], \tag{2.16}$$

$$\approx \frac{1}{L}\sum_{n=1}^{L} W_n W_n^T. \tag{2.17}$$

The KL model is then formed using an eigenvalue decomposition with

$$RF = F\Lambda. \tag{2.18}$$

The columns of F are the eigenvectors of R and are ordered to correspond with the eigenvalues which are sorted in descending order. This assures that the basis vectors are sorted to minimize the basis restriction error when truncating the model.

The KL model has become the model of choice for several reasons. The first reason is that the basis vectors of the KL model are orthonormal. This is important because each model parameter is independent of the others. Probably the most important reason is that the KL model is optimal in terms of minimizing basis restriction error. This means that in truncating the model the maximum energy is contained in the retained basis vectors [12]. For the KL model each column is a basis vector and corresponds to a basis wind field. Figures 2.9 and 2.10 illustrate the first 12 basis fields of a 24×24 KL model. The first two basis fields are the mean wind fields and the others display curl and divergence fields. Combined, the full set of basis fields can represent any wind field.

Using wind field models, the wind is estimated for a $M \times N$ region in a fashion similar to the point-wise case. That is, an objective function based on the wind field and the σ^o measurements over that field is optimized. Again, this is typically done using a maximum likelihood estimator. Thus, the estimated wind field is

$$\hat{W} = \arg\max_{W} p_Z(Z|W). \tag{2.19}$$

To reduce dimensionality a truncated model is used. Once the model parameters are estimated the wind field is reconstructed. The estimator then becomes

$$\hat{X} = \arg\max_{X} p_Z(Z|FX). \tag{2.20}$$

The conditional probability, $p_Z(Z|FX)$, is formed as a product of Gaussian distributions similar to the conditional for the point-wise case with the addition of multiplying over all the cells in the region. The conditional is computed as

$$\begin{aligned} p_Z(Z|FX) &= \prod_{l=1}^{MN} \prod_{k=1}^{K(l)} \frac{1}{\varsigma_{z_{k,l}}\sqrt{2\pi}} \exp\left[\frac{-(z_{k,l} - \mathcal{M}_{k,l})^2}{2\varsigma^2_{z_{k,l}}}\right], \\ \mathcal{M}_{k,l} &= \mathcal{M}(U_{k,l}, \chi_{k,l}, \theta_{k,l}, f_{k,l}, \mathrm{pol}_{k,l}). \end{aligned} \tag{2.21}$$

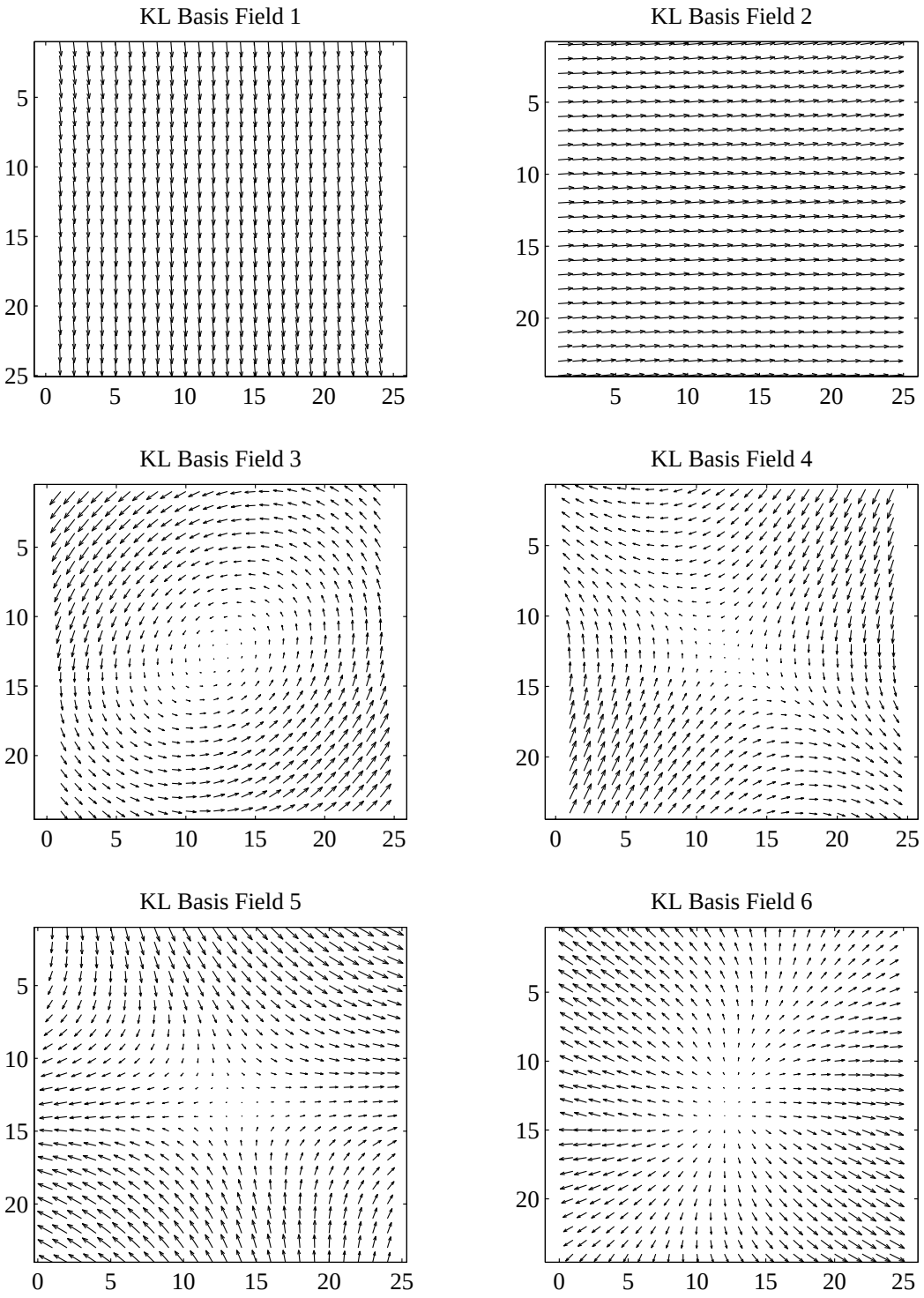

Figure 2.9: *The first six KL basis wind fields for a* 24×24 *region. Note that the first two wind fields determine the mean wind flow and every additional field adds more high frequency components. Model-based wind fields are simply linear combinations of these wind fields.*

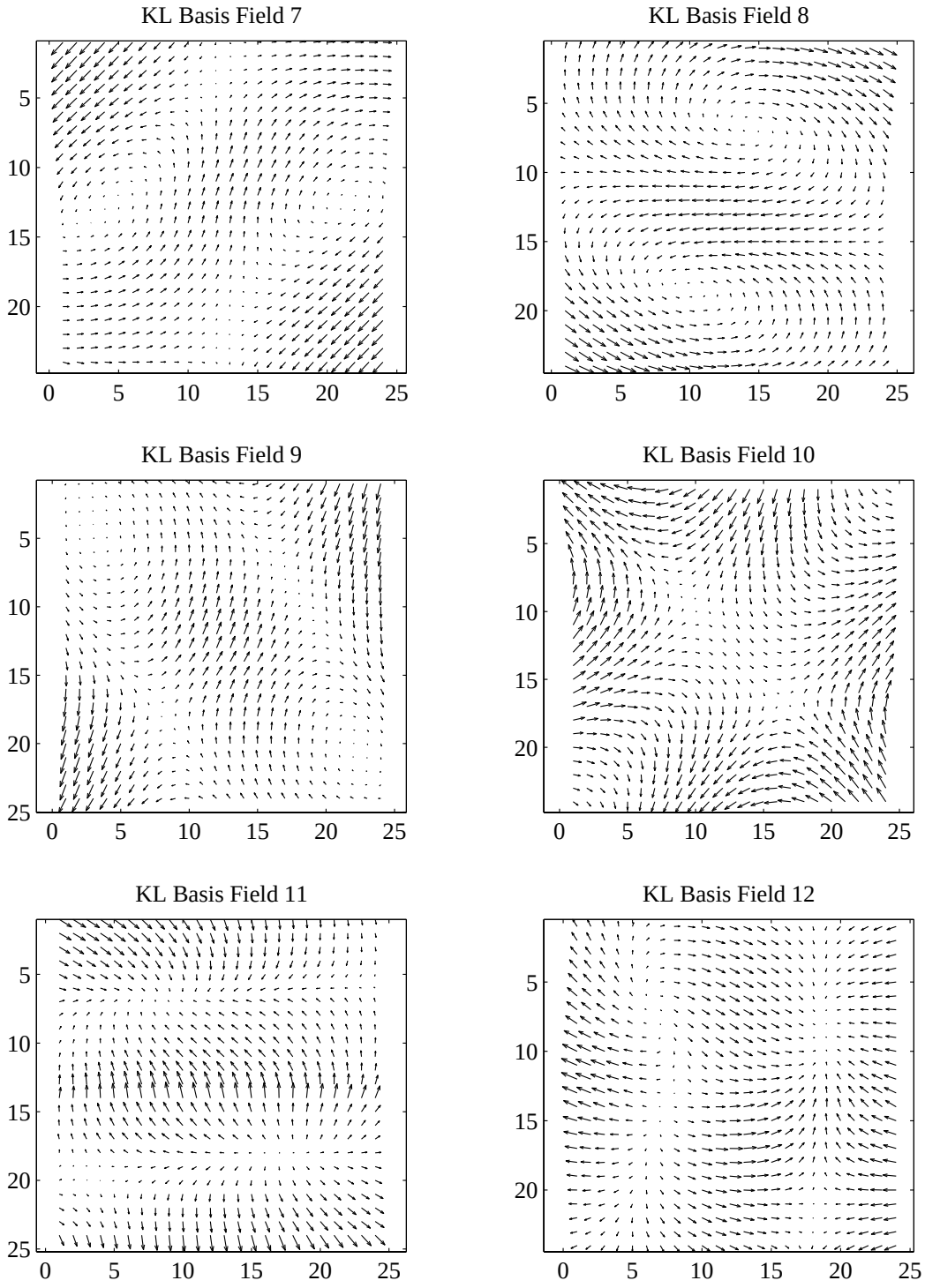

Figure 2.10: *The seventh through twelfth KL basis wind fields for a* 24×24 *region. These fields have more high frequency content than the previous six wind fields.*

In the above equation the connection to FX is not explicitly given, but $U_{k,l}$ and $\chi_{k,l}$ are the result of FX.

Like point-wise wind retrieval, the amplitude of the local extrema in the objective function can be misleading due to noise in the measurements and consequently all the minima must be calculated and retained. This creates field-wise ambiguities, which are entire wind fields that could correspond to the true wind. Figure 2.11 shows a wind field and the first three resulting field-wise aliases.

The primary advantage of field-wise estimation is that there are fewer field-wise ambiguities than there are possible combinations of point-wise ambiguities which should help to simplify the ambiguity selection step. Spatial overlap of the field can also be used to simplify ambiguity selection. One drawback to field-wise estimation is that it is very computationally intensive. Determining minima in the objective function requires a search through an N_X dimensional space where N_X is the length of the wind field parameter vector. For large N_X it is practically impossible to perform an exhaustive search on the objective function. For this reason, the ability to truncate the KL model with minimum basis restriction error adds to our ability to reduce the parameter vector size while only adding a small modeling error.

2.4 The Instrument: SeaWinds

The single biggest factor in determining the accuracy with which winds are retrieved is the design of the instrument measuring σ^o. Over the last several years NASA has developed several spaceborne scatterometers that have had great success. In the spring of 1999 the launch of a new generation of scatterometers is planned with SeaWinds going into space aboard the satellite Quikscat. The design of SeaWinds incorporates several new innovations which make it significantly different from past scatterometers. The most significant change is that SeaWinds uses a scanning pencil-beam antenna rather than fixed, fan beam antennas. This change has several effects on wind retrieval performance which are discussed in greater detail in this section.

Figure 2.12 shows the satellite geometry for SeaWinds. The two antenna beams are also shown in this figure. The outer beam is vertically polarized while

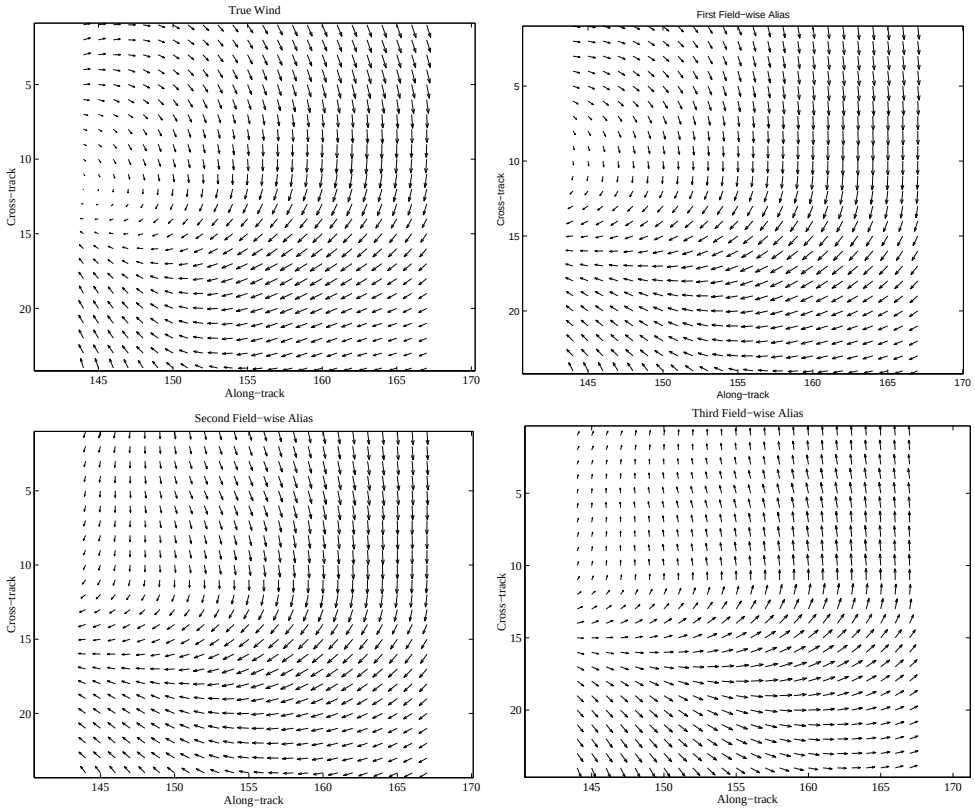

Figure 2.11: *The top left plot is a plot of the true wind and the remaining three plots are the first three field-wise aliases corresponding to this wind field. It appears that the first alias is the correct alias.*

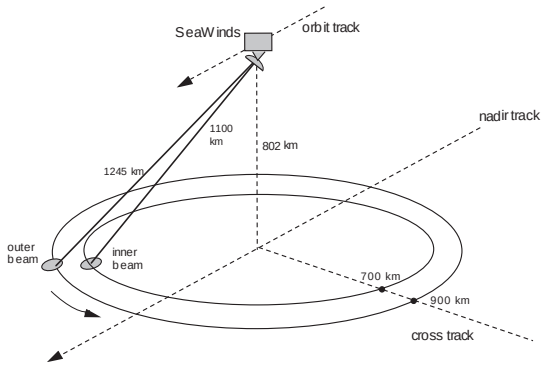

Figure 2.12: *The spacecraft and antenna geometries for SeaWinds on Quickscat.*

the inner beam is horizontally polarized. As the spacecraft flies over the earth the antenna dish rotates causing the beams to trace a helical pattern on the ground. The end effect is two continuous swaths of data, one from the inner beam and another from the outer beam. This rotating pencil-beam configuration offers many advantages over the fixed beams. One of these advantage is increased coverage area. The width of the swath created by the outer beam is 1800 km [1]. This is a 50% increase over the two 600 km swaths covered by NSCAT, NASA's previous scatterometer [2]. Greater swath width results in more rapid global coverage.

While a scanning beam allows for greater coverage there are also some distinct disadvantages when using it for wind retrieval. As mentioned before, previous space-borne scatterometers have fixed antenna beams to measure σ^o. The angles of these beams are optimized to ensure the best wind retrieval possible. For example, NSCAT has four fixed beams on each side which provided the different σ^o measurements over a range of 90° in azimuth. Three beams are vertically polarized and the forth is

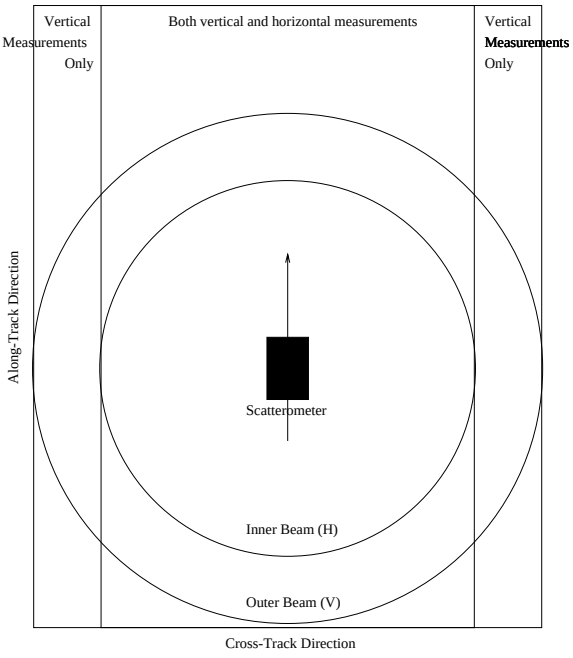

Figure 2.13: *A top view of the SeaWinds swath showing the two overlapping swaths from the inner and outer beam.*

horizontally polarized. Thus, for each cell there are at least four measurements with a minimum of 20° azimuth separation between them. As explained in section 2.3 (Figure 2.5), measurements must be taken at a variety of azimuth angles is necessary to pinpoint the true wind speed and direction.

Using a scanning beam, however, the azimuth separation between measurements varies across the swath. To illustrate this Figure 2.13 shows the two overlapping SeaWinds swaths. On the outer edges of the swath the measurements are only vertically polarized because the inner beam is smaller in circumference. More importantly the measurements in this area can only be taken when the antenna is pointing nearly perpendicular to the direction of travel. This means that all the σ^o values taken near the edges of the swath are close to 90° for the right hand side and 270° for the left hand side. This offers very little azimuth variation in the measurements making wind retrieval much more difficult.

A similar problem occurs in the very middle of the swath. Now the measurements are both vertically and horizontally polarized, but they can only be taken at 0° and 180°. Because of the symmetry in the GMF, measurements taken 180° apart are nearly identical and hence wind retrieval is poor in the sub-nadir region of the swath. Figure 2.14 shows two sets of measurements, one taken from the edge of the swath and the other from the center of the swath. In these two plots we see that the curves nearly line up for all speeds and directions. With noise added it is almost impossible to distinguish the true wind speed and direction. As a result of the varying geometries our ability to correctly estimate the wind also varies across the swath. This is best illustrated in Figure 2.15 which plots the RMS vector error between the closest point-wise alias and the true wind as a function of the distance across the swath. In this plot we see that the error is very high at the edges and in the middle of the swath. It is equally important to note that wind retrieval is quite good in the two regions on either side of the center. This portion of the swath is often referred to as the "sweet spot".

Unless a way is found to improve the wind retrieval in the low skill areas the size of the SeaWinds swath could be effectively limited to the size of the sweet spots (about the same size as an NSCAT swath). The primary purpose of this thesis is to combine model-based estimation with the current point-wise estimation techniques to create improved accuracy across the entire swath. With the use of model-based wind retrieval, the highly reliable wind estimates from the sweet spot can be extended to the sub-nadir and exterior parts of the swath, improving the overall wind retrieval.

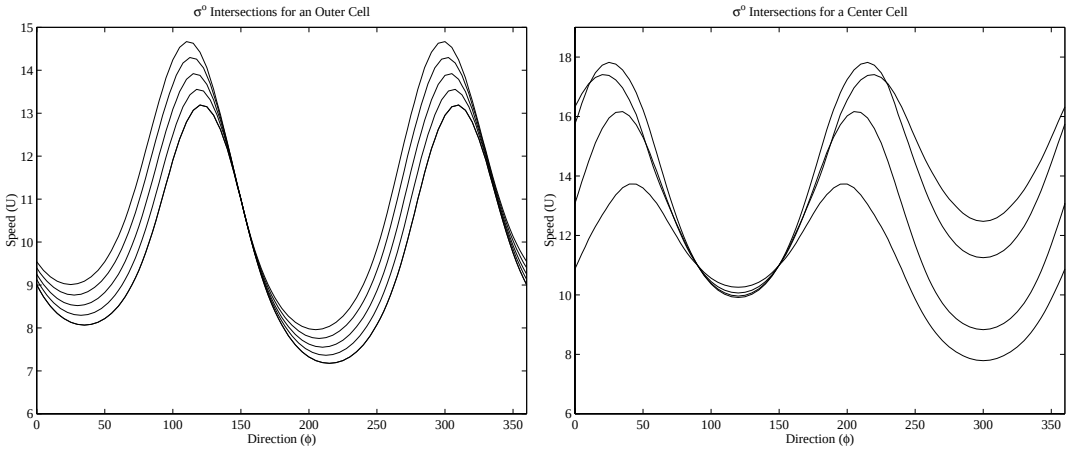

Figure 2.14: *The plot on the left shows the intersection of the GMF for several vertically polarized σ^o with little difference in the azimuth angles for each. The plot on the right shows the intersections for a cell in the very center (nadir region) of the swath. The measurements were take at azimuth angles of 0° and 180° with using a vertical and horizontal beam for each angle. In both cases the true wind is 11 m/s at* 150°.

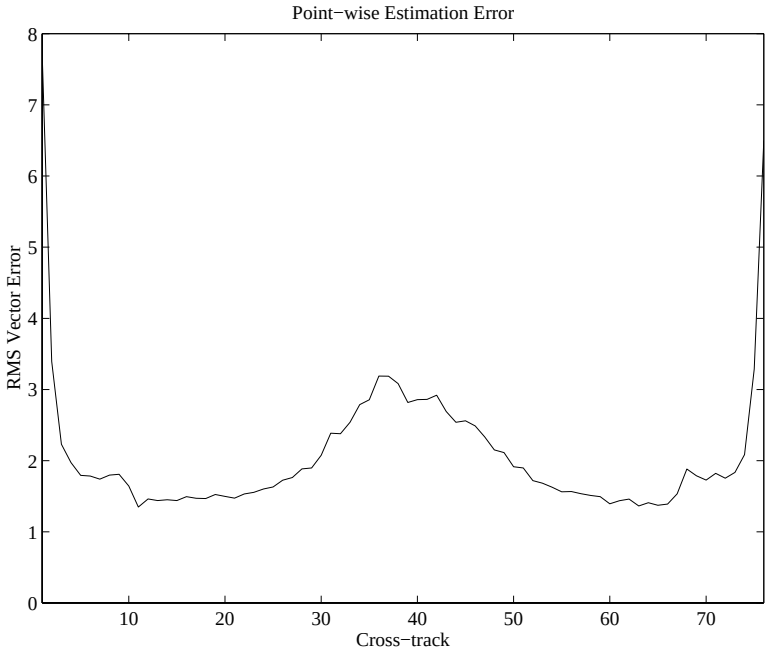

Figure 2.15: *The point-wise wind estimation error as a function of cross-track index. The edges and the middle regions exhibit very poor wind retrieval accuracy.*

Chapter 3

Simulating Winds Fields

3.1 Motivation

Before a field-wise wind retrieval algorithm can be built and tested, a method of simulating the SeaWinds data sets must be developed. The ability to simulate realistic winds plays a critical role in later evaluation of the field-wise wind retrieval algorithm. This chapter describes and evaluates three different methods for simulating wind fields. The first method is based on matching the power spectral density (PSD) of the simulated wind to the theoretical PSD of surface ocean winds. The second method uses wind field models to interpolate the gaps in NSCAT estimates of the wind to fill a SeaWinds swath. The third method uses wind field models to model the interpolated NSCAT winds, creating a low-pass version of the NSCAT data. Finally, the PSDs of winds generated using each of these methods are compared.

3.2 Synthesized Wind Fields

The first proposed method for simulating wind is to generate a wind field based on a model for the PSD. Using data from the Seasat scatterometer, [13] showed that the PSD of surface mesoscale ocean winds follows a power law of k^{-2}, where k is the wavenumber. Using this fact, randomly generated simulated wind fields are created using a field of Gaussian white noise, $w(m,n)$, filtered so the spectrum falls off at the rate k^{-2}. The filter is implemented using the following convolution:

$$u(m,n) = \sum_{k=-\infty}^{\infty} \sum_{l=-\infty}^{\infty} h(m-k, n-l) w(m,n), \tag{3.1}$$

where

$$h(m,n) = \frac{1}{4\pi^2} \int_{-\infty}^{\infty} \int_{-\infty}^{\infty} \left(\sqrt{k_1^2 + k_2^2} \right)^{-2} e^{j(mk_1 + nk_2)} dk_1 dk_2. \tag{3.2}$$

In short, the inverse transform of a radially symmetric surface with a k^{-2} falloff is convolved with a field of Gaussian white noise. To create a wind field, the u and v components are generated independently and combined to form the wind speed and direction.

A single realization of wind generated using this method is displayed in Figure 3.1. In this figure the wind exhibits a fairly realistic flow and the variability between each individual vector seems consistent with other visually inspected estimates of the surface winds. The primary problem with such wind fields is that they lack common phenomenological features, such as storm fronts and cyclones. Unfortunately, these features are important because they have historically been the hardest to estimate using field-wise estimation [3].

3.3 Interpolated NSCAT Winds

While the previous technique uses synthetic wind fields, better, more realistic winds can be obtained using real data. However, there is a very limited set of possible sources of which NSCAT is the best. As mentioned, the SeaWinds data differs from NSCAT data in that there is no nadir gap and the swath is wider. Two fundamental problems arise in attempting to convert NSCAT data to simulated SeaWinds data. The first is that there are many missing data points in the NSCAT swath due to calibration cycles of the instruments and σ^o collocation errors. These missing data points must first be interpolated from the existing data. The other problem is due to the fact that NSCAT has a smaller coverage area than SeaWinds. In order to make the NSCAT data conform to the SeaWinds swath, data in the NSCAT nadir gap and on the outer edges must be extrapolated from the two NSCAT swaths. It should also be noted that the fundamental limitation of NSCAT data is the noise resulting from measurement noise and ambiguity removal errors in processing the data. These two

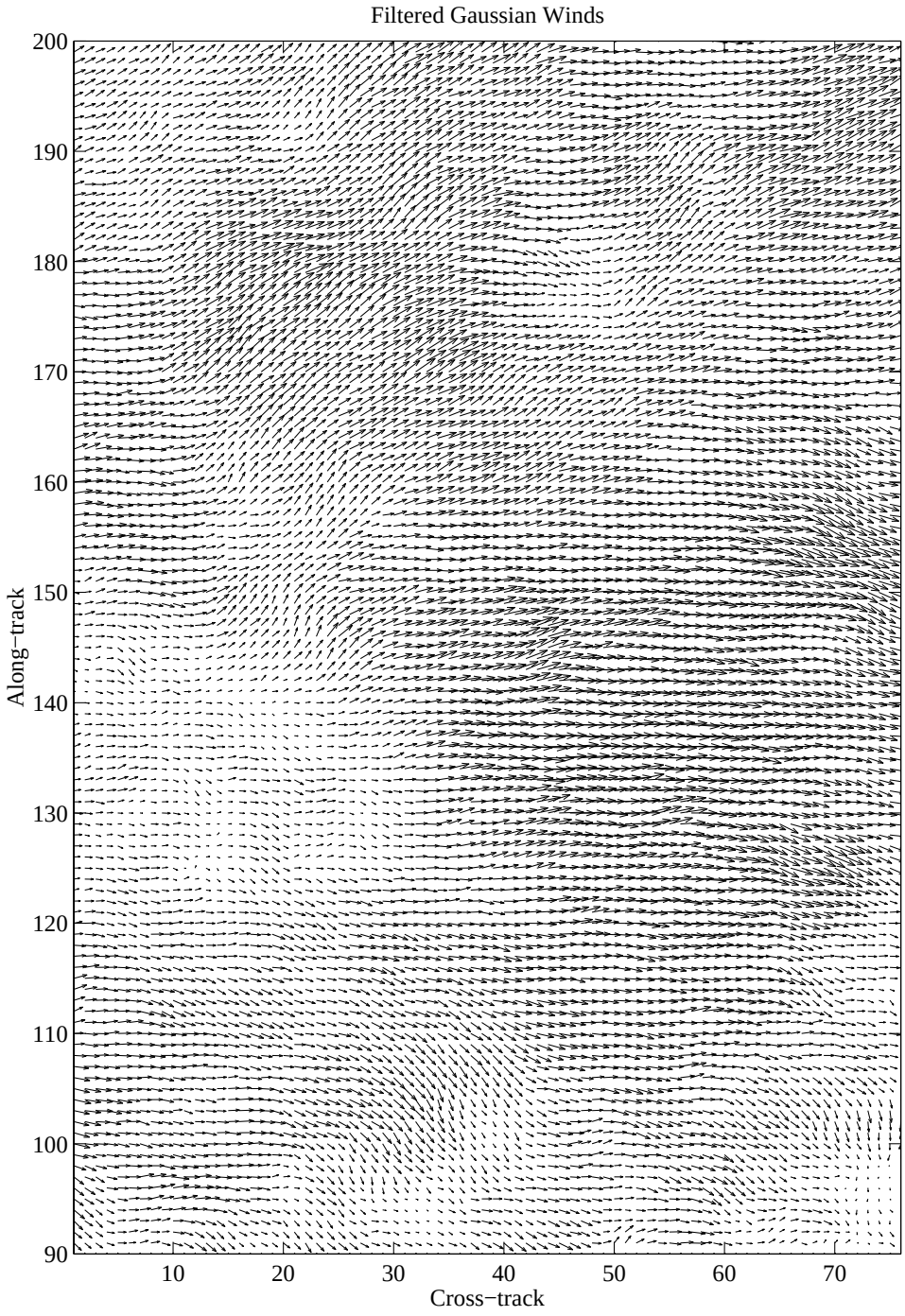

Figure 3.1: *Simulated winds generated using filtered Gaussian noise.*

factors combine to make the NSCAT derived winds more variable than the underlying true wind fields.

In order to best interpolate and extrapolate the NSCAT data an optimal interpolation method is developed. Over the years several optimal interpolators have been introduced for multi-dimensional data [14], [15]. This section proposes to interpolate the wind using the autocorrelation of the wind and a weighted model fit to the data.

3.3.1 Weighted MAP Least Squares Estimates

The first step in interpolating the NSCAT data is applying the wind field models, particularly the KL model, to the field so that an accurate estimate of the missing data can be obtained. Figure 3.2 shows a region of NSCAT winds with missing wind vectors resulting from the calibration cycle of the instrument and gridding errors in collocating σ^o. Next to this region of wind is a plot of the least-squares model fit, W_m, to the NSCAT wind field. This model-based estimate of the original wind field, W_t, is generated using a pseudoinverse of F in the following manner:

$$X_m = F^{\dagger} W_t, \tag{3.3}$$

$$W_m = F X_m. \tag{3.4}$$

A model fit to the wind field is used to supply information in the areas where there is missing data. For example, the vectors in the modeled wind corresponding to the cells where there is no data in the NSCAT wind can be taken and inserted in the NSCAT field, thus filling in the gaps. A closer look at the modeled wind in Figure 3.2 also yields some important information about the nature of the pseudoinverse. Because the pseudoinverse is a least squares fit, it attempts to model the gaps. Since the model is truncated it cannot force the wind vector cells to zero but they are somewhat smaller than the surrounding winds. To correct this a weighted least squares fit is applied which only weights the cells with valid wind vectors. The formulation for the weighted inverse is as follows [16]:

$$\hat{X} = (F^T S^{-1} F)^{-1} F^T S^{-1} W_t. \tag{3.5}$$

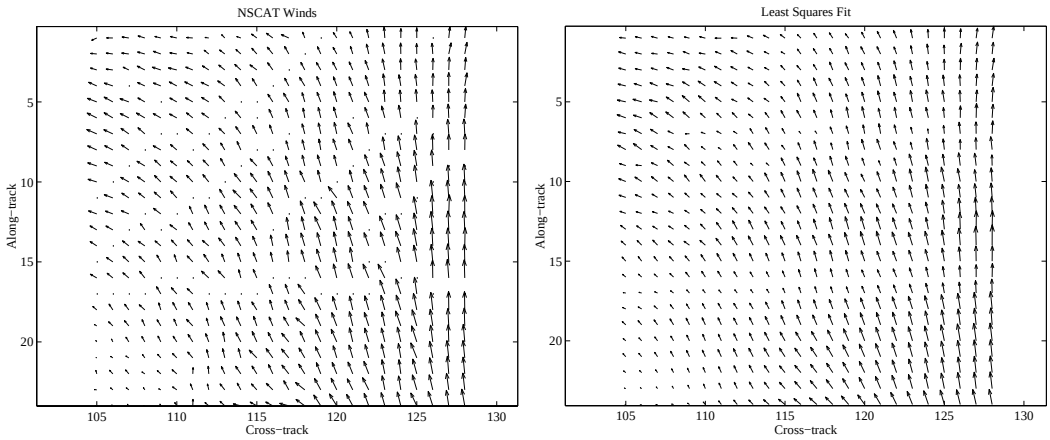

Figure 3.2: *NSCAT winds and a least-squares model fit to the wind.*

For an $M \times N$ region, S is a $2MN \times 2MN$ diagonal matrix with the elements of the diagonal, $s_{n+n(m-1)}$, equal to the weighting for the $(m,n)^{th}$ element of the wind field. The diagonal elements of S are weighted heavily for cells with no data and set to a small number for cells with data. Figure 3.3 shows the same region as Figure 3.2, now the KL model has been fit to the data using the weighted least squares fit. Using this fit the wind vectors corresponding to the missing cells look much more realistic. Finally, Figure 3.4 illustrates the interpolated NSCAT region with modeled wind inserted into the cells with no data.

The weighted inverse works well for interpolating regions where the gaps are small and completely surrounded by wind. However, for extrapolation of larger spaces, such as the nadir gap between the two NSCAT swaths, the estimate gets unwieldy in the middle where there are large areas without data. To correct for this a MAP fit can be used to ensure that the model fit to the data is also realistic. The MAP estimate for model based wind retrieval was first derived by Brown as follows [17]:

$$J_{MAP}(X) = f_{W|X}(W|X) f_X(X), \tag{3.6}$$

$$\hat{X} = \arg\max_X J_{MAP}(X), \tag{3.7}$$

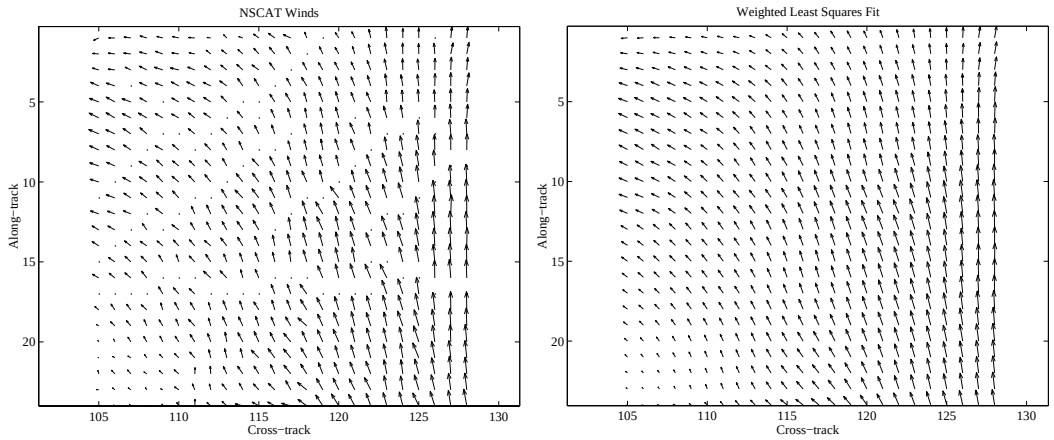

Figure 3.3: *NSCAT winds and a weighted least-squares model fit to the wind.*

where

$$f_{W|X}(W|X) = \frac{1}{(2\pi)^{\frac{N}{2}}} \exp -\frac{1}{2}(W - FX)^T(W - FX), \tag{3.8}$$

$$f_X(X) = \frac{1}{(2\pi)^{\frac{N}{2}}|R_W|^{\frac{1}{2}}} \exp\left(-\frac{1}{2}X^T F^\dagger R_W^{-1} FX\right). \tag{3.9}$$

A Gaussian model with wind autocorrelation matrix R_W is chosen for $f_X(X)$ because it imposes the least restrictive *a priori* conditions on the wind estimate.

By eliminating the constants and taking the log of each side of the provided MAP estimate, $\hat{X}$ is reduced to

$$\hat{X} = \arg\min_X -\frac{1}{2}(W - FX)^T(W - FX) - \frac{1}{2}X^T F^\dagger R_W^{-1} FX. \tag{3.10}$$

Because the KL model is orthonormal, $F^\dagger = F^T$. Using this simplification, $\hat{X}$ is found by taking the derivative of the above equation and setting it to zero. Expanding the log of J_{MAP}:

$$J_{MAP} = -\frac{1}{2}(W^T W - W^T FX - X^T F^T W + X^T F^T FX) - \frac{1}{2}(X^T F^T R_W^{-1} FX), \tag{3.11}$$

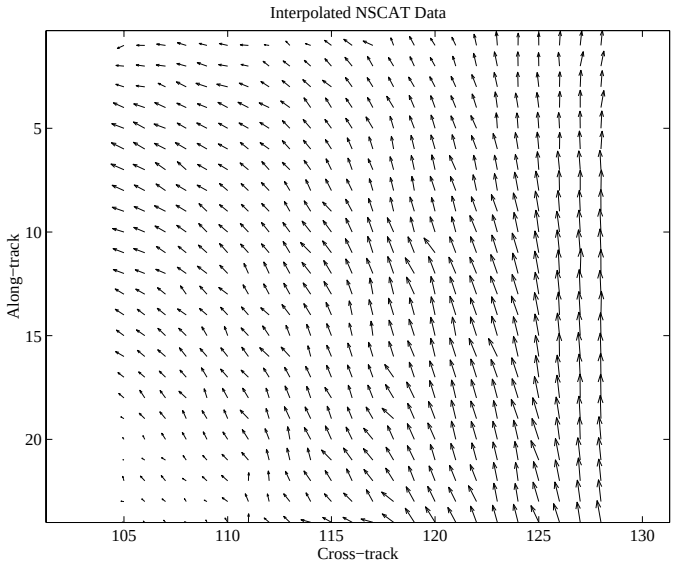

Figure 3.4: *Interpolated NSCAT data.*

then taking the derivative,

$$\frac{dJ_{MAP}}{dX} = -\frac{1}{2}(-F^TW - F^TW + 2F^TFX) - \frac{1}{2}(2F^TR_W^{-1}FX) = 0, \quad (3.12)$$

$$= F^TW - F^TFX - F^TR_W^{-1}FX = 0, \quad (3.13)$$

$$F^TW = (F^TF + F^TR_W^{-1}F)X, \quad (3.14)$$

$$\hat{X} = (F^TF + F^TR_W^{-1}F)^{-1}F^TW. \quad (3.15)$$

This final form is nearly identical to the least squares pseudoinverse with the addition of the $F^TR_W^{-1}F$ term. The MAP inverse is combined with the weighted inverse to form a weighted MAP least squares fit to the data,

$$\hat{X} = (F^TS^{-1}F + F^TR_W^{-1}F)^{-1}F^TS^{-1}W. \quad (3.16)$$

This model fit provides an optimal interpolation of the NSCAT winds based on the autocorrelation matrix, R_W.

To demonstrate the effectiveness of this inverse Figure 3.5 shows a model fit which spans that nadir gap, slightly overlapping the two swaths. In this plot a least squares fit, weighted least squares fit and weighted MAP least squares fit are applied.

It is apparent that the least squares fit simply fits the model to the missing data while the weighted least squares fit does a better job of ignoring the missing data and creating a wind field that is consistent in magnitude across the gap, though it is not very realistic. The weighted MAP least squares fit generates a wind field that is appears reasonable. Using this fit, the missing data points are filled in with data from the model.

Figure 3.6 shows a portion of a swath of NSCAT data. Figure 3.7 shows the same swath where the missing data has been filled in and the swath interpolated to match a SeaWinds swath in width. The same phenomenological features are visible in both swaths making this a very realistic section of wind. It should be noted that the interpolated sections are also still visible because they are less variable than the actual data. The effect of this on the PSD of the wind is be examined later.

3.4 Modeled NSCAT Winds

The final simulated wind type is known as "modeled NSCAT winds". These winds are formed in a manner very similar to interpolated NSCAT winds but instead of merely filling the gaps the NSCAT data itself is replaced with modeled winds. This method further reduces variability of the NSCAT data, resulting in a smooth wind field. Figure 3.8 shows a section of modeled NSCAT winds. This wind field is a smoother version of the interpolated winds in Figure 3.7. In fact, the interpolated nadir gap can no longer be distinguished from the actual swaths.

While the modeled winds appear subjectively superior due to their smoothness there are a couple disadvantages associated with them. The first problem is that important features, such as storm fronts, can be smoothed significantly during the modeling. The second problem is that performing model-based wind estimation on model-based wind may yield unrealistically good results. An examination of the PSD for modeled winds compared to interpolated winds yields some insights in to the accuracy of this form of simulated winds.

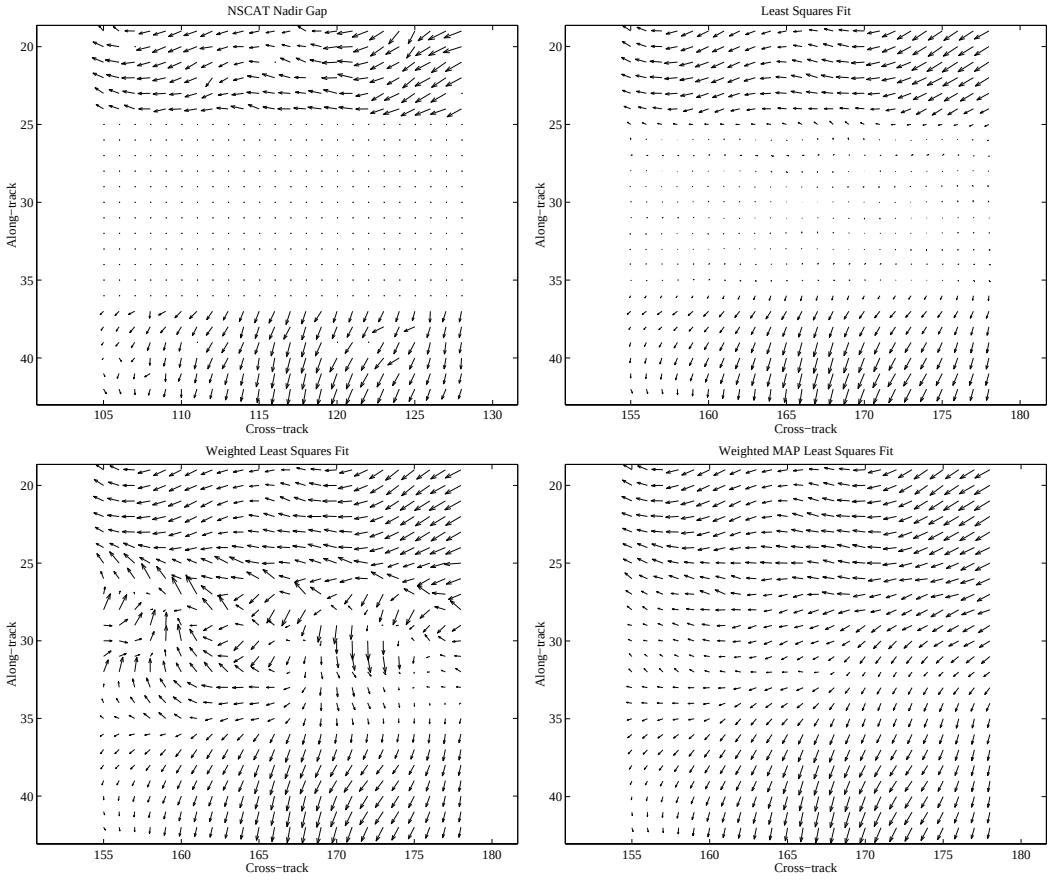

Figure 3.5: *Interpolation of the nadir gap using three different model fits.*

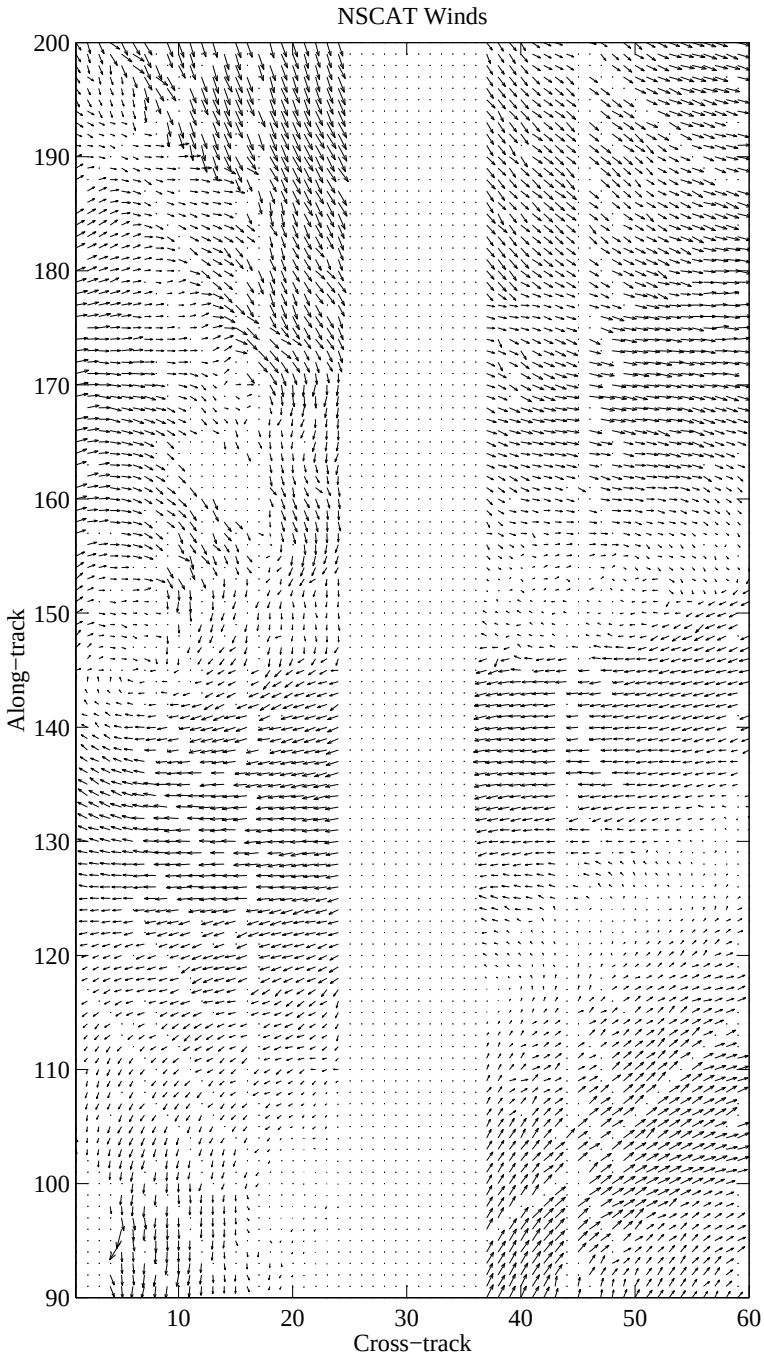

Figure 3.6: *Original NSCAT winds.*

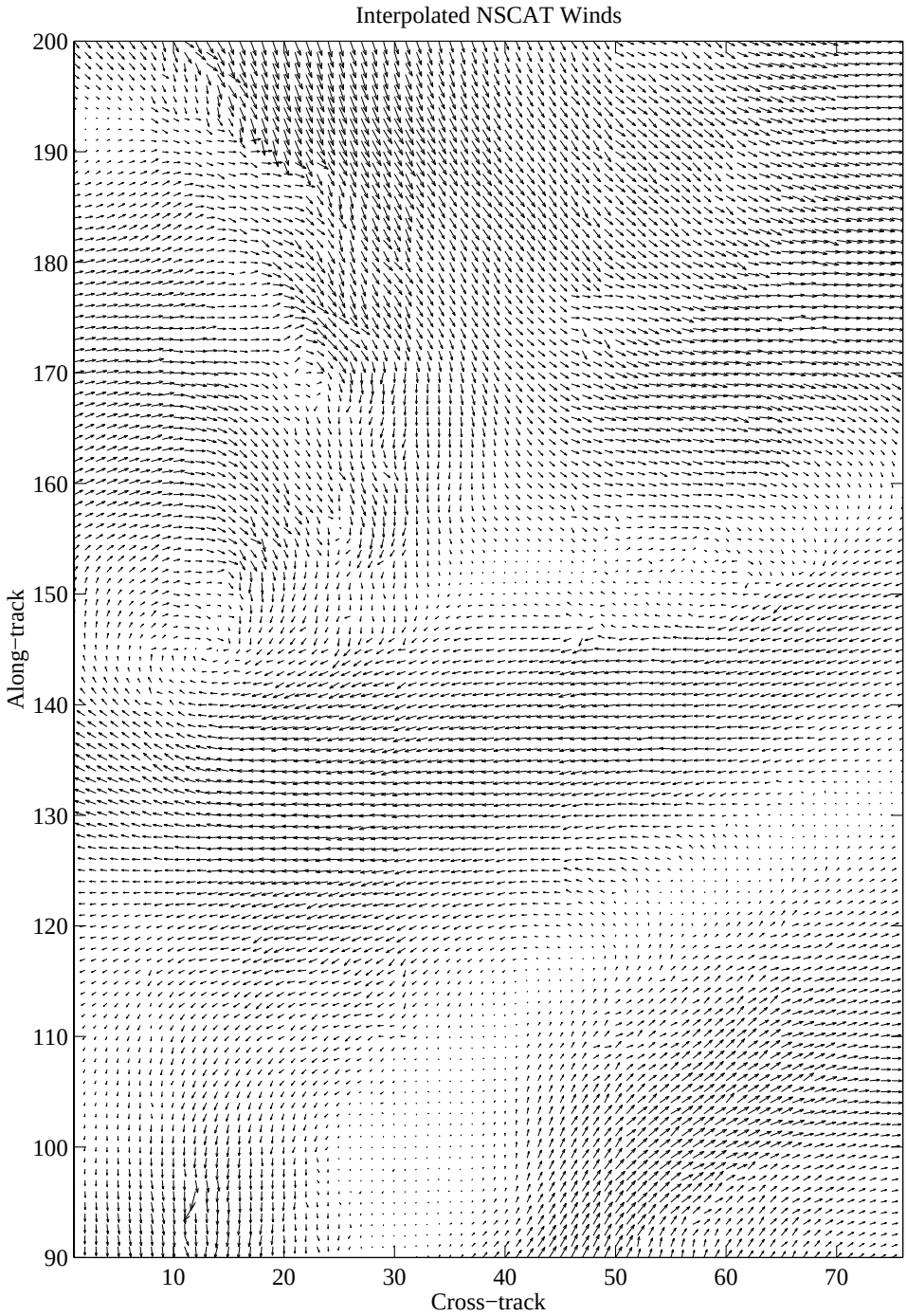

Figure 3.7: *Simulated winds generated by interpolated NSCAT winds.*

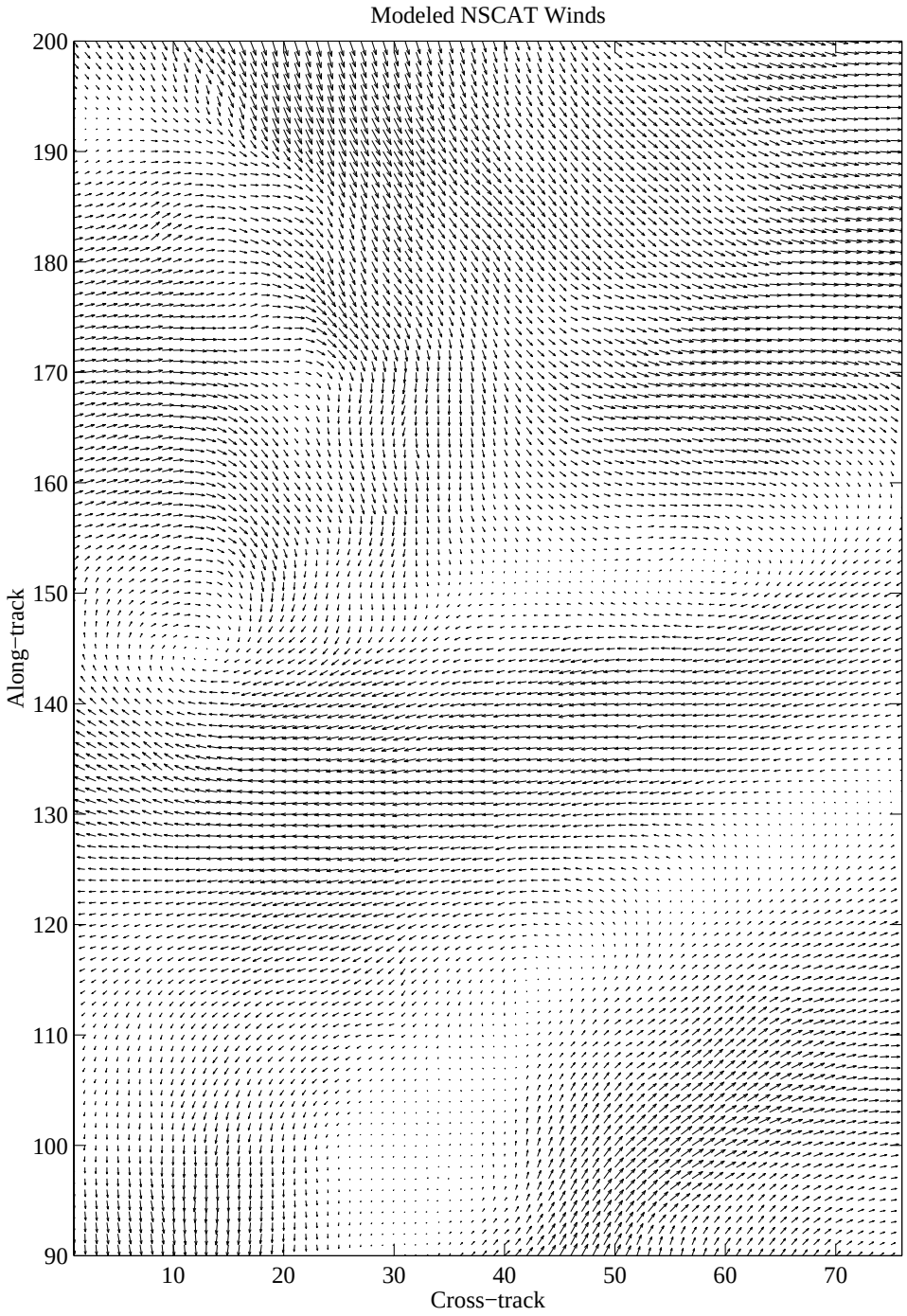

Figure 3.8: *Simulated winds generated by modeling NSCAT winds.*

3.5 Comparing the PSDs of Simulated Wind fields

The final step in validating the different forms of simulated wind is to ensure that the power spectral densities are consistent with the known characteristics of mesoscale ocean winds. To accurately describe the PSD of a wind field a 2-dimensional spectrum must be calculated. However, the 2-dimensions spectrum is hard to analyze so for simplicity the wind spectrum is only calculated in one dimension for both the along and cross-track cases. In these two cases the one-dimensional spectra are slices of the two dimensional spectra taken in the along-track and cross-track directions. For this analysis the PSD, $P_{xx}(f)$, is calculated using

$$P_{xx}(f) = \sum_{m=-(N-1)}^{N-1} w(m) r_{xx}(m) e^{-\jmath 2\pi F m}, \tag{3.17}$$

with

$$r_{xx}(m) = \frac{1}{N} \sum_{n=0}^{N-|m|-1} x(n)x(n+m), \qquad m = 0, 1, \ldots, N-1. \tag{3.18}$$

This approach is based on the Wiener-Khinchin theorem where $r_{xx}(m)$ is the unbiased sample autocorrelation of a length N sequence and $w(m)$ is a windowing function used to reduce the spectral leakage [18]. It should also be noted that since u and v are independent their respective spectrums should be identical and the spectrums used in this section are generated using the u component only.

3.5.1 Filtered Gaussian Spectrum

Because synthetic filtered Gaussian winds are generated on the basis of shaping the spectrum this test is merely a verification that the filtering works rather than a test to see if the spectrum is satisfactory. Figure 3.9 shows both the along-track and cross-track spectrums and verifies that they do, in fact, fall off at the correct rate.

3.5.2 Interpolated NSCAT Spectrum

Testing the PSD of interpolated NSCAT winds is very important because although the NSCAT winds contain many realistic features the interpolation could

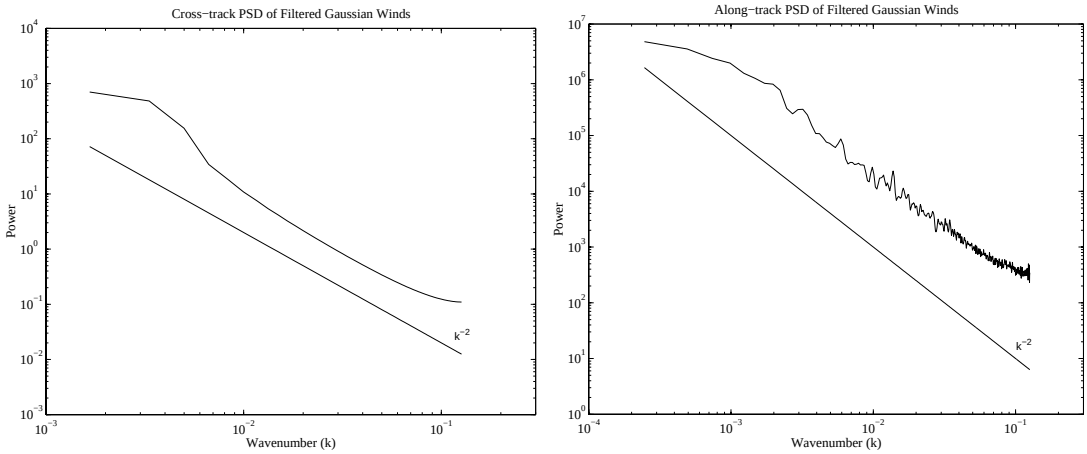

Figure 3.9: *The power spectral densities for the filtered Gaussian wind fields.*

also cause the frequency content of the wind to be significantly different than a true wind field. The results of the wind estimation algorithm would consequently become skewed.

Figure 3.10 shows the along-track and cross-track spectrums of interpolated NSCAT winds. The cross-track PSD appears to be very close to the theoretical slope of k^{-2}. The along-track PSD, on the other hand, is very close for low frequencies but it slopes up slightly as the frequencies get higher. This inflation at high spatial frequencies is most likely due to noise in the NSCAT data. Referring back to Figure 3.6 we see that the NSCAT data can be quite noisy in areas.

3.5.3 Modeled NSCAT Spectrum

As a final test of the modeled NSCAT winds the PSD of these winds is compared with the theoretical PSD. Like previous simulated winds the cross-track and along-track PSDs are plotted in Figure 3.11. The only noticeable difference between these PSDs and the ones for interpolated NSCAT winds is that the along-track PSD follows the k^{-2} fall off for all frequencies.

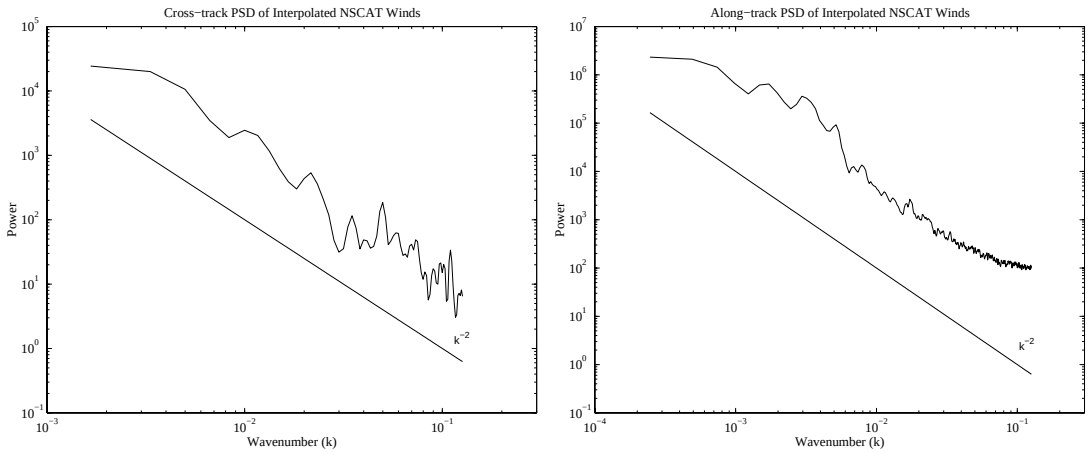

Figure 3.10: *The power spectral densities for the interpolated NSCAT wind fields. These fields also fall off an nearly a k^{-2} rate but there is some addition high frequency noise power that causes the slope to curve up at the end.*

3.6 Simulated Wind Selection

To properly evaluate the wind estimation algorithms presented in subsequent chapters a simulated wind format must be selected. Since the filtered Gaussian winds lack phenomenological features these are not used. The modeled and interpolated NSCAT wind field, however, each offer unique advantages in representing ocean wind. The interpolated NSCAT wind has the advantage of properly representing wind fronts and other features with the disadvantage that there is quite a bit of variability in the NSCAT data. The modeled NSCAT winds, on the other hand, smooth wind features but have wind spectrums that are closer to the predicted spectrums. Because each of these methods has different advantages both are used to evaluate the wind retrieval algorithms. With its built in noise the interpolated NSCAT wind provides worst case statistics for the wind retrieval while the modeled wind with its smoothed wind fields provides the best case statistics.

To create the simulated SeaWinds data files the modeled and interpolated NSCAT wind fields are taken and the σ^o values corresponding to the wind speeds and directions are calculated using the GMF and antenna geometries from a simulated

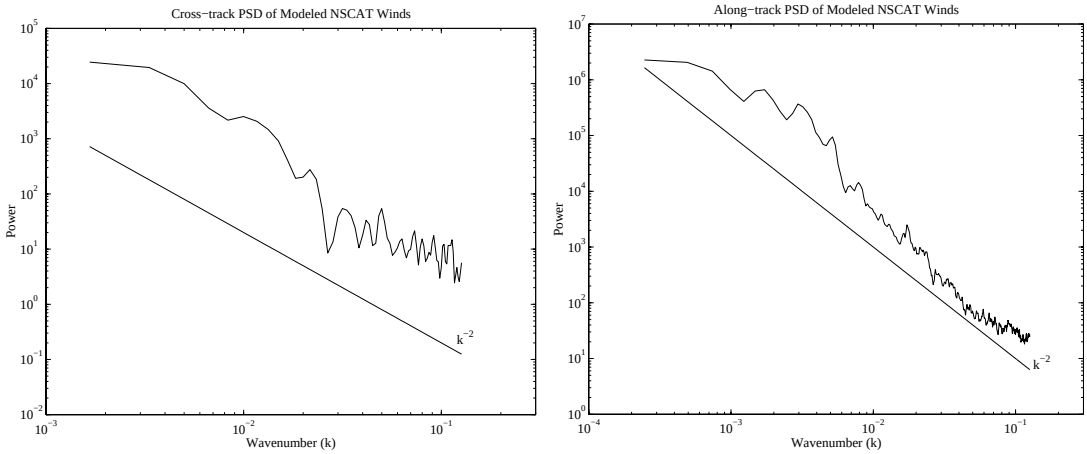

Figure 3.11: *The power spectral densities for the modeled NSCAT wind fields.*

SeaWinds file obtained from JPL. Once the field of σ^o are generated the field-wise estimation algorithms can be tested. One obvious benefit that simulated data offers is that the results of the field-wise estimation can be compared with the true wind to generate accurate performance statistics. (The convention used in this thesis is to name the simulated SeaWinds files after the rev. of NSCAT data they were created from. For example, the QSCAT rev. 2293A wind fields were created by interpolating the NSCAT file for the ascending node of rev. 2293.)

Chapter 4

Field-wise Estimation

The first step in any wind retrieval algorithm is wind estimation. The purpose of wind estimation is to determine the set of possible wind aliases from the noisy scatterometer measurements. For field-wise wind retrieval the set of field-wise aliases, $\left\{\hat{W}^{(n)}\right\}$, is determined from the measurements, $\mathbf{z}$, taken over the defined wind field region.

Determining $\left\{\hat{W}^{(n)}\right\}$ requires searching an objective function, $J(W)$, to find the wind fields that either maximize or minimize it, depending of the form of $J(W)$ (each wind alias, $\hat{W}^{(n)}$ corresponds to a local minimum or maximum in $J(W)$). The objective function provides a measure of the difference between $\mathbf{z}$ and the projected σ_m^o, which is a function of the geophysical model function (GMF) and the wind field W.

The type of objective function and the search method used to find extrema in $J(W)$ impacts the overall performance of the wind estimation step. This chapter examines and evaluates different objective functions and search algorithms to determine which perform best on simulated SeaWinds data. The optimal model size for the selected search algorithm is also determined. Finally, the resulting field-wise estimation algorithm is tested in several data sets to evaluate the performance.

4.1 Multi-start Estimation

Performing field-wise estimation requires a multi-dimensional global search over an objective function. Complications that arise in performing this search are

dimensionality and multiple local extrema, necessitating multiple searches for all extrema. One of the most effective ways to perform this search is using a multi-start method, similar to one used by Brown (1998).

The original field-wise multi-start proposed by Brown is based on randomly generating wind fields to initialize a steepest descent minimization of the objective function. Because of the many local minima, a steepest descent search yields different answers depending on the value of the initial W. In an effort to locate all the local minima, initial W vectors are randomly generated to uniformly cover the entire wind field space.

To take advantage of the wind correlation over a region, linear wind field models are used, where $W = FX$. A truncated wind field model, F, allows the wind field to be represented using a relatively small set of model parameters, X. Thus the full objective function $J(W)$ is reduced to $J(FX)$ and instead of searching over the entire space of W we search over the subspace determined by the length of X. The set of minima from $J(X)$, $\left\{\hat{X}^{(n)}\right\}$, correspond to the set of wind field aliases $\left\{\hat{W}^{(n)}\right\}$.

This section describes two different multi-start optimizations that can be used in performing field-wise estimation. The first method uses randomly generated starting points to perform a steepest descent optimization of the objective function while the second method augments the random starting points with information from the point-wise wind retrieval.

4.1.1 Basic Multi-start

As mentioned the multi-start optimization uses random initial parameters to perform a steepest descent optimization. For an $N_X \times 1$ initial vector X, the individual parameters are generated using a uniform random distribution based on the 3σ size of each parameter. An N_X-dimensional steepest descent search is then performed using the random vector as the initial starting point. As a result of this minimization a field wise alias is generated. Originally this process was performed 50 times and because of symmetry in the objective function the 50 solutions were negated and then used

as initial values for another 50 searches. The end result is 100 total optimizations providing a fairly effective search over the parameter space [3].

Using this multi-start routine many of the initial solutions fall into the same capture region. For a 50 multi-start optimization there may only be 20-30 unique solutions. To reduce the total number of optimizations required, a solution filter is added to the basic multi-start to determine the unique solutions before negating them. Consequently, only the unique solutions are re-optimized, reducing the optimization time without reducing the scope of the search.

4.1.2 Augmented Multi-start

The augmented multi-start is a variation of the basic multi-start which uses the fact that the first and second median filtered point-wise fields are often quite close to the true wind. In fact, a test performed on 200 regions showed that using a model fit to the median filtered fields as the initial X optimized to the true wind field in 24% of the regions. To take advantage of this, the augmented multi-start algorithm includes in the set of random initial vectors a model fit to the first and second median filtered wind fields. For good measure, additional random vectors are generated using a 1σ uniform distribution around the model fit to the median filtered fields.

The augmented multi-start performs 40 random multi-start optimizations, 2 optimizations using the first and second median filtered fields and 18 random optimizations around the median filtered fields. Once these 60 optimization are completed the results are filtered to eliminate duplicates and the remaining unique solutions negated and optimized.

4.2 Objective Functions

The accuracy with which the wind is estimated depends not only on the search routine but also on the form of the objective function, $J(X)$. Two objective functions are presented for use with SeaWinds data and the multi-start search algorithms. The first is based on the maximum likelihood objective function and the second is a least

squares objective function with a penalty term added to constrain the wind speeds over the region. Both objective functions are described in this section.

4.2.1 Maximum Likelihood Objective Function

The first multi-start algorithm to be examined uses a log likelihood function for the objective function. This function is obtained by negating the log of Eq. 1.21 and is given as follows:

$$J(X) = \sum_{l=1}^{MN} \sum_{k=1}^{K(l)} \frac{(z_{k,l} - \mathcal{M}_{k,l})^2}{\varsigma_{k,l}^2} + \ln \varsigma_{k,l}^2. \tag{4.1}$$

The objective function values are found by summing over all the cells in the region (l) and over all the measurements for each cell (k). For this expression the notation of the GMF has been simplified so $\mathcal{M}_{k,l} = \mathcal{M}(U_l, \chi_{k,l}, \theta_{k,l}, f_{k,l}, \mathrm{pol}_{k,l})$. U_l and $\chi_{k,l}$ are obtained from each element of the wind vector, W_l. Since $W = FX$, the objective function is, in fact, a function of X.

4.2.2 Constrained Objective Function

In an effort to incorporate as much outside information as possible, a constrained optimization is developed using a speed map based on the point-wise data. Because the speed information in the point-wise estimates is very reliable, a speed map is generated for a region by averaging the speeds of every alias in a single wind vector cell for each cell in the region. Figure 4.1 illustrates a field of simulated wind and the corresponding speed map taken from the point-wise aliases. This speed map is used by the objective function to penalize wind fields that do not match the the point-wise speeds. Replacing the log variance term in the log likelihood objective function with the speed penalty term, the objective function becomes a least squares, constrained objective function

$$J(X) = \sum_{l=1}^{MN} \sum_{k=1}^{K(l)} \frac{(z_{k,l} - \mathcal{M}_{k,l})^2}{\varsigma_{k,l}^2} + \lambda (S_l(X) - {S^{pw}}_l)^2, \tag{4.2}$$

where $S_l(X)$ is the speed of the wind alias for cell l, ${S^{pw}}_l$ is the speed generated from the point-wise data and λ is a scaling factor for the penalty term. It should

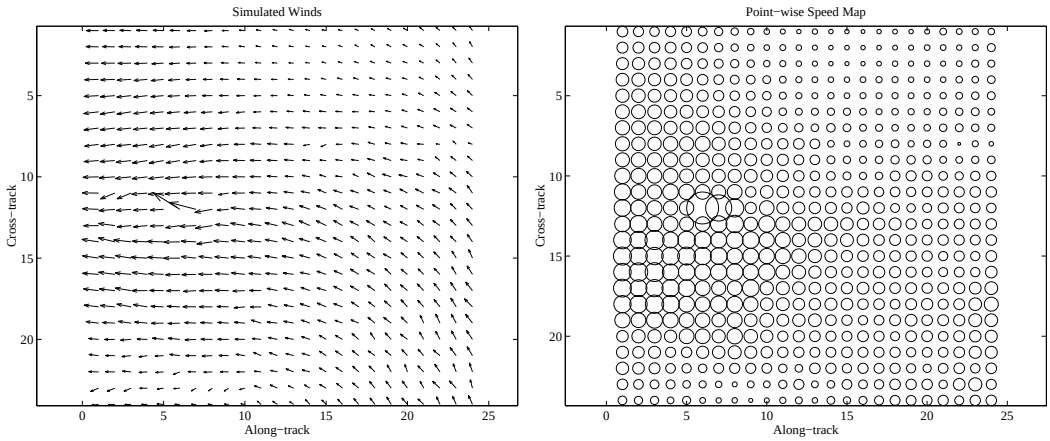

Figure 4.1: *Simulated wind and corresponding point-wise speed map.*

be noted that this is similar to a Lagrange method for constrained optimizations, however, using the Lagrange method, λ would be calculated to force the speed of the optimized wind to exactly match the speed map, S^{pw}. In this context we only want to penalize the objective function for being very different from the speed map, but not necessarily force it to be exactly the same. In testing this objective function, values of .01, .001 and .0001 are used for λ.

4.3 Testing Field-wise Estimation

To determine which combination of objective functions and search algorithms performs the best on average, each method is implemented on 200 regions of simulated winds. In this section the results of these simulations are compared to determine which combination offers the best wind retrieval performance.

Before reviewing the results some error measures are defined. The first error measure is E_{est}, the vector RMS error between a model fit to the true wind, W_m, and the optimized model fit to the true wind W_{opt}. The modeled wind, W_m, is generated using a least squares fit of the model to the true wind in the following manner,

$$X_m = F^{\dagger} W_t, \tag{4.3}$$

$$W_m = F X_m. \tag{4.4}$$

W_{opt} is calculated using the steepest descent algorithm with an initial value of X_m. The optimized true wind, W_{opt}, represents the best solution attainable using the objective function and consequently E_{est} is error built into field-wise estimation; there is no way to do better than this error. E_{est} is calculated as follows:

$$E_{est} = \left(\frac{(W_m - W_{opt})^T (W_m - W_{opt})}{MN} \right)^{\frac{1}{2}}, \tag{4.5}$$

for an $M \times N$ region. The second error,

$$E_{opt} = \left(\frac{(W_{opt} - W^{(n)})^T (W_{opt} - W^{(n)})}{MN} \right)^{\frac{1}{2}}, \tag{4.6}$$

is the vector RMS error between W_{opt} and the closest field-wise alias, $W^{(n)}$, resulting from the multi-start optimization. This error indicates how well the optimization algorithm locates the correct local minimum.

The most fundamental statistic relating to these optimizations is the percentage of regions in which the correct solution was found. In this context "found" is defined as any alias with W_{opt} less than 1.4 m/s. For any field-wise ambiguity removal algorithm to be effective we must be confident that the correct alias is in the set of possible aliases for each region. Table 4.1 displays these percentages for each of the multi-start algorithms. The percentages are given for the entire group of regions and also for the regions in the inner and outer parts of the swath.

In Table 4.1 the augmented multi-start performed the best overall with only one region lacking the true solution. The constrained objective function did not improve the percentage of solutions found.

Table 4.2 shows the RMS error, both E_{est} and E_{opt}, for the different optimization methods. The optimization error, E_{opt}, is also calculated for regions where the solution was found and regions where the true solution was not found. This enables us to estimate how close the aliases are when the true one is not located. We conclude that the augmented multi-start works the best. The errors are consistently higher for the constrained multi-start with the exception of the optimization error for regions where no solutions are found.

The final statistics considered in Tables 4.3 and 4.4 are the ranking accuracy of the different objective functions and the classification of regions into good, fair and

Table 4.1: *The percentage of regions where the true solution was found.*

Percentage of Regions with True Solution			
Optimization Type	All Regions	Inner Regions	Outer Regions
Original MS	98%	100%	96%
Augmented MS	99.5%	100%	99%
Constrained MS ($\lambda = .01$)	99%	100%	98%
Constrained MS ($\lambda = .001$)	98%	99%	97%
Constrained MS ($\lambda = .0001$)	98.5%	100%	97%
Aug./Const. MS ($\lambda = .01$)	97.5%	100%	95%
Aug./Const. MS ($\lambda = .001$)	98%	100%	96%
Aug./Const. MS ($\lambda = .0001$)	97.5%	100%	95%

poor based on E_{est} for each region. The ranking accuracy is the percentage of time the objective functions rank the correct solution as the 1^{st} alias, 2^{nd} alias and so on. The classification statistic labels a region as good if E_{est} for that region is less than 1.44 m/s, fair for 1.44 m/s $< E_{est} \leq$ 2.2 m/s, and poor if E_{est} is greater than 2.2 m/s.

Table 4.2: *Error in the closest estimates to the true wind.*

Estimation and Optimization Error				
Optimization Type	E_{est}	E_{opt}	E_{opt} (found)	E_{opt} (missing)
Original MS	1.30	0.49	0.32	2.67
Augmented MS	1.30	0.39	0.34	2.79
Constrained MS ($\lambda = .01$)	1.44	0.40	0.35	1.86
Constrained MS ($\lambda = .001$)	1.44	0.48	0.41	1.67
Constrained MS ($\lambda = .0001$)	1.44	0.46	0.41	1.63
Aug./Const. MS ($\lambda = .01$)	1.44	0.48	0.37	2.02
Aug./Const. MS ($\lambda = .001$)	1.44	0.42	0.36	1.54
Aug./Const. MS ($\lambda = .0001$)	1.44	0.45	0.37	1.61

Table 4.3: *The percentage of rankings for the alias closest to the true.*

Ranking Accuracy					
Objective Function	1^{st}	2^{nd}	3^{rd}	4^{th}	$\geq 5^{th}$
Log Likelihood	81%	10%	4%	2%	3%
Constrained ($\lambda = .01$)	80%	11%	3%	3%	3%
Constrained ($\lambda = .001$)	81%	11%	4%	1%	3%
Constrained ($\lambda = .0001$)	81%	11%	3%	2%	3%

Table 4.4: *The percentage of regions classified as good, fair or poor where good has* $E_{est} \leq 1.44$ *m/s, fair has* 1.44 *m/s* $< E_{est} \leq 2.2$ *m/s and poor has* $E_{est} < 2.2$ *m/s.*

Region Classification by Objective Function			
Objective Function	Good	Fair	Poor
Log Likelihood	73%	21%	6%
Constrained ($\lambda = .01$)	62%	29%	9%
Constrained ($\lambda = .001$)	70%	23%	7%
Constrained ($\lambda = .0001$)	70%	23%	7%

4.4 Analysis of Results

We now examine these results in greater detail. Specifically, the regions where multi-start failed are examined to find fundamental problems with each multi-start method. Because multi-start is a random search it is important to realize that some regions may be missed in one test but found in another simply because of differences in the initial parameter vectors. In this analysis we look only at those regions that were missed consistently by the different optimizations. Finally, the point-wise estimation error is computed and compared with E_{est} to determine if the magnitude of these errors is acceptable.

4.4.1 Missed Regions

Of the 200 regions tested there were four that were missed fairly consistently. These four regions are examined here to better understand the strengths and weaknesses of the multi-start algorithms.

Simulated Rev. 2293A, Along-track 240, Cross-Track 53

The most frequently missed region is found on the outer edge of the third swath of simulated wind. This region was missed in 6 out of the 8 simulations. Figure 4.2 shows plots of the true wind field, a model fit to the true wind and the closest ambiguity to the true wind. In the plot of the true wind field a small storm front can be seen running through the center of the region. Brown (1998) showed that wind fields with fronts and cyclones typically have a larger number of local minima and that the capture region size for the true solution is significantly smaller on average. This region is an example of such a case. In addition to the front, the bottom half of the region appears to have a cyclonic flow. These two factors combine to make an objective function with many local minima and relatively small capture regions. The only way to compensate for this is to use a larger number of initial random parameters when performing the search. The augmented search was able to correctly locate this wind field because the first median wind field is very close to the true and fell into the correct capture region.

This region is a also good example of the modeling error that results from model-based estimation. Using a 22 parameter model the model fit to the true wind, W_m, completely smoothes over the frontal feature in the middle of the region. To overcome this smoothing a higher order model must be used, greatly increasing the computational time required to optimize a region. Thus, in performing model-based estimation a tradeoff must be made between computational time and modeling error.

One final consolation: while the closest alias was classified as not found, visual inspection shows that the general wind flow is still very similar to the model fit to true. Therefore, if this closest alias was used instead of the best one the resulting swath of wind should still be quite accurate.

Simulated Rev. 2293A, Along-track 258, Cross-track 53

The region of wind directly adjacent to the region discussed above is also missed quite often with 5 out of the 8 simulations failing to locate the correct alias. Figure 4.3 shows the true wind, the model fit to true and the closest alias. Unlike the previous region this region contains no unusual phenomenological features. In fact, it is very difficult to see differences in closest alias and the modeled true wind (middle and bottom plots). There are only a couple areas where the directions appear to differ. The reason that this region was classified as missed is most likely due to the very high wind speeds. This region has an average wind speed of 13.5 m/s and so small differences in the direction result in large vector errors and large E_{opt}. Most likely, the initial parameter vector fell into the correct capture region but the gradient search ended at a slightly different place and because the wind speeds were so high the alias is classified as not found. The fact that this region was missed so many times may also indicate that the bottom of the minimum is large and relatively flat with many smaller local minima. Thus different searches may result in slightly different answers.

Simulated Rev. 2294A, Along-track 308, Cross-track 53

The third most often missed region is in the second simulated swath. This region demonstrates one of the most basic problems with scatterometer based wind retrieval. Figure 4.4 shows the true, modeled true and closest alias wind fields. In these plots the low wind speeds are very evident, in fact, the average wind speed for the region is only 2.2 m/s. When the wind speeds are low it is very difficult to infer the wind from the scatterometer data. For this reason it may be necessary to choose a speed threshold and not estimate the wind in regions where the speed is below that threshold. It has been shown recently that wind retrieval is not accurate for regions with average wind speeds of less than 4 m/s [19]. This region is one that such a threshold would apply to.

Simulated Rev. 2293A, Along-track 510, Cross-track 53

The final region to be examined and the fourth most commonly missed region is the sixteenth along-track region in the third simulated swath. This region is significant because it best illustrates one of the drawbacks to using the constrained objective function. Figure 4.5, like the previous figures, contains plots of the true wind, modeled true and closest alias. Also included is a plot of the speed map generated for this region. In the middle right section of the true wind field we see spurious high wind speed vectors. This may be the beginning of a front or some other feature but it does not appear to be a large scale phenomenon. Due to the low order nature of the model these high wind speed vectors are smoothed out considerably when fit to a model (top right plot). When the constrained optimization is performed a speed map is generated from the point-wise data to help force the optimized wind to match the point-wise speeds. This is detrimental, however, if the speed map has higher spatial variability than the truncated model can represent. In this case the speed map contained large speed values corresponding to the spurious high wind speed vectors (bottom right plot Fig. 4.5). During the optimization the model attempts to fit this speed map but cannot because of its low spatial variability. In the plot of the closest alias, a large high wind speed section is found corresponding to the high wind speeds in the speed map. Hence, more error is introduced trying to match a highly variable wind speed map. This is one of the primary disadvantages of using a constrained objective function.

4.4.2 Accounting for High E_{est}

As a result of noisy σ^o measurements and poor antenna geometries, the optimized model fit to true, W_{opt}, often has a significant amount of error when compared with W_m. This error is built into the wind estimation process and there is no way to eliminate it with out redesigning the instrument or finding a way to reduce the noise. The purpose of this section is to compare E_{est} with the error between the true wind and the closest point-wise wind vectors to gauge the magnitude of the field-wise retrieval error compared to the point-wise retrieval error.

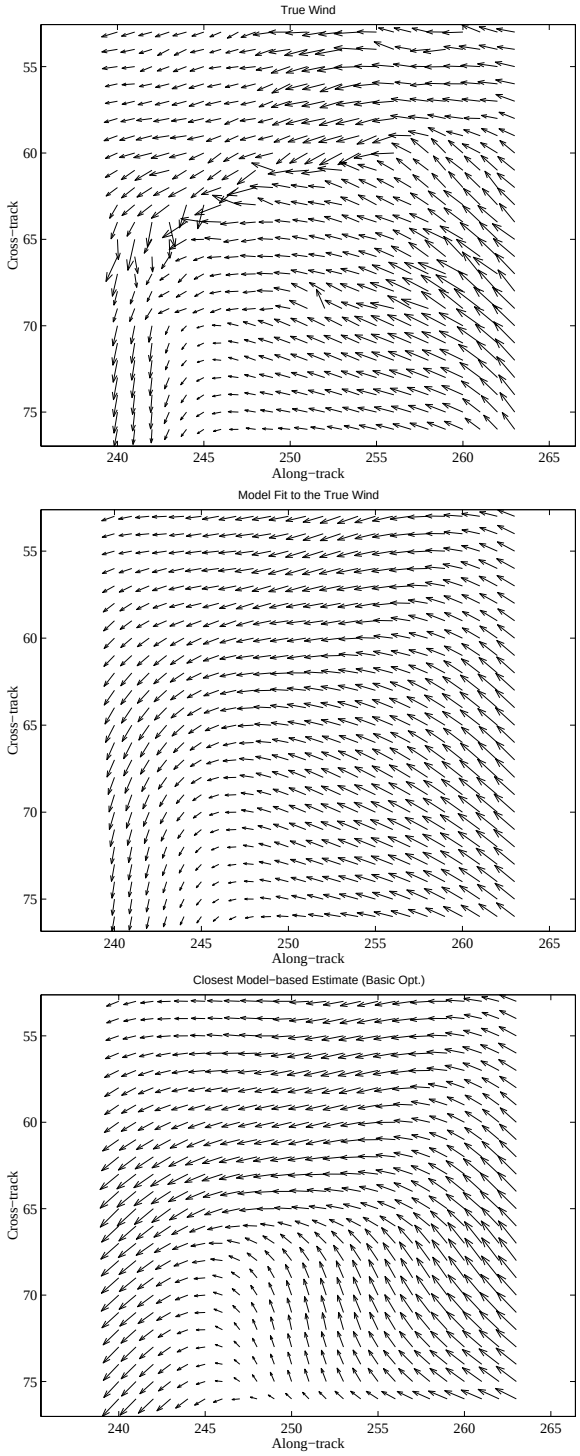

Figure 4.2: *The top plot is the true wind, the middle is the model fit to the true and the bottom is the closest field-wise alias. This region is taken the from the simulated rev. 2293A.*

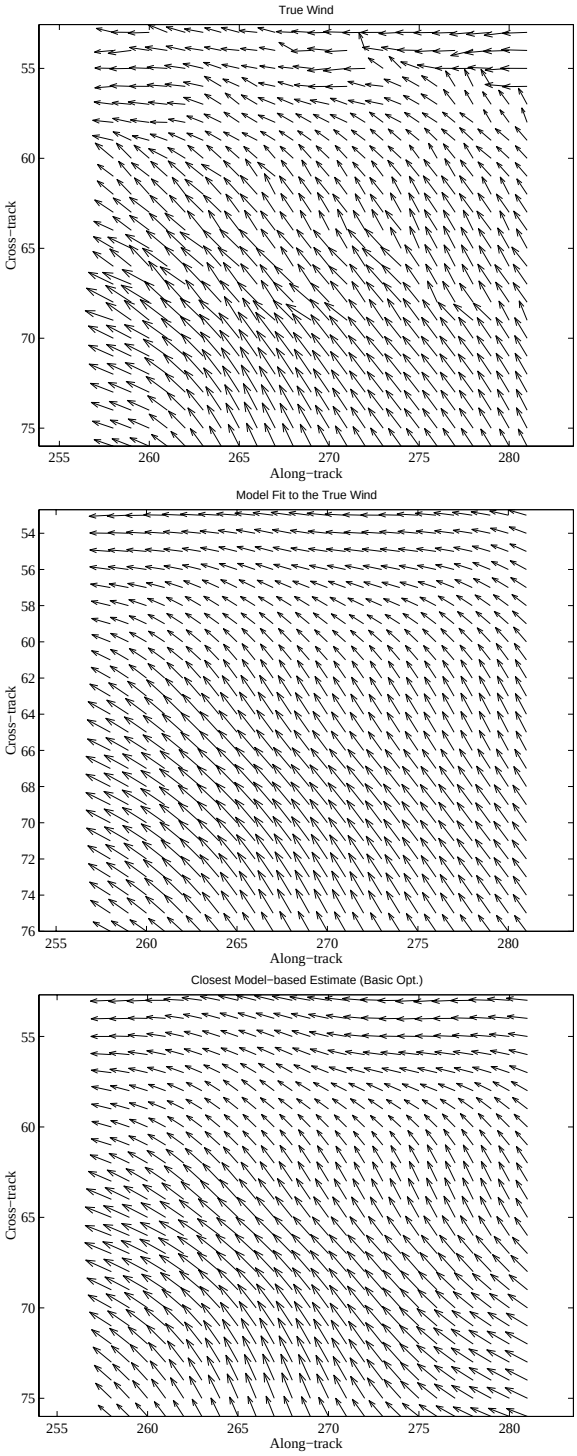

Figure 4.3: *The top plot is the true wind, the middle is the model fit to the true and the bottom is the closest field-wise alias. This region is taken the from the simulated rev. 2293A.*

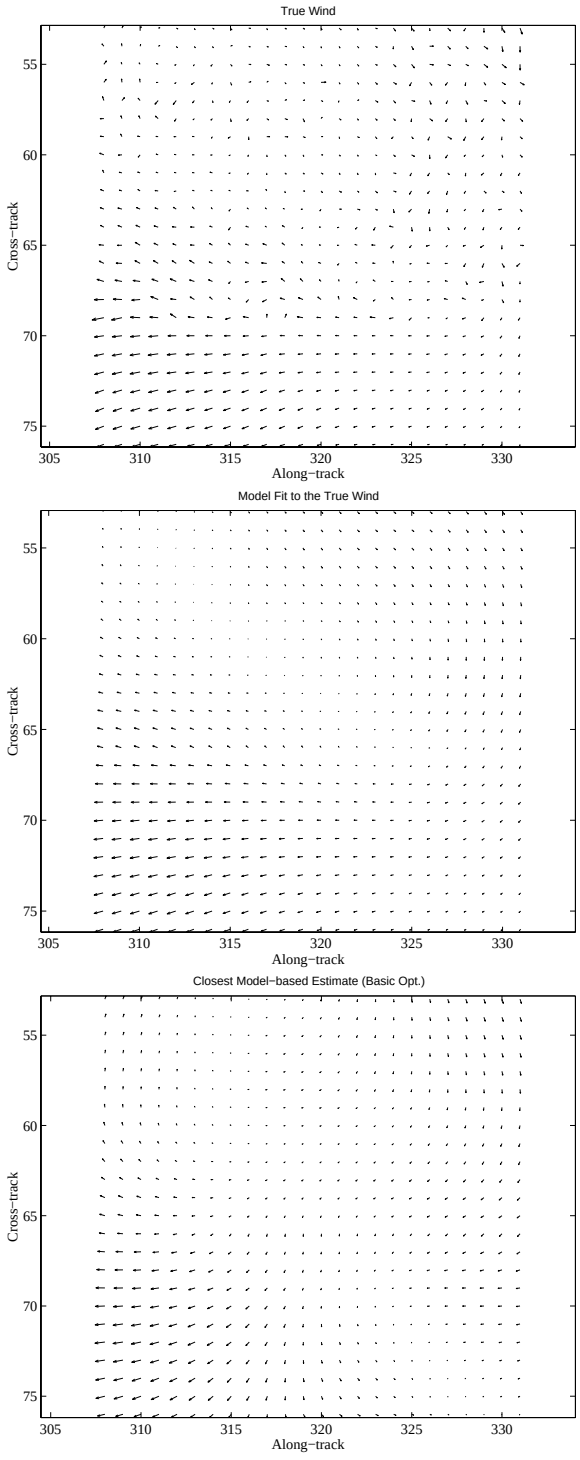

Figure 4.4: *The top plot is the true wind, the middle is the model fit to the true and the bottom is the closest field-wise alias. This region is taken the from the simulated rev. 2294A.*

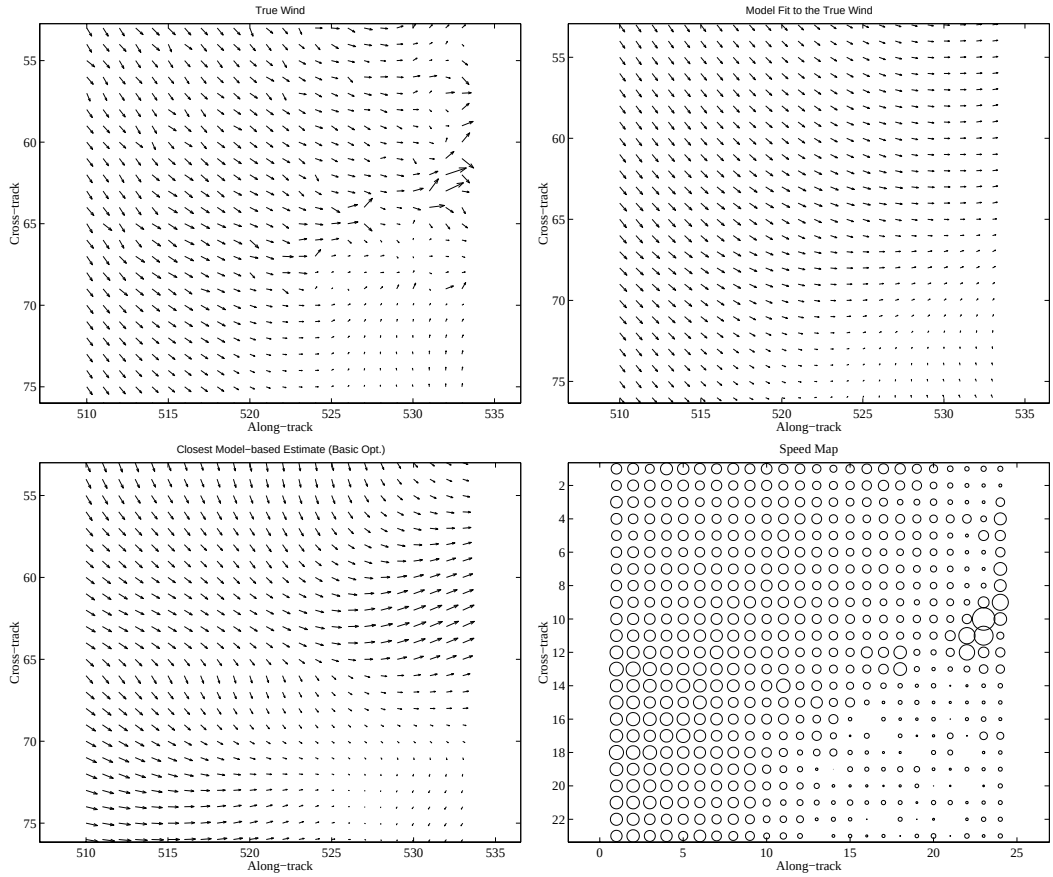

Figure 4.5: *The top plot left is the true wind, the top right is the model fit to the true, the bottom left is the closest field-wise alias and the bottom right is the speed map for the region. This region is taken the from the simulated rev. 2293A.*

Using the same 200 regions, the error between the closest point-wise aliases and the true wind, W_t, was calculated. The error, denoted E_{pw}, is calculated as follows:

$$E_{pw} = \left(\frac{(W_t - W_{pw})^T (W_t - W_{pw})}{MN} \right)^{\frac{1}{2}}, \tag{4.7}$$

where W_{pw} is the column scanned vector of the field of closest point-wise aliases to the true wind for an $M \times N$ region. This error can now be compared with E_{fw}, which is the field-wise estimation error calculated using

$$E_{fw} = \left(\frac{(W_t - W_{fw})^T (W_t - W_{fw})}{MN} \right)^{\frac{1}{2}} \tag{4.8}$$

where W_{fw} is the closest field-wise alias to the true wind. Table 4.5 compares the errors for each case. The data in this table is generated using the maximum likelihood objective function and the constrained objective function, with $\lambda = .001$. The error is computed for the cases where all the regions were included and only including the regions where the true solution was found (this is denoted "found" in the table).

Table 4.5: *Field-wise estimation error compared with the point-wise estimation error.*

Error Comparisons		
Objective Function	Error Type	RMS Error (m/s)
Max-Like	E_{fw}	1.75
	E_{fw} (found)	1.69
Constrained ($\lambda = .001$)	E_{fw}	1.80
	E_{fw} (found)	1.75
none	E_{pw}	1.77

Thus, while E_{fw} on the order of 1.5-2 m/s is not negligible it is comparable to the error using the closest point-wise aliases. This fact helps to alleviate concerns that E_{est} may be prohibitively large.

4.5 Model Order Selection

With a multi-start algorithm selected we turn our attention to choosing the best model size, N_X. In finding the best N_X, trade-offs must be made between the accuracy of the model and computational complexity of the objective function search. The accuracy increases as the model size increases but the dimensionality of the objective function also increases. The best model is the one that provides adequate modeling error, E_m, with minimal computational time.

To make the trade-off between accuracy and complexity the model basis vectors must be selected to retain the maximum information for the number of bases kept. The KL model is optimal since it minimizes the basis restriction error for every value N_X [12]. To choose the number of basis vectors we refer to Figure 4.6 which plots the eigenvalues of the KL basis vectors sorted in descending order. These eigenvalues represent the average energy attributed to a wind field by the corresponding basis vectors. In Figure 4.6 there are natural breaks in the eigenvalues for model sizes of 3, 6, 11, 14, 20, 25, and 30. These values make logical choices for N_X.

The best model size is determined by running the augmented multi-start on 80 different regions using different model sizes and comparing the results. Since model sizes of 3, 6, and 11 are extremely small, only sizes of 14, 20, 22, 25 and 30 are tested (22 is included for historical reasons).

Table 4.6: *Model-based estimation for different size models.*

Model Performance				
N_X	E_m (m/s)	E_{opt} (m/s)	E_{est} (m/s)	Unique Solutions
14	1.80	0.29	1.59	21.2
20	1.79	0.28	1.37	28.4
22	1.60	0.26	1.12	29.3
25	1.59	0.43	1.13	31.0
30	1.55	0.32	1.14	35.7

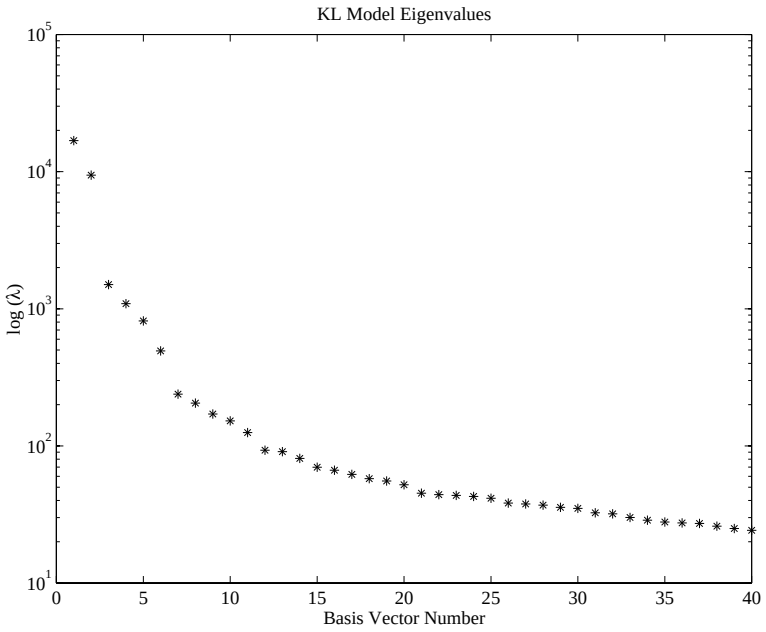

Figure 4.6: *Eigenvalues for the KL basis vectors.*

In Table 4.6 the 22 and 25 parameter models have low E_m while maintaining satisfactory computational complexity. Based on these results the 22 parameter model is used because it has comparable error to the 25 parameter model but is smaller.

4.6 Extended Evaluation of Field-wise Estimation

The final step in developing a field-wise estimation algorithm is to evaluate the performance of the selected parameters on a larger data set. The following statistics represent the performance of the augmented multi-start with the maximum likelihood objective function and a 22 parameter model on 1060 regions of data. The performance of the estimation is measured using the percentage of correct solutions found, E_{est}, E_{opt}, the ranking accuracy, E_{fw} and E_{pw} all of which are computed in the same way as described previously.

Table 4.7: *The percentage of regions where the true solution was found.*

Solutions Found		
All Regions	Inner Regions	Outer Regions
96.1%	99.3%	93.0%

Table 4.8: *Different estimations errors for the selected FWE algorithm.*

FWE RMS Errors	
Error Type	RMS Error (m/s)
E_{est}	1.79
E_{opt}	0.58
E_{fw}	1.45
E_{pw}	1.47

4.7 Summary and Conclusions

In performing field-wise estimation on 200 regions of simulated wind fields the accuracy and reliability of several field wise estimation techniques are evaluated. Overall, all of the techniques perform very well, with a 97%-99.5% probability of finding the true solutions in each region. The augmented maximum likelihood objective function performs the best with 99.5% of the correct solutions found and the lowest E_{est}.

To better understand the objective functions and their ability to locate the correct solutions the regions where solutions were not found are examined in detail. From this examination it is found that phenomenological features and low wind speeds are the primary reasons for missing the correct minima. It is also shown that the constrained objective function contains weaknesses that increase the error in the wind aliases. Finally, the estimation error for the field-wise aliases, E_{fw}, is shown to be comparable with the estimation error of the point-wise aliases, E_{pw}.

The augmented multi-start algorithm is tested for several different size wind models to find the best size. The 22 and 25 parameter models are shown to have

Table 4.9: *The percentage of rankings for the alias closest to the true.*

Ranking Accuracy				
1^{st}	2^{nd}	3^{rd}	4^{th}	$\geq 5^{th}$
72.5%	12.5%	5%	3.5%	6.5%

comparable modeling error, E_m. The 22 parameter model is chosen as the best trade-off between E_m and computational complexity as it is the smaller of the two models.

Finally, the 22-dimensional augmented maximum likelihood objective function is selected as the best choice for field-wise estimation on SeaWinds data. It has the best alias location percentage with the lowest estimation error. It has a good alias ranking accuracy, with 72.5% of the first aliases corresponding to the true wind, the highest percentage of good regions, based on the estimation error, and it is the best compromise between modeling error and dimensionality.

Chapter 5

Field-wise Ambiguity Selection

5.1 Ambiguity Selection

Field-wise ambiguity selection is the process of choosing the wind field alias closest to the true wind, $\hat{W}^{(i)}$, from the set of ambiguities generated during the field-wise estimation step. This chapter presents an algorithm for selecting the correct alias using only the information generated by the field-wise estimation.

A block diagram of the field-wise ambiguity selection algorithm is given in Figure 5.1. This algorithm is comprised of three main steps; field-wise median filtering, point-wise nudging and construction of the final field. Each of these steps are described in greater detail in this chapter. Finally, the overall performance of the ambiguity selection algorithms is evaluated.

Before continuing with a discussion of the algorithm the geometries of the wind field regions are described. The SeaWinds swath is divided into 24×24 wind vector cell regions; hereafter denoted wind field regions (WFR). These regions are chosen so

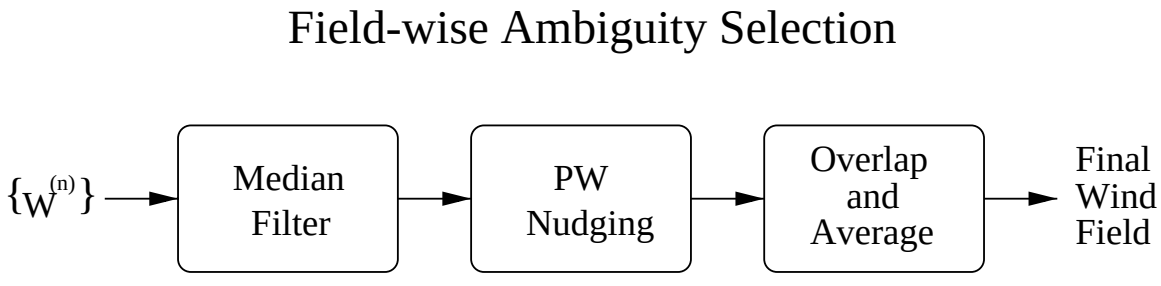

Figure 5.1: *Block diagram for the ambiguity selection algorithm.*

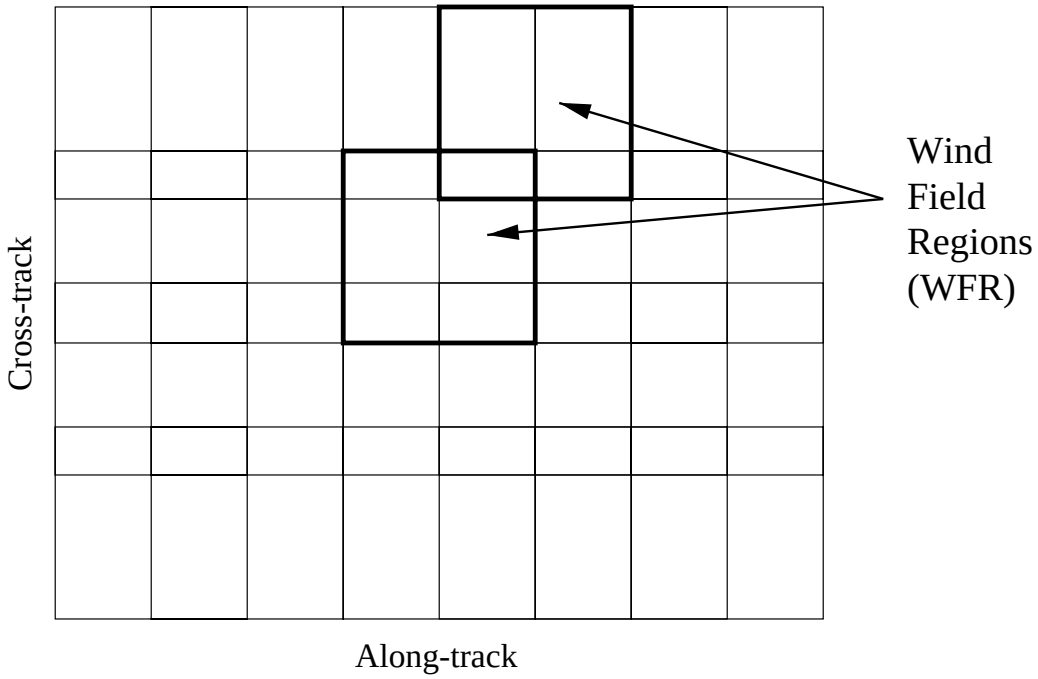

Figure 5.2: *The SeaWinds swath gridded into wind field regions.*

to overlap each other by 50% in the along-track direction and 25% - 33% in the cross-track direction. Figure 5.2 illustrates the SeaWinds swath and the subdivided regions. Field-wise estimation is performed separately for each region and the overlapping is used in selecting the correct alias.

5.2 Ambiguity Selection using a Field-Wise Median Filter

The most important and most difficult step in wind estimation is the actual selection of the closest ambiguity. The fact that a good estimate of the true wind exists in the set of aliases is of little worth unless we choose it as the final estimate. This is true for both field-wise and point-wise winds. The most important ambiguity selection tool for point-wise retrieval over the past several years has been the point-wise median filter (PWMF). This section proposes to extend the ideas behind PWMFs to a field-wise median filter (FWMF). First an overview of median filtering is given followed by a brief explanation of the PWMF, finally, the FWMF is described.

5.2.1 Median Filtering

Median filtering techniques have become a valuable noise reduction tool in image processing. The median filter is implemented for a single pixel at location (m,n) in the following manner [12]:

$$v(m,n) = \text{median}\,\{(y(m-k,n-l),(k,l)\epsilon W\} \tag{5.1}$$

where $v(m,n)$ is the filtered image, $y(m,n)$ is the noisy image and W is window typically centered on m, n. The pixels of the original image in the window are sorted by magnitude and the filtered value is selected as the median of these pixels. During the sorting, extreme pixel values resulting from noise are shifted to the ends of the sorted vector and have little effect on the median value. Thus, for a data set affected with impulsive noise the median filter minimizes the noise with little image degradation.

A valuable characteristic of median filters is edge preservation [12]. Other smoothing filters often average pixels together to reduce the noise, blurring the image and smearing hard edges. Since the median filter does not use averaging image edges are preserved.

5.2.2 The Point-wise Median Filter

In 1991, Shaffer et al. proposed a median filter algorithm for performing ambiguity selection for point-wise wind vectors. This algorithm chooses the alias as the median of the wind vectors in a window surrounding it. For scalar data the median is simply the center element of the sorted values. Because wind cells contain both speed and direction the scalar definition of the median must be extended. One method described by Mardia [20] calculates the median of a vector as the one that minimizes the error between it and the surrounding vectors. Mathematically, the median vector $V(m)$ is the one that minimizes $S(m)$ where

$$S(m) = \sum_{i=1}^{N} \|V(m) - V(i)\|. \tag{5.2}$$

This vector difference is calculated for the N elements in a window around the point being filtered.

Using this definition of median, a median filter is implemented for ambiguity selection. Before running the median filter, the wind field is initialized by selecting an alias for each wind vector cell, U_{ij} (i and j are the along-track and cross-track indices). One method for initializing the fields is to choose the highest ranked alias at each location. More involved techniques have also been developed in which the initial alias is chosen from the first two aliases as the one closest to numerical weather model predictions of the wind field. This process of nudging the data using external wind fields has been shown to be very successful and was used in the NSCAT ambiguity removal algorithm. However, it requires non-scatterometer data to implement it.

Once the field is initialized the selected alias, w_{ij}^k, is the one closest to the median. Thus the alias number is calculated as follows:

$$k = \arg\min_k \sum_{m=i-h}^{i+h} \sum_{n=j-h}^{j+h} W_{m'n'} \| w_{ij}^k - U_{mn} \| \tag{5.3}$$

$$m' = m - i$$

$$n' = n - j$$

where $W_{m'n'}$ is a weighting function for the window, and $(2h+1) \times (2h+1)$ is the size of the window. The selected alias is the one that minimizes the error between it and the surrounding wind vectors. Once w_{ij}^k has been calculated for each cell in the swath, the initial values are updated ($U_{ij} = w_{ij}^k$) and the process is repeated. The process iterates until either none of the vectors change during a pass through the data or a predetermined number of iterations is reached. The end result is a wind field estimate based on the initial field and the available aliases.

One of the greatest advantages of using the median filter for point-wise ambiguity selection is the simplicity and resulting speed of the algorithm. Another advantage of the PWMF is that it retains the edge preserving property of the scalar median filter. Edge preservation ensures that wind features such as storm fronts are retained and not smoothed over. The single biggest drawback to the median filter is

the dependence of the performance on the initial field. The majority of the time the initial field is quite close to the true wind and the filter correctly selects the aliases. However, erroneous sections of the initial field can cause ambiguity selection errors.

5.2.3 The Field-wise Median Filter

The PWMF selects the point-wise alias in the median wind direction. Extending the median filter to the field-wise case requires that we select the field-wise ambiguity that corresponds to the median wind field. To do this we must first define "median wind field".

The median for vector data as defined by Mardia [20] is the vector that minimizes the error between it and the other data points (Eq. 5.2). Using this definition, the vector median is essentially equivalent to the average of the data. The median wind field for field-wise estimation can also be thought of as the average wind over the WFR.

The problem becomes finding a way to determine the average wind flow using the aliases in each WFR in the swath. In the PWMF the median is found using a window over several wind vector cells. Likewise, the median is calculated in FWMF using a large window overlapping several WFRs around the region in question. This window is illustrated in Figure 5.3. Next, each WFR in the window is initialized to a predetermined alias. The aliases can be initialized using the highest ranking aliases or using nudging techniques similar to those used in PWMFs. Using the initial values, a continuous field of wind is generated by overlapping and averaging the selected initial aliases. This wind field represents the initial wind field for the median filter. Because it is likely that some of the WFRs are initialized to the wrong alias the initial field may not perfectly represent the true wind, but as long as a majority of the regions in the window are initialized correctly the general flow of wind should be close to the true. To ensure that no high frequency wind features resulting from incorrectly initialized WFRs influence the median wind field the large field is low-pass filtered. The end result is a low frequency, average wind flow over the region. The area of the

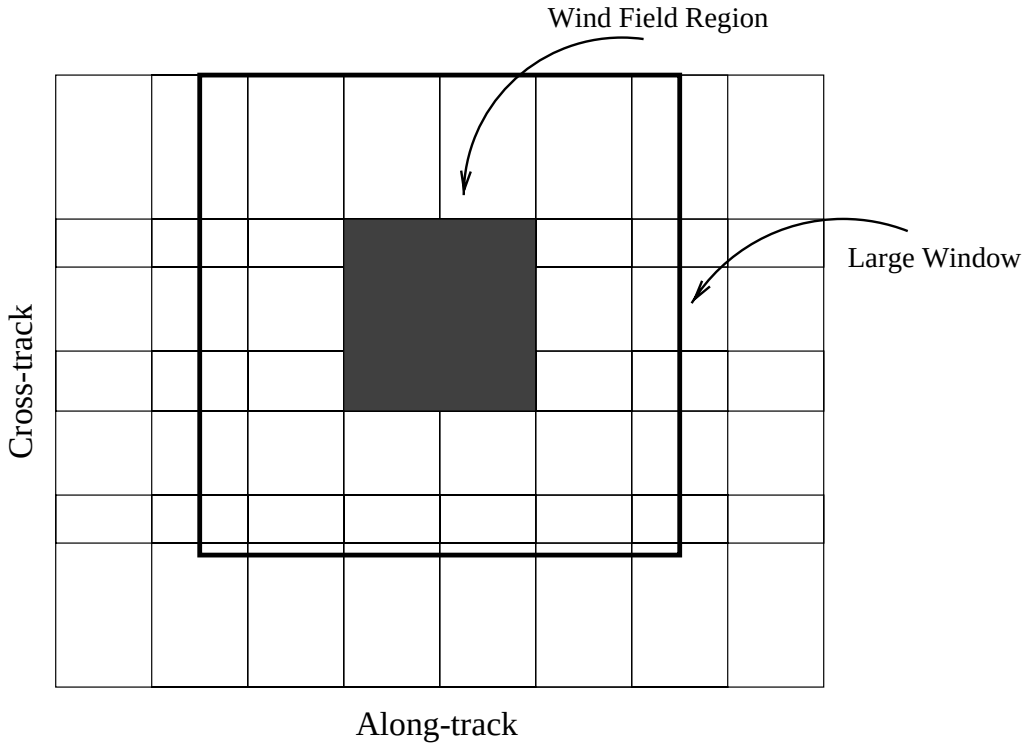

Figure 5.3: *Typical window size used to determine the median wind.*

average wind field directly over the WFR being filtered is extracted, column scanned and designated W_{median}.

For this algorithm the low-pass filter is implemented by performing a least-squares fit of a low order Fourier wind model [7] to the initial wind field. The Fourier basis wind model fits Fourier polynomials to the wind field. Using low order Fourier polynomials ensures that the high frequency components of the wind are filtered. The Fourier model size is chosen to match the size of the window, typically 2 to 3 times the size of a WFR. Figure 5.4 shows a section of wind obtained by overlapping and averaging the first aliases in each WFR. Figure 5.5 shows a low-pass filtered version of the wind in Figure 5.4. The wind is filtered using a third order, 67×67 Fourier model fit to the original wind field. The median wind field is found by column scanning the section of the average wind field corresponding to the region in question.

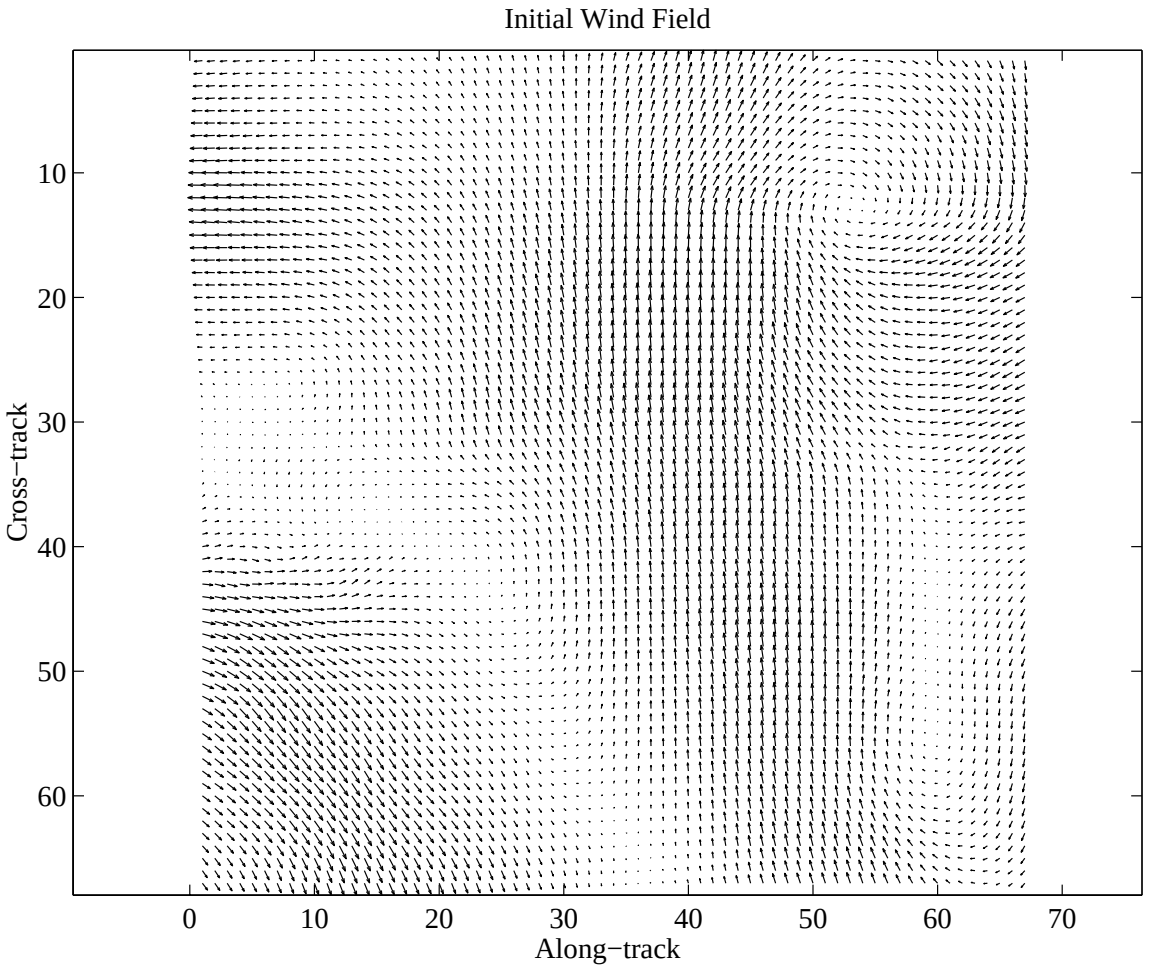

Figure 5.4: *The initial wind field formed by averaging the overlapping regions of wind.*

5.2.4 Implementation of the Median Filter

The details of implementing the median filter in field-wise ambiguity selection are illustrated using the pseudocode algorithm in Figure 5.6. Like PWMFs the first step in median filtering is to initialize the entire swath. For field-wise data it is shown in Chapter 4 that close to 73% of the first aliases are the correct aliases. Using this fact, a logical choice for the initial field is first alias of each region.

With the initial aliases selected we now apply the median filter to each WFR in the swath. First, the initial wind field is created from the initialized wind aliases by

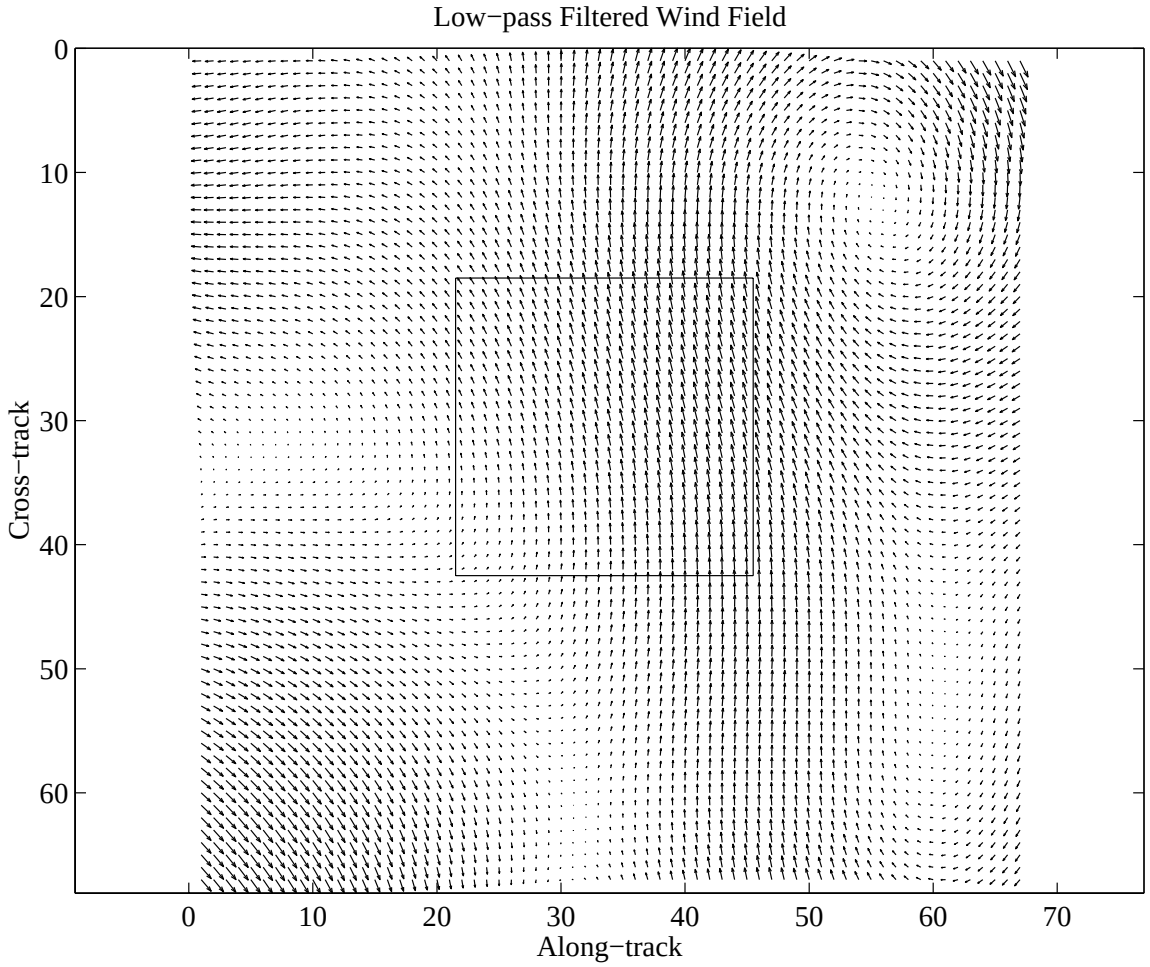

Figure 5.5: *The low-pass filtered wind field. The wind in the box is the median wind field corresponding to the region being filtered.*

overlapping and averaging each wind alias with the aliases in the surrounding regions. Once the initial field is generated the true wind flow is estimated using the median filter. The median wind field, W_{median}, for each region is calculated using the initial wind field and a low order Fourier model, as described above. The alias, k, for the region is selected as follows:

$$k = \arg\min_{k} (\hat{W}^{(k)} - W_{median})^T (\hat{W}^{(k)} - W_{median}). \tag{5.4}$$

In other words, the selected alias is the one closest to the median wind field. Figure 5.7 shows the median wind field calculated in Figure 5.5 and the first four field-wise

```
initial_k(:)=1
changed=true
it = 0
while(changed & it < max_iteration)
  changed = false
  initial_field=Compute_field(initial_k)
  for i=1:number_of_regions
    W_median=Compute_median(i,initial_field)
    for k=1:number_of_aliases(i)
      overlap_error(k)=Compute_error(W_median,alias(i,k))
    end
    chosen_k(i)=index(min(overlap_error))
    if chosen_k(i) != initial_k(i) then
      changed=true
    end
  end
  it = it + 1
  initial_k = chosen_k
end
```

Figure 5.6: *Pseudocode implementation of the field-wise median filter.*

aliases. In this case the first alias is selected as the closest to the median field. This step is repeated for each WFR in the swath.

Once the entire swath has been filtered the initial field is updated using the selected aliases from the first pass. The median filter is again implemented on the swath. This process is repeated until either none of the filtered aliases change or a maximum number of iterations is reached. The final result is a swath of wind formed from the best fitting combination of the aliases for each region.

5.2.5 Optimizing the Median Filter

To optimize the median filter, multiple sizes and orders of the Fourier wind model are tested on three swaths to see which performs the best. In this test the vector RMS error between the true wind field and the filtered wind field is compared. The percentage of times that the alias "close" to the true wind was selected is also calculated. In calculating this percentage the solutions are classified as "close" if the vector RMS error between it and the true is within 1 m/s of the vector RMS

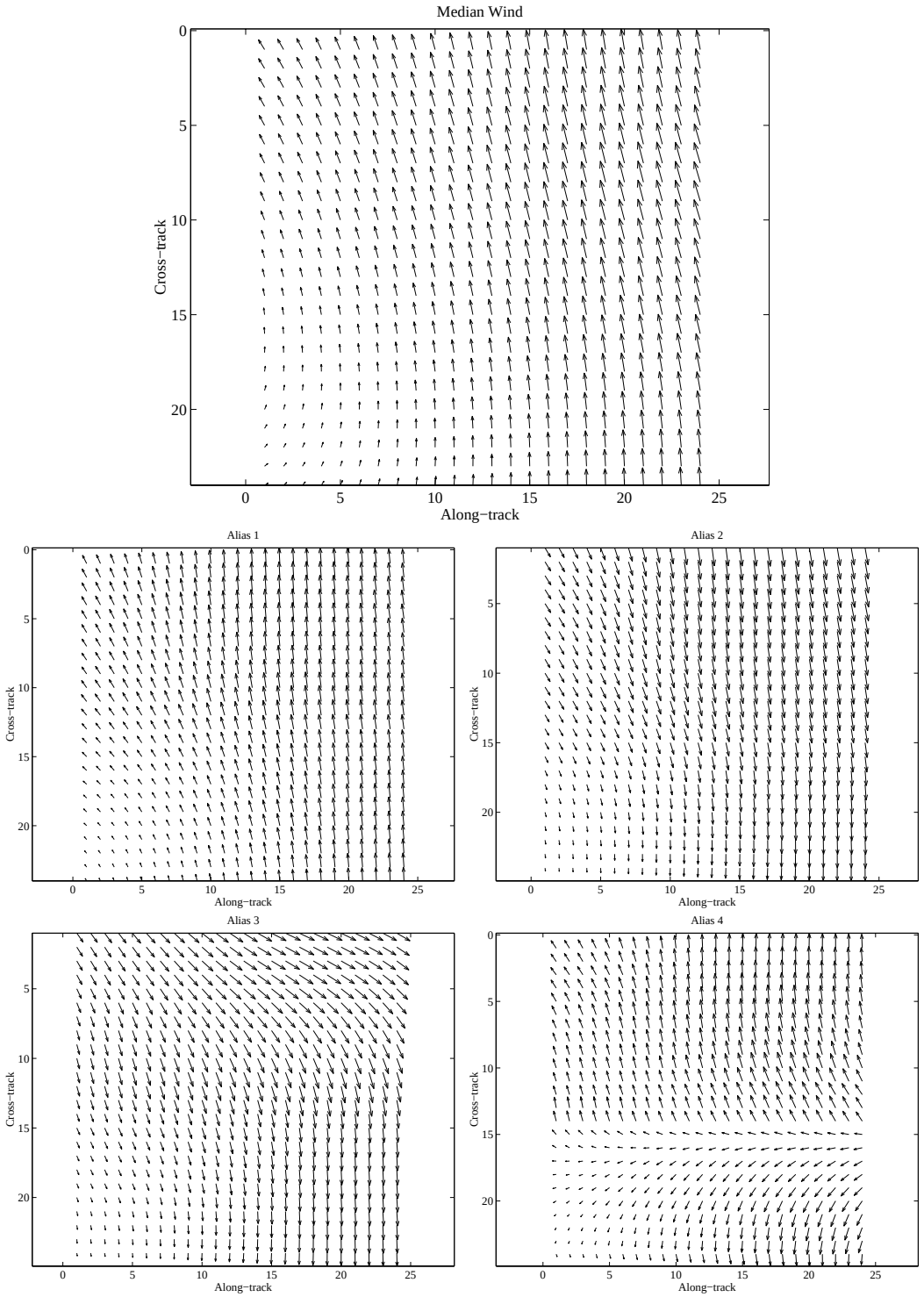

Figure 5.7: *The median wind field and and first four field-wise alias. Using a median filter the first field-wise alias is selected as the true wind.*

error of the closest alias and the true wind. The performance of the FWMF using the different Fourier models is presented in Table 5.1. As a noted in the previous chapter, field-wise estimation is not very accurate for low wind speed winds. In fact, Gonzales [19] showed that winds below 4 m/s have large estimation errors. For this reason the percentage of close regions is only calculated for fields with average wind speeds greater that 4 m/s.

Table 5.1: *FWMF performance for various Fourier models.*

FWMF Performance			
Model Order	Model Size	Vector RMS Error	% Correct FW Aliases
3	48×48	1.76	94.4%
3	52×52	1.71	95.1%
3	57×57	1.73	92.3%
3	62×62	1.72	92.6%
3	67×67	1.71	94.0%
4	48×48	1.78	93.3%
4	52×52	1.76	94.4%
4	57×57	1.76	94.4%
4	62×62	1.75	94.4%
4	67×67	1.72	94.8%
4	72×72	1.73	93.7%
4	76×76	1.74	92.6%

Overall, the third order models perform better than the fourth order models. Of the third order models the 67×67 Fourier model and the 52×52 Fourier model have the best performance. The 67×67 Fourier model is chosen because is spans a larger area providing more stability to the filter.

5.2.6 FWMF Performance

To estimate the performance of the FWMF, 1060 regions from 7 different swaths of simulated data are processed and the results are presented in Table 5.2.

In this table the percentage of WFRs close to true after being initialized to the first alias is compared with the resulting percentage of WFRs that are close to the true after the median filter is implemented (here, close is defined as any region where the RMS vector error between the selected alias and the true wind is within 1 m/s of the RMS vector error between the closest alias in the set and the true wind). The vector RMS error for all the regions is given. A final statistic, termed PW accuracy, is the percentage of time that the point-wise alias closest to the true wind is also the closest to resulting model-based wind field from the median filter. The point-wise accuracy is computed only for vectors with wind speeds greater than 4 m/s.

Table 5.2: *Overall FWMF performance.*

FWMF Performance			
Initial Correct	Filtered Correct	Vector RMS Error (m/s)	PW Accuracy
70.3 %	83.3 %	2.54	95.4%

The FWMF improves the percentage of selected ambiguities that are close to true by 13%. The final percentage of 83.3% is good but not good enough to justify the use of field-wise wind retrieval algorithms. To further improve the ambiguity selection for field-wise wind retrieval an addition step must be taken.

5.3 Nudging the Median Filter

Like the PWMF the performance of the FWMF is intimately linked with the accuracy of the initial field. Both the percentage of initial FWRs that are close to the true wind and the location of the erroneous initial values play important roles in determining the true wind. The performance of the PWMF was improved in NSCAT ambiguity selection by "nudging" the initial field using numerical weather models. To nudge the wind the initial field was calculated by choosing from the first two aliases the alias closest to the wind flow predicted by a numerical weather model. In a similar

fashion additional information can be used to "nudge" the field-wise estimates and improve the overall performance. This section describes three different methods for improving the performance of the FWMF.

5.3.1 Nudging with External Data

Similar to point-wise nudging, an initial field can be generated by choosing the initial alias in each region as the one closest to a numerical weather model field. To test this method the simulated wind fields are low-pass filtered to a spatial resolution of 250 km, the same resolution as most numerical weather models. The initial field is then created using the field-wise aliases closest to the low-pass filtered winds. The same 1060 regions are tested using this nudging and the results are presented in Table 5.3.

Table 5.3: *FWMF performance using nudging from external data.*

External Nudging		
FW Amb. Selection	Vector RMS Error (m/s)	PW Accuracy
92.0 %	1.96	97.0%

As expected the results are significantly better. In fact, the initial field is actually closer to the true field with 96.7% of the WFRs close to the true, while only 92.0% of the filtered WFRs are close to the true. In spite of this the vector RMS error is much lower than the previous FWMF results and the PW accuracy is better by almost 2%. Admittedly this simulation produces more optimistic results than the nudging to be used with numerical weather models because the wind fields are essentially nudged with the true wind, but this test illustrates the potential for improving FWMF performance using external data.

5.3.2 Nudging with Point-wise Winds

We note that in the tests of the FWMF performance given in Table 5.2 the point-wise accuracy is a remarkable 95.4%. This means that even though many of the individual WFRs have ambiguity selection errors the overall flow of the wind is close to the true wind. This section explores several different methods for improving the field-wise ambiguity selection using the closest point-wise aliases. These method are referred to as internal nudging or point-wise nudging.

The first step in point-wise nudging is to generate a point-wise wind field by choosing the point-wise aliases that are closest to the model-based estimate from the FWMF. The result is a point-wise vector field (PWVF) with a wind flow close to the model-based estimate. Next regions of the PWVF corresponding to each WFR are selected and labeled $W_{pw,i}$, where i is the WFR number.

The first point-wise nudging method uses $W_{pw,i}$ to nudge the final wind estimate. This is done by comparing each field-wise alias in each region with its corresponding $W_{pw,i}$ and choosing the alias closest to $W_{pw,i}$ as the final estimate, thus nudging the final field. This method is designated PW Nudge and the performance is given in Table 5.4.

Another nudging method uses a least squares model fit on each $W_{pw,i}$. The resulting model parameters X_i are then used as the initial values for a steepest descent optimization of the objective function. The optimization generates one new field-wise alias for each WFR. This process of creating new wind aliases using point-wise winds is illustrated in Figure 5.8. The top plot is a field-wise estimate for a single WFR, the bottom left plot is the corresponding closest point-wise field, $W_{pw,i}$, and the bottom right plot is the alias resulting from the optimization. Once the new aliases have been created they are included in the set of all aliases and the final estimate is selected as the alias closest to the point-wise field. This approach is called PW Optimized and the performance is given in Table 5.4.

The final approach is to use the newly created aliases to form a new initial field for the FWMF. The FWMF is implemented again and the resulting wind field is used as the final wind estimate. This is referred to as Opt-FWMF in Table 5.4.

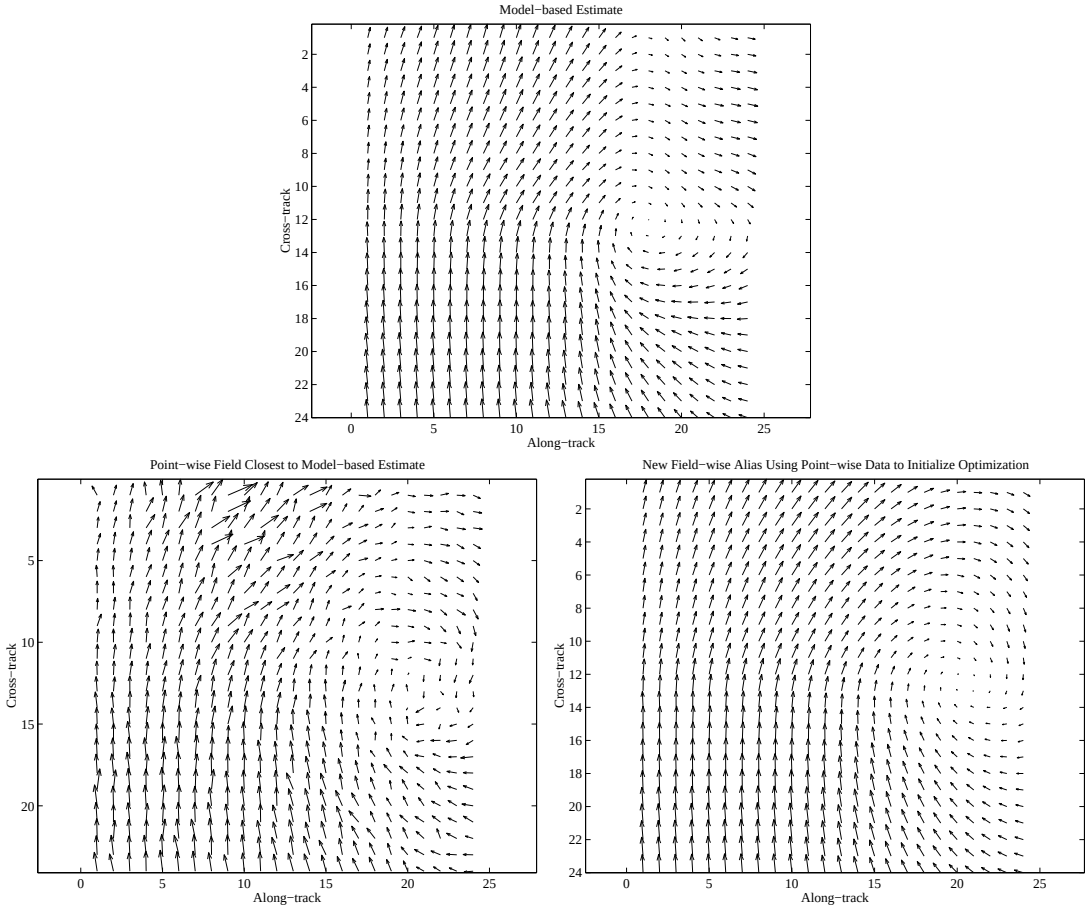

Figure 5.8: *An example of nudging with point-wise wind fields.*

A test is performed using the same 1060 regions with the three point-wise nudging techniques implemented. The results are displayed in Table 5.4. Of the three methods described above, point-wise nudging of the final field with the newly created aliases included in the set of aliases performs the best though none of the result are significantly better than the results without point-wise nudging.

5.3.3 Nudging with Point-wise Median Filtered Winds

A slight variation of nudging using PWVFs is to run the PWMF on the point-wise vector field before nudging. A test on these 1060 regions shows that the PWMF improved the number of correct point-wise aliases from 95.4% to 96.5%. Using the filtered point-wise estimates should further improve the ambiguity selection. Table 5.4 contains the results of this method on the same regions using PWMF nudging.

PWMF nudging both improves the number of correct field wise aliases selected and reduces the average vector error between the modeled field and the true wind. Of the three PWMF nudging methods PWMF nudging using the optimization performs the best. It minimizes the error and has the maximum percentage of correct point-wise aliases. Overall, using PWMF fields to nudge the data improves the performance of the field-wise ambiguity selection.

Table 5.4: *FWMF performance using different forms of point-wise nudging.*

PW Nudging			
Method	FW Amb. Selection	RMS Error (m/s)	PW Accuracy
PW Nudge	83.1 %	2.45	95.4%
PW Optimized	92.6 %	2.47	95.4%
PW Opt-FWMF	92.2 %	2.52	95.1%
PWMF Nudge	88.0 %	2.41	95.6%
PWMF Optimized	95.0 %	2.37	95.8%
PWMF Opt-FWMF	92.3 %	2.46	95.4%

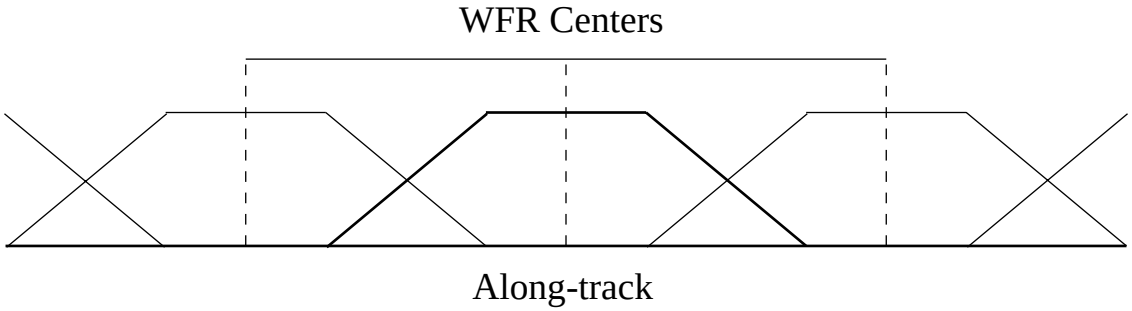

Figure 5.9: *The along-track weighting used in overlapping and averaging the WFRs together.*

5.4 Combining Wind Field Regions

Once the ambiguities have been selected using the median filter and a nudging technique, the final wind field is generated by combining the estimates in each WFR in the swath. Because each region overlaps its neighbors the final field is formed using a weighted average of the overlapping sections. Figure 5.9 illustrates the along-track weighting used where the regions overlap by 50%. A similar weighting is used as the regions are averaged together in the cross-track direction. The final result of the overlap and average stage of field-wise ambiguity removal is a single, smooth estimate for the wind over the entire swath.

5.5 Ambiguity Selection Performance

In this chapter several components of the ambiguity selection algorithm are described and tested. A FWMF is used to choose from the set the aliases closest to the true wind. The optimal Fourier model size for low-pass filtering the median wind fields is shown to be a third order 67×67 model.

Using the FWMF improves the percentages of close field-wise aliases by 13%. Because the initial field is only 72.5% accurate, additional processing must be done to improve it. The PWMF nudging algorithm is shown to improve the field-wise ambiguity selection from 83% to 95% while providing the minimum vector RMS error.

Once the ambiguities have been selected the aliases are combined by overlapping and averaging them to form an estimate for the wind field.

To evaluate the performance of this algorithm, 1060 regions are processed and the performance evaluated. Tables 5.5 and 5.6 display the performance statistics for the algorithm compared with the statistics of wind fields with perfect ambiguity selection. The percentage of times that an ambiguity "close" to the true is found is 95.0% for all the regions and 96.6% for regions with an average wind speed greater than 4 m/s. The point-wise skill of 95.8% is close to the 96.9% obtained using the closest ambiguities. The last statistic is the vector RMS error between the wind estimates and the true wind.

Table 5.5: *FWMF performance compared to perfect ambiguity selection performance ($s > 4$ is for speeds greater than 4 m/s).*

FWMF Performance				
Method	FW Aliases	FW Alias (s > 4)	PW Skill	PW Skill (s > 4)
Nudged FWMF	95.0%	96.6%	92.5%	95.8%
Closest Ambiguities	100.0%	100.0%	94.3%	96.9%

Table 5.6: *FWMF performance compared to perfect ambiguity selection performance and the closest point-wise fields.*

FWMF Error	
Method	Vector RMS Error (m/s)
FWMF	2.37
Closest Ambiguities	1.97
Closest Point-wise	2.18

Finally, the test regions are visually inspected to determine the effects of ambiguity removal errors on the final wind field. Overall, the estimates are quite close to the flow of the true wind. However, almost every swath has one section with significant ambiguity selection errors. Fortunately most of the ambiguity errors appear to be clustered together and are easily distinguished by visual inspection of the field of point-wise aliases closes to the model-based field. Figures 5.10, 5.12 and 5.14 are plots of the point-wise vector fields closest to the model-based estimate illustrating three example of regions with ambiguity selection errors. Figures 5.11, 5.13 and 5.15 are enlarged views of these fields showing the sharp transition in wind direction that occurs when there is an ambiguity selection error.

In each case ambiguity selection errors result from groups of adjacent WFRs initializing the median filter incorrectly. The best example of this is illustrated in Figure 5.14. This region is plotted again in Figure 5.16 with the outline of the wind field regions added. In this figure we see that four of the WFRs are selected incorrectly causing the wind to rotate 180°. Figure 5.17 shows the location of the WFRs along with the corresponding ranking of the alias closest to the true wind. Here we see that in the lower middle four regions the aliases closest to the true are of rank two. The first aliases for these regions point in the opposite direction of the true wind. Hence, when the FWMF is initialized to the first aliases this section of wind is initialized in the wrong direction and because so many adjacent regions are initialized the same way the median filter can not correct it. The fact that so many regions of wind in the same area have the first alias pointing in the opposite direction of the true wind also indicates that there may be some types of wind fields that cause the skill of the scatterometer to be reversed, meaning that aliases pointing 180° from the true are ranked higher than those pointing in the same direction as the wind. This phenomenon has been noticed in NSCAT data (D. G. Long, personal communication). More research is required to fully understand and predict regions where such skill reversal occurs.

When ambiguity selection errors occur, a sharp transition in the wind direction is typically found in the field of point-wise aliases closest to the model-based estimate.

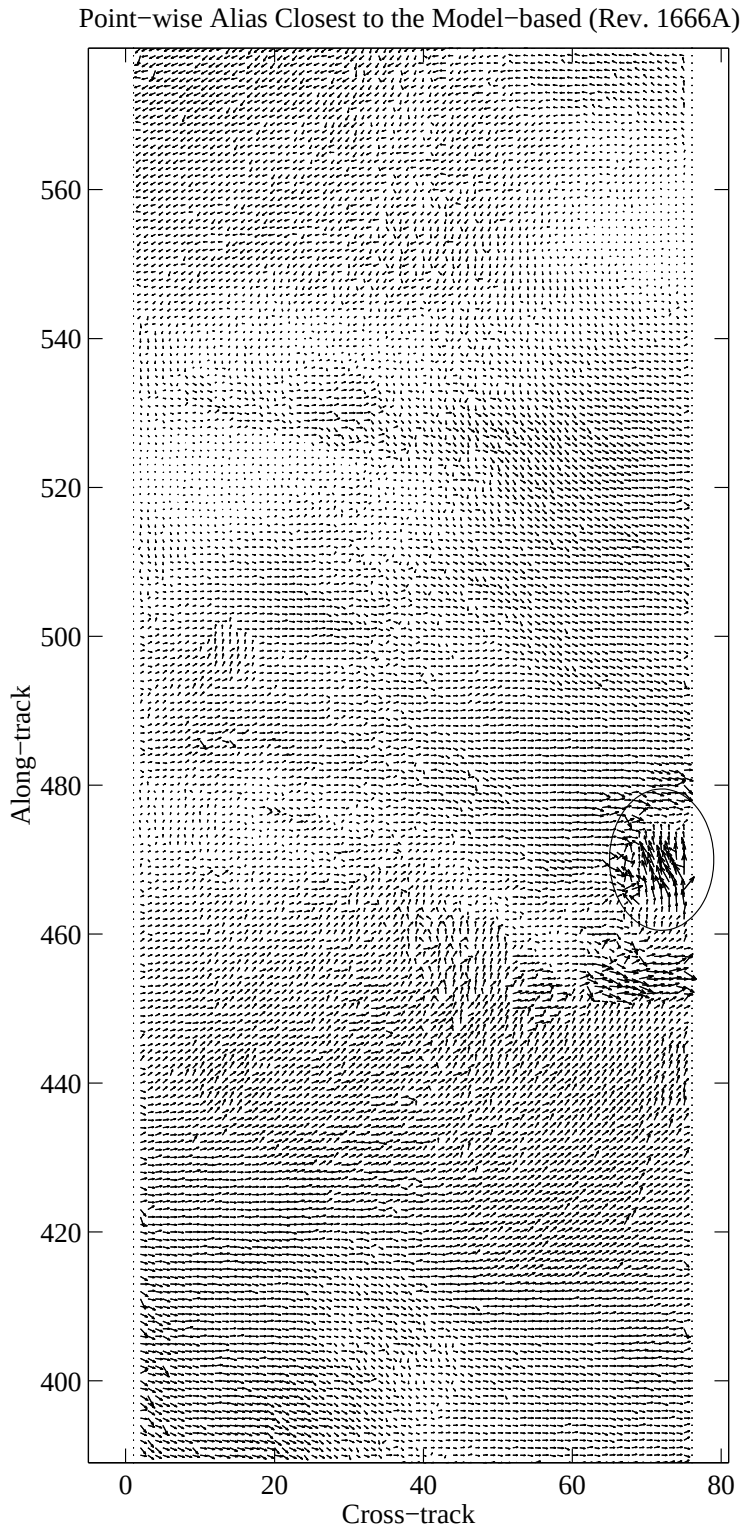

Figure 5.10: *Ambiguity removal errors evident in the point-wise field closest to the model-based winds (Rev. 1666A).*

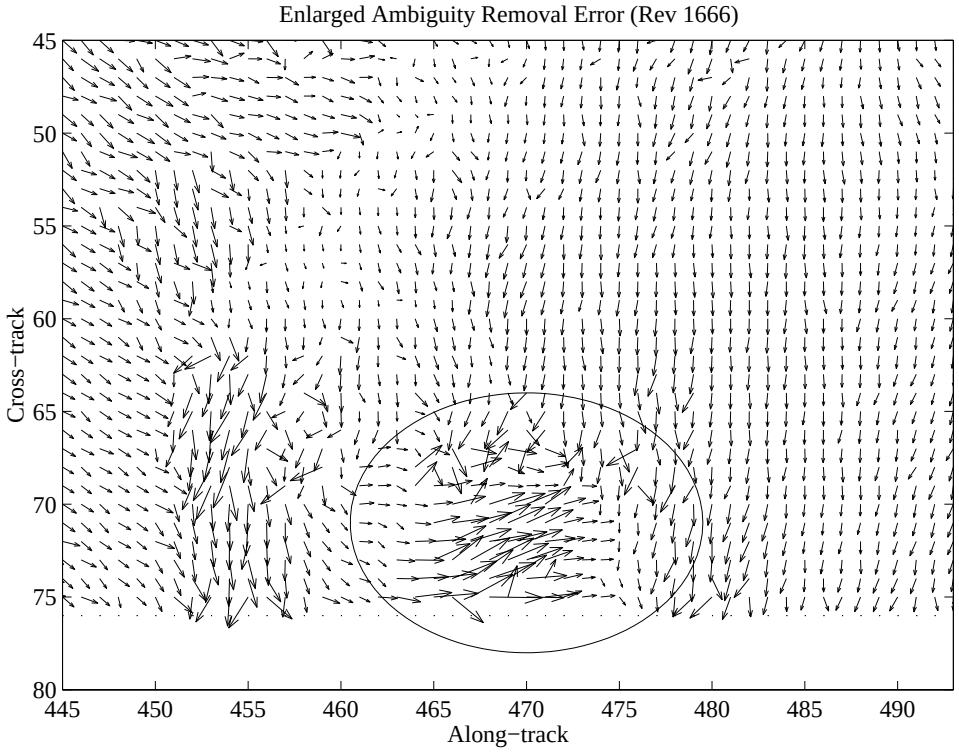

Figure 5.11: *An enlarged view of the ambiguity removal errors shown in Figure 5.10. At the point of the error the point-wise vectors abruptly change direction by about* 90°. *This error results from one field-wise ambiguity being selected incorrectly.*

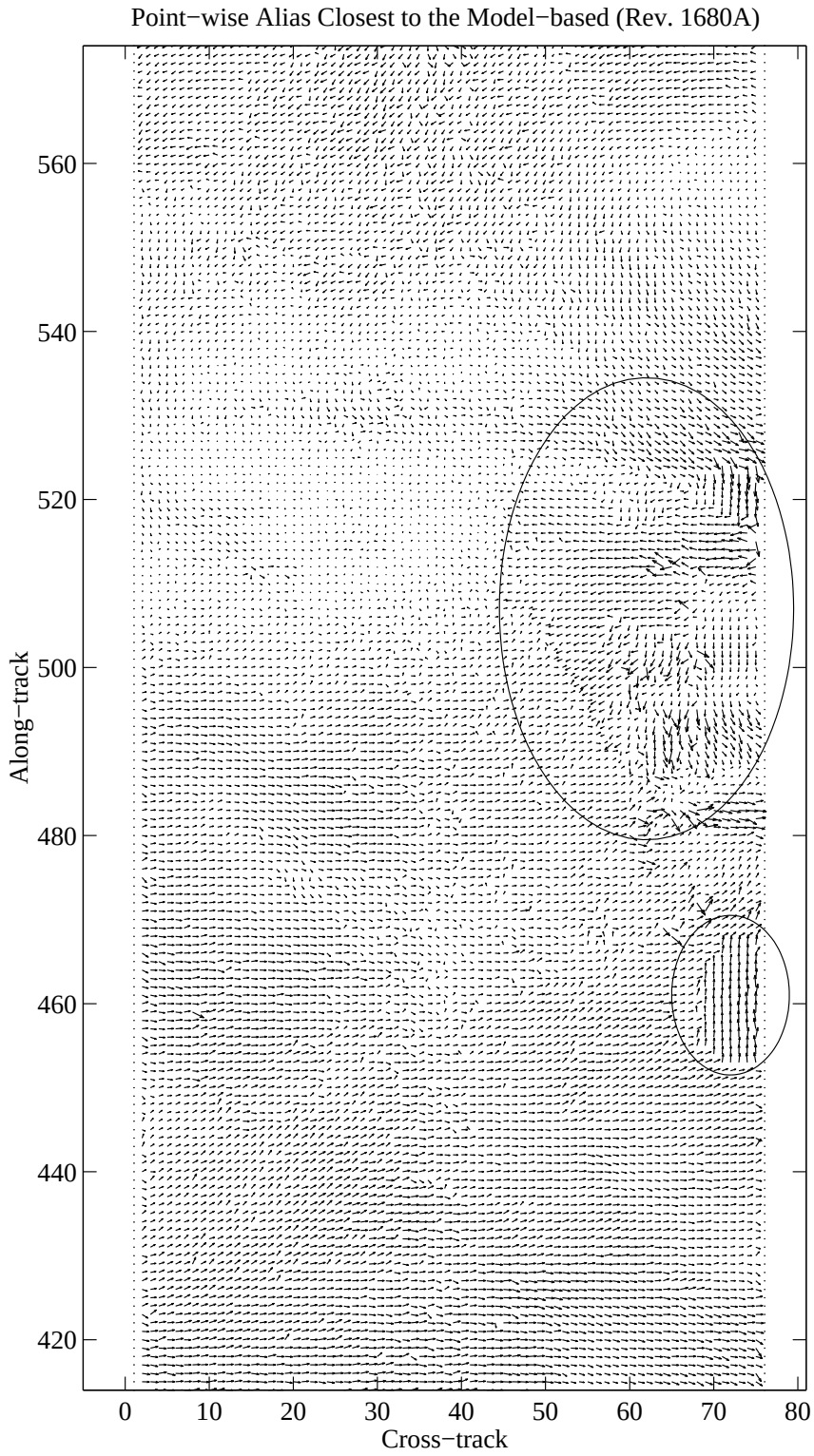

Figure 5.12: *Ambiguity removal errors evident in the point-wise field closest to the model-based winds (Rev. 1680A).*

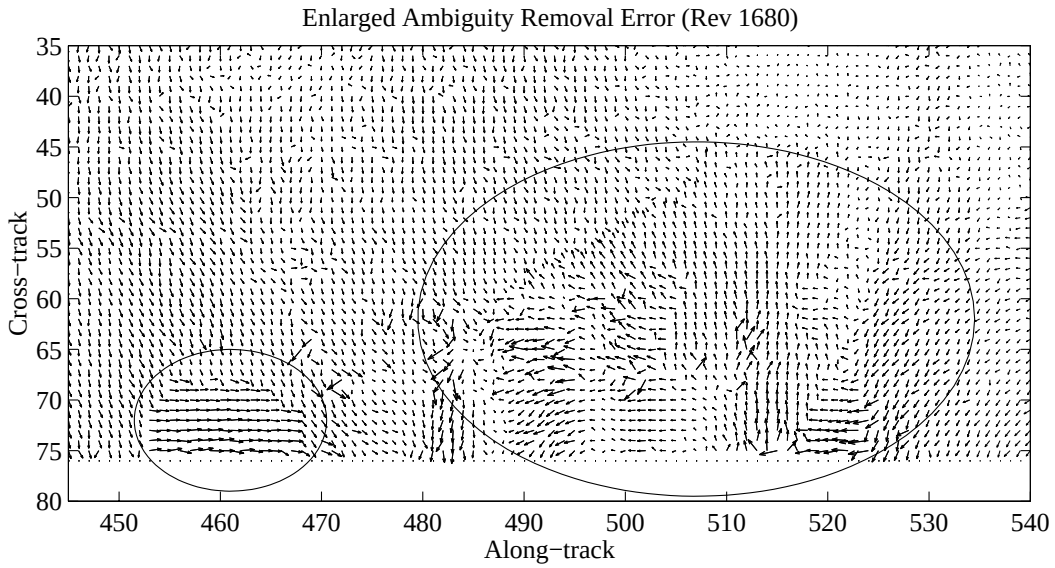

Figure 5.13: *An enlarged view of the ambiguity selection errors shown in Figure 5.12. Here there are two different places where the ambiguity errors are very evident. The area on the left is the result of ambiguity selection error for a single WFR while the area on the right results from 2 incorrectly selected WFRs. Again the areas with ambiguity removal error are easily determined by abrupt changes in the wind directions.*

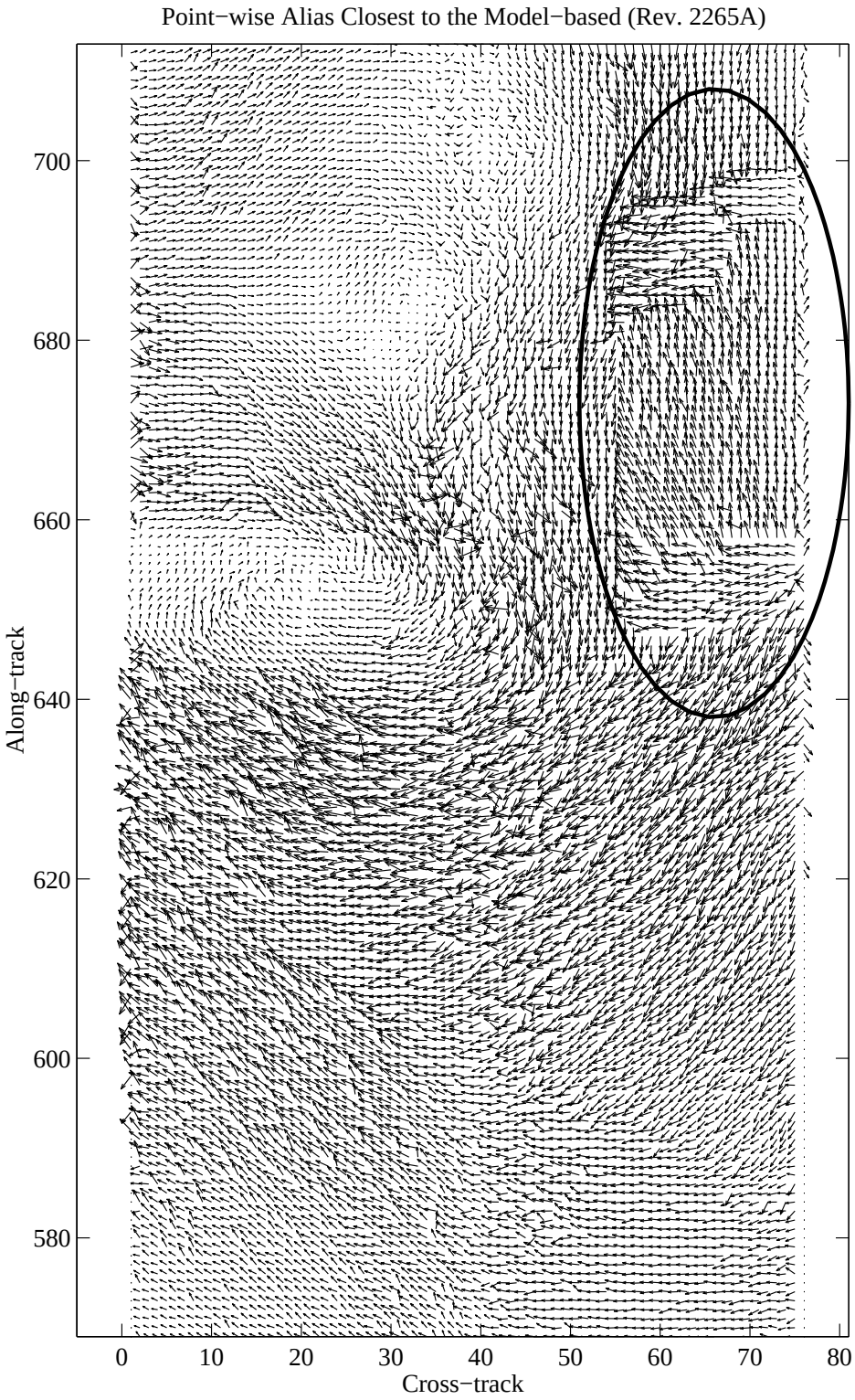

Figure 5.14: *Ambiguity removal errors evident in the point-wise field closest to the model-based winds (Rev. 2265A).*

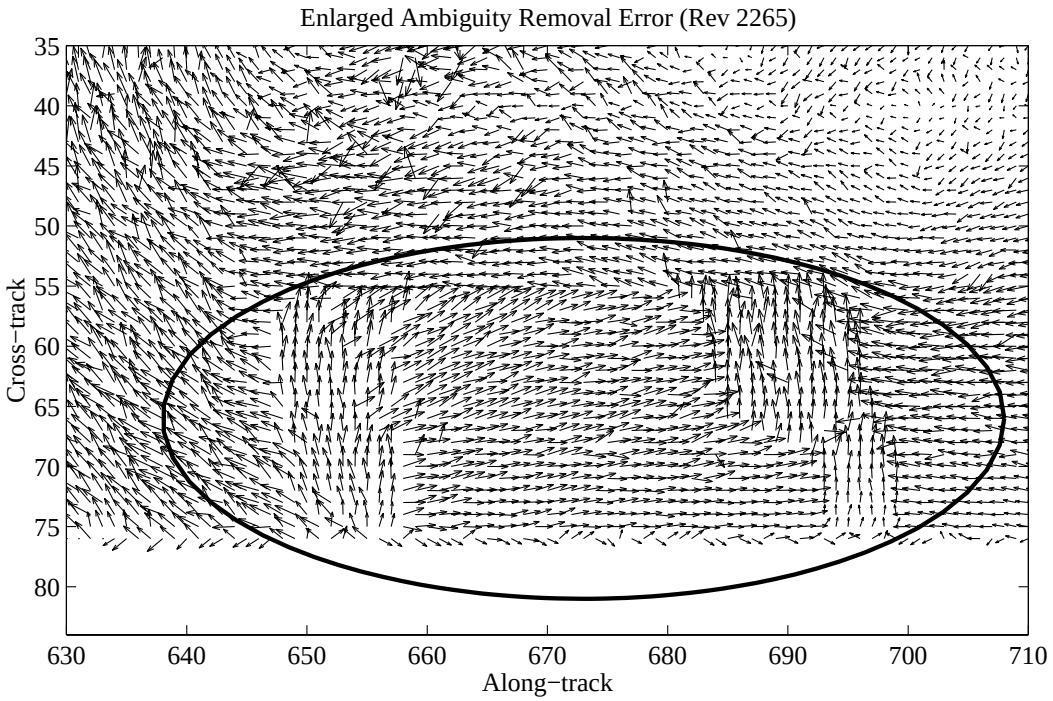

Figure 5.15: *An enlarged view of the ambiguity removal errors shown in Figure 5.14. of all the tested swaths of wind this is the worst case of ambiguity removal. Here 4 adjacent WFRs are incorrectly selected resulting in* 90° *to* 180° *errors in the wind directions.*

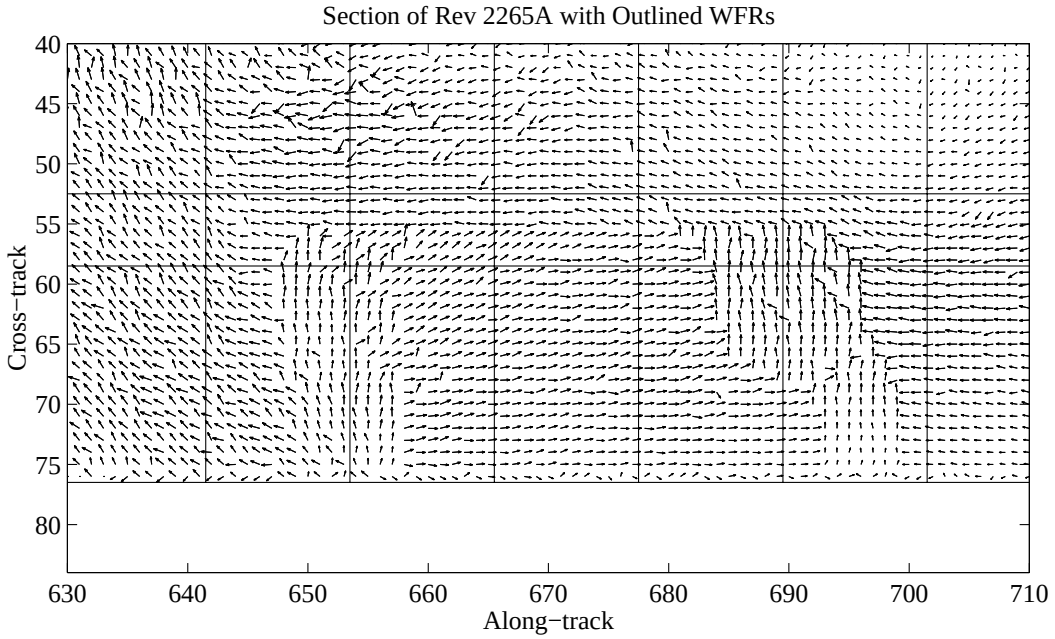

Figure 5.16: *The ambiguity selection error wind from Figure 5.15 with the WFRs outlined. The four WFRs selected incorrectly are easily seen.*

These instantaneous 90° and 180° jumps in wind direction are good indicators of errors. Using these fields it may be possible to create an ambiguity selection error detection algorithm using the principles employed by Gonzales [19], [21] in her quality assurance algorithm for NSCAT. Gonzales compared a low-order model fit to the point-wise fields with the point-wise fields to find wind vector cells where there is a large difference in direction between the two. Using an algorithm like this the sudden changes in direction are easily detected and can then be corrected. It may also be possible to use an edge detection algorithm from image processing on the the vector fields to detect boundaries for sections of wind with ambiguity removal errors.

5.6 Summary

In summary, an ambiguity selection algorithm is presented using only SeaWinds data. Overall the algorithm performs very well selecting an alias close to the true wind 95% of the time. 95.5% of the point-wise vectors closest to the field-wise

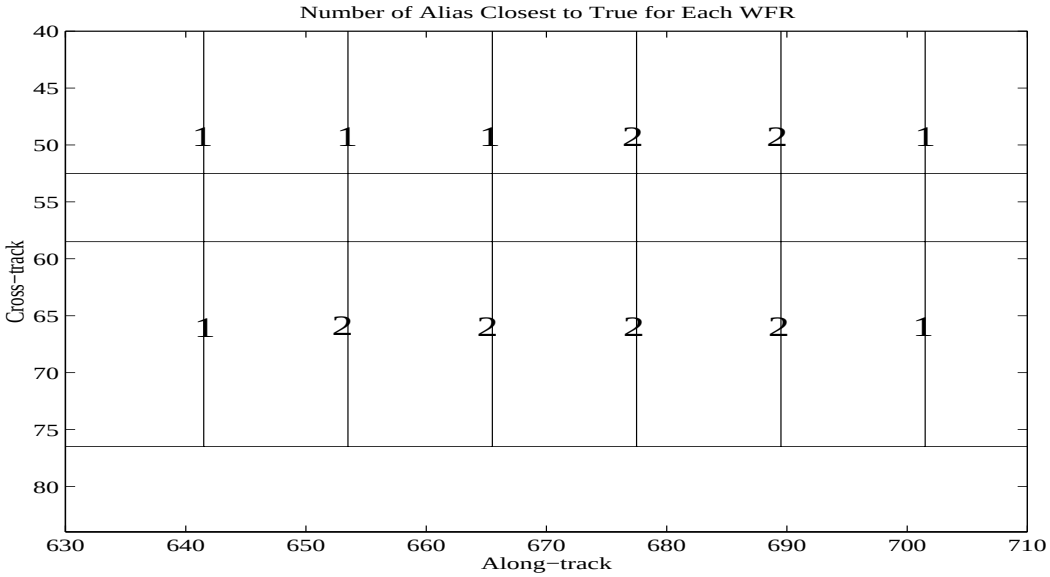

Figure 5.17: *The ranking of the aliases closest to the true wind for the WFRs in Figure 5.16. The ambiguity selection error occured because the field is initialized using the first aliases and here we have a large area where the second aliases correspond to the true wind.*

estimate of the wind are also closest to the true wind making this algorithm a potentially useful point-wise ambiguity selection tool. The errors in ambiguity selection are found to be large when incorrect selection occurs but they often occur in groups that are easily distinguished using the closest point-wise aliases.

Chapter 6

Results

The previous chapters have described the steps required to implement a field-wise wind retrieval algorithm. This chapter uses the algorithms from previous chapters to implement an end-to-end field-wise retrieval algorithm. First, the overall algorithm is described. Next, the algorithm is tested using several simulated data sets. To compare the effects of wind variability on the estimates, both the interpolated NSCAT and modeled NSCAT simulated winds are used and the results are compared.

6.1 The Field-wise Wind Retrieval Algorithm

Figure 6.1 shows a block diagram of the final wind retrieval algorithm. This algorithm takes the simulated σ^o values as the input and produces an estimate of the wind field. The σ^o measurements are generated using the simulated wind fields described in Chapter 3. Using the GMF and instrument geometries, such as incidence angle and azimuth angle, a σ^o value is calculated from the wind speed and direction in the simulated wind field.

The estimates of the wind are found through a global optimization of $p_{\mathbf{Z}}(\mathbf{Z}|\mathbf{W})$. The optimization is performed using a steepest descent algorithm with random starting points. A 22 parameter KL wind field model is used to model the wind and the global search is performed over the 22-dimensional parameter space, X. The multi-start search is further augmented using the the first and second median filtered point-wise fields from the point-wise estimates to compute initial search parameters.

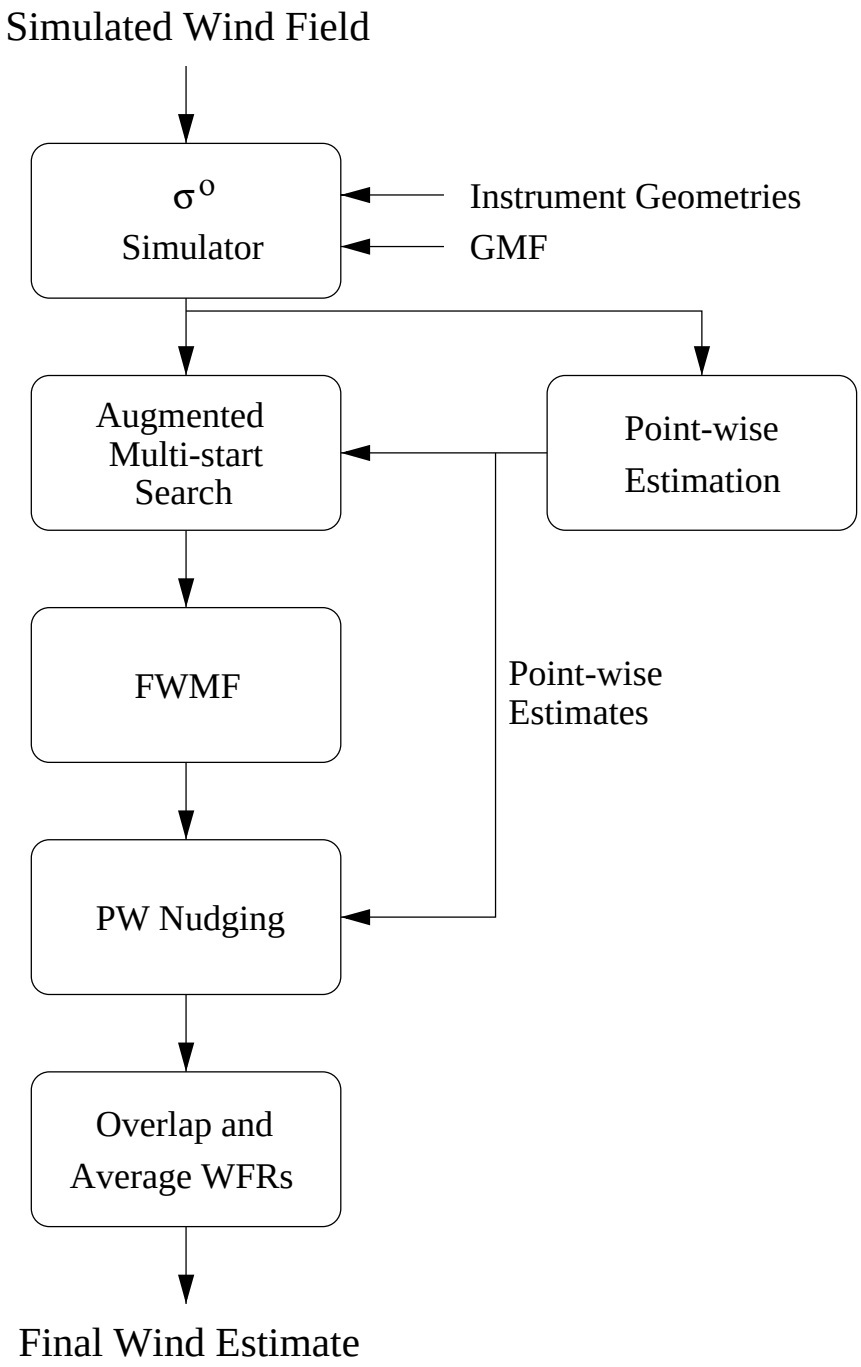

Figure 6.1: *A block diagram of the final field-wise wind retrieval algorithm.*

The result of the augmented multi-start search is a set of possible wind aliases for each WFR in the swath.

The best estimate of the wind is chosen from the set of aliases during the ambiguity selection stage of the retrieval. Ambiguity selection is performed using a field-wise median filter (FWMF) initialized using the first alias in each region. The median wind field for the filter is calculated using a third order 67×67 Fourier wind model. The resulting wind estimate from the FWMF is further improved using point-wise nudging. During nudging the point-wise field closest to the field-wise estimate is generated and an additional optimization is performed using a model fit to the point-wise winds as the initial value. The final wind field is selected by choosing the field-wise aliases closest to the point-wise field. The last step is to take the selected field-wise aliases and average the overlapping regions to form a single smooth wind field estimate.

6.2 Wind Retrieval Performance Using Interpolated NSCAT Winds

The performance of the field-wise wind retrieval algorithm is evaluated using 15 swaths of interpolated NSCAT winds. To demonstrate the accuracy and potential effectiveness of field-wise wind retrieval, three sets of figures are presented.

The first set of plots demonstrate the ideal performance of field-wise wind retrieval versus the ideal performance of point-wise wind retrieval. These figures, numbered 6.2-6.5, show the RMS vector, speed and direction errors for the wind estimates using the best field-wise aliases, the best point-wise aliases and the point-wise aliases closest to the field-wise estimate. These plots represent wind retrieval algorithms with 100% ambiguity selection accuracy and show the potential of field-wise and point-wise estimation. The errors are calculated for winds with speeds of 3-6 m/s, 6-12 m/s, 12-30 m/s and all wind speeds.

In general, field-wise retrieval is slightly less accurate than point-wise wind retrieval in the "sweet spot" of the swath but better in the nadir region and on the edges. Note that the point-wise retrieval error varies across the swath while the field-wise retrieval error remains fairly constant. This constancy is one of the principle

advantages of field-wise estimation. The dips in the model-based performance at the edges of the swath and in the nadir region are most likely due to the smoothness of the extrapolated wind fields in these regions. The magnitude of the error drop is a good indicator of the difference in modeling error for the more variable interpolated winds and the smoother extrapolated winds.

The second set of plots shows the accuracy of field-wise estimation when imperfect ambiguity selection is used. The plots, numbered 6.6-6.9, are comprised of error plots for the same sets of wind speeds as above and show the RMS vector, speed and directions errors in each case.

When ambiguity selection is applied the average error for all wind speeds increases 0.5 to 1 m/s, on average. The worst ambiguity selection errors are reflected in Figure 6.8. In this plot the vector and direction errors increase significantly for cross-track indexes greater than 55. This increase is largely due to ambiguity selection errors where the wind direction is flipped 90° to 180° as illustrated in Chapter 5. An error detection and correction algorithm could help to reduce this error.

Finally, the field-wise estimates created using the FWMF are compared to the closest point-wise fields and to the point-wise estimates obtained using a point-wise median filter initialized with the first aliases. These errors provide a more realistic comparison of the field-wise and point-wise methods as they would actually be implemented. Figures 6.10-6.13 show the vector, speed and direction errors for winds grouped by wind speed, as above.

Compared to the first median filtered point-wise estimates, the field-wise retrieval performs very well. For low wind speeds the point-wise performs better than the model-based in the "sweet spot" but as the speeds increase, the point-wise estimation error increases. However, the field-wise estimation error remains fairly constant. In Figure 6.13 the average error over all wind speeds is best for the field-wise estimates. Figures 6.10-6.13 also illustrate the potential value of using field-wise estimation as an ambiguity selection tool for point-wise data. Table 6.1 lists the percentage of point-wise vectors closest to the true wind that are also closest to the field-wise estimate. This percentage is referred to as point-wise (PW) skill in the table.

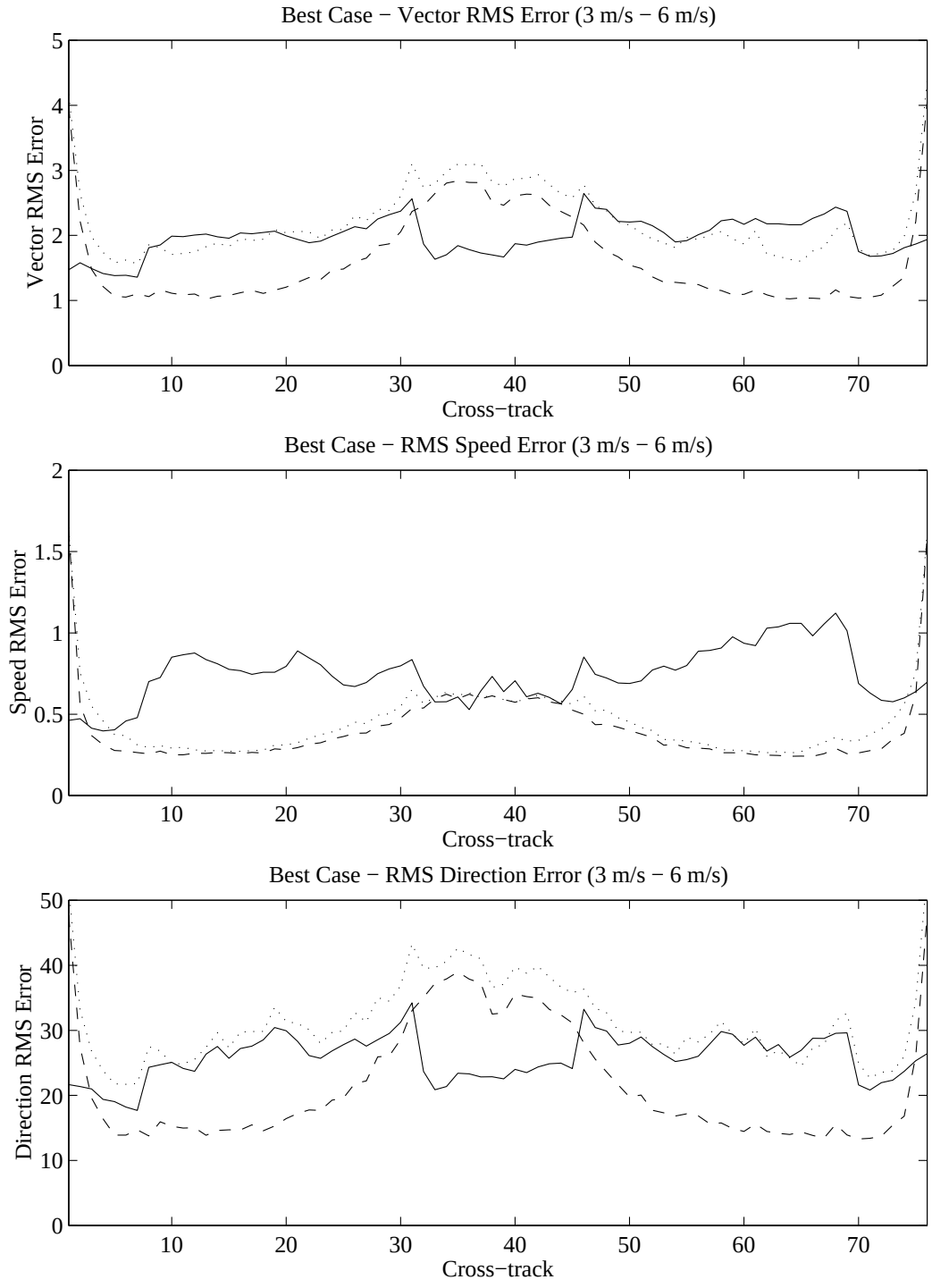

Figure 6.2: *RMS error as a function of the cross-track index for wind with speeds between 3 and 6 m/s. The solid line represents the model-based estimate, the dotted line is the point-wise field closest to the model-based and the dashed line is the point-wise alias closest to the true. These results were generated using interpolated NSCAT winds.*

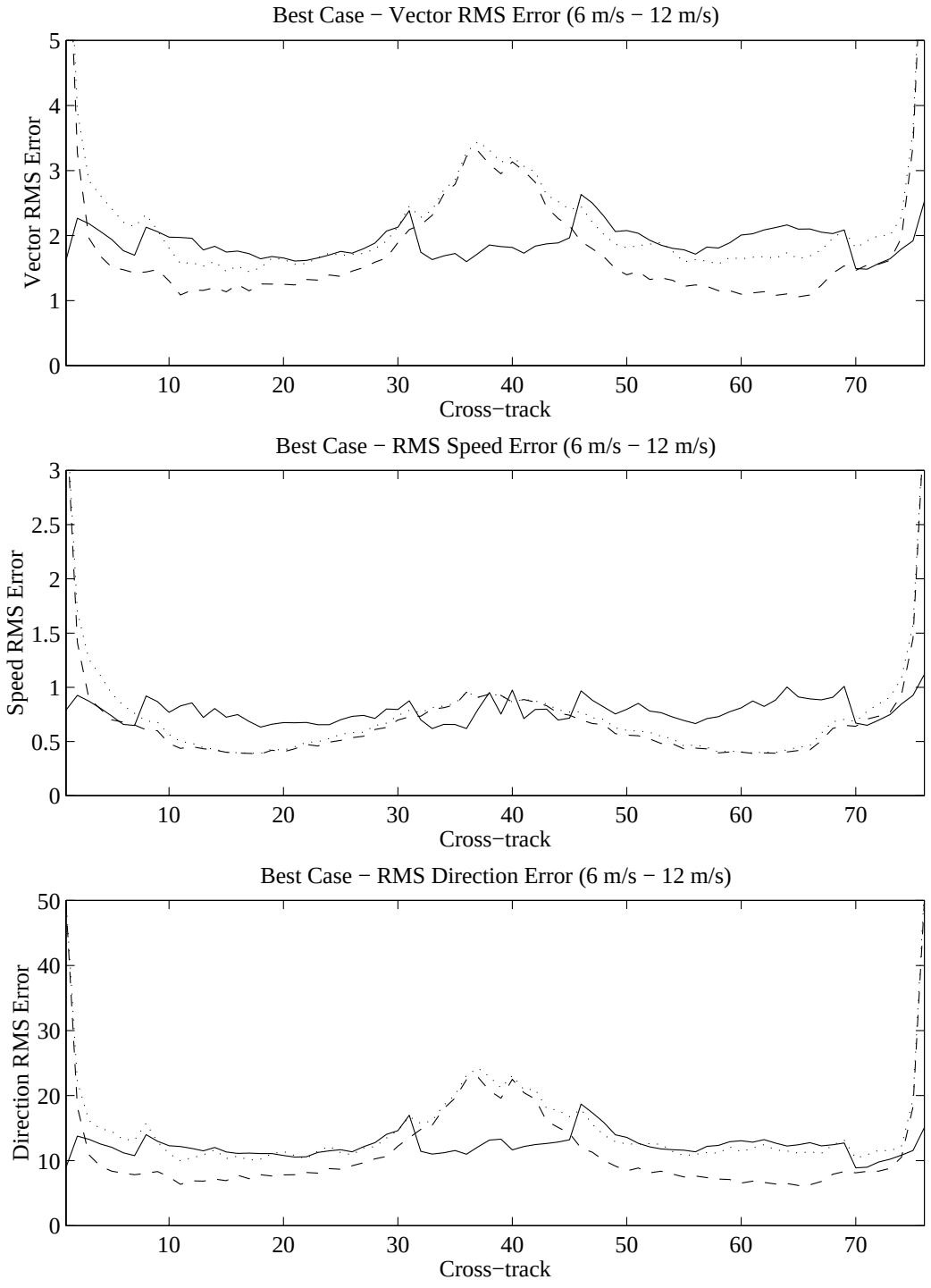

Figure 6.3: *RMS error as a function of the cross-track index for wind with speeds between 6 and 12 m/s. The solid line represents the model-based estimate, the dotted line is the point-wise field closest to the model-based and the dashed line is the point-wise alias closest to the true.*

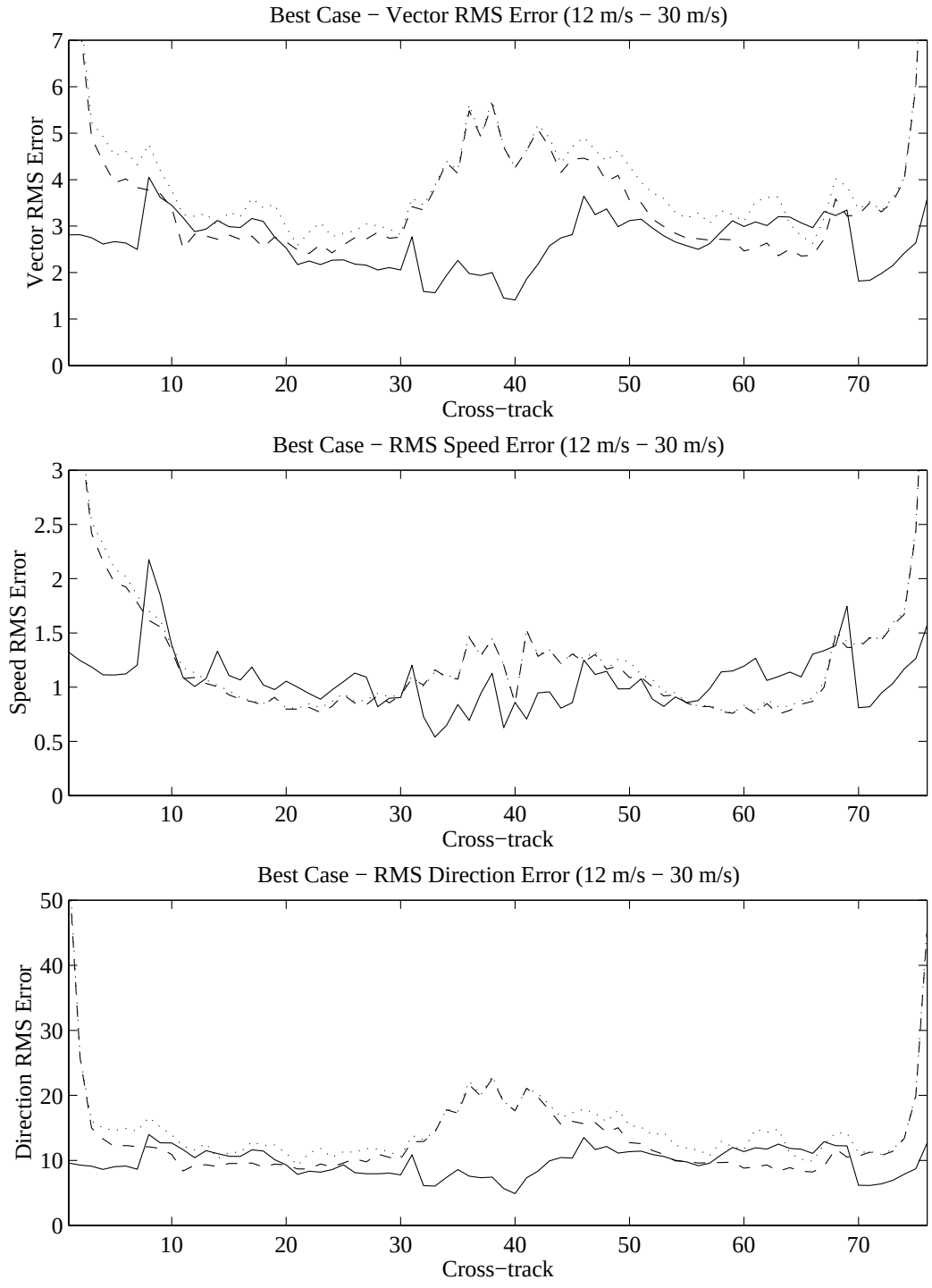

Figure 6.4: *RMS error as a function of the cross-track index for wind with speeds between 12 and 30 m/s. The solid line represents the model-based estimate, the dotted line is the point-wise field closest to the model-based and the dashed line is the point-wise alias closest to the true. These results were generated using interpolated NSCAT winds.*

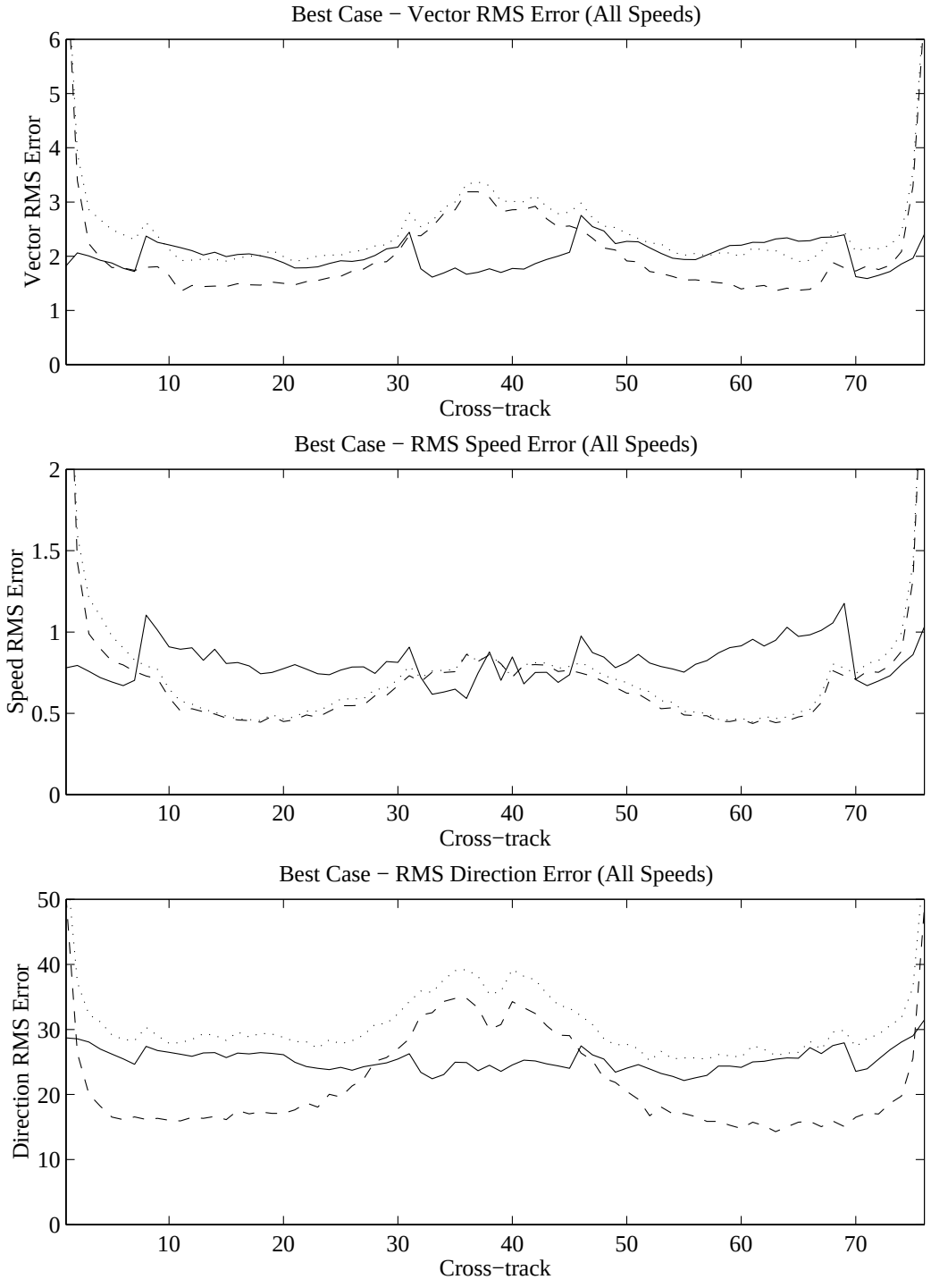

Figure 6.5: *RMS error as a function of the cross-track index for all wind speeds. The solid line represents the model-based estimate, the dotted line is the point-wise field closest to the model-based and the dashed line is the point-wise alias closest to the true. These results were generated using interpolated NSCAT winds.*

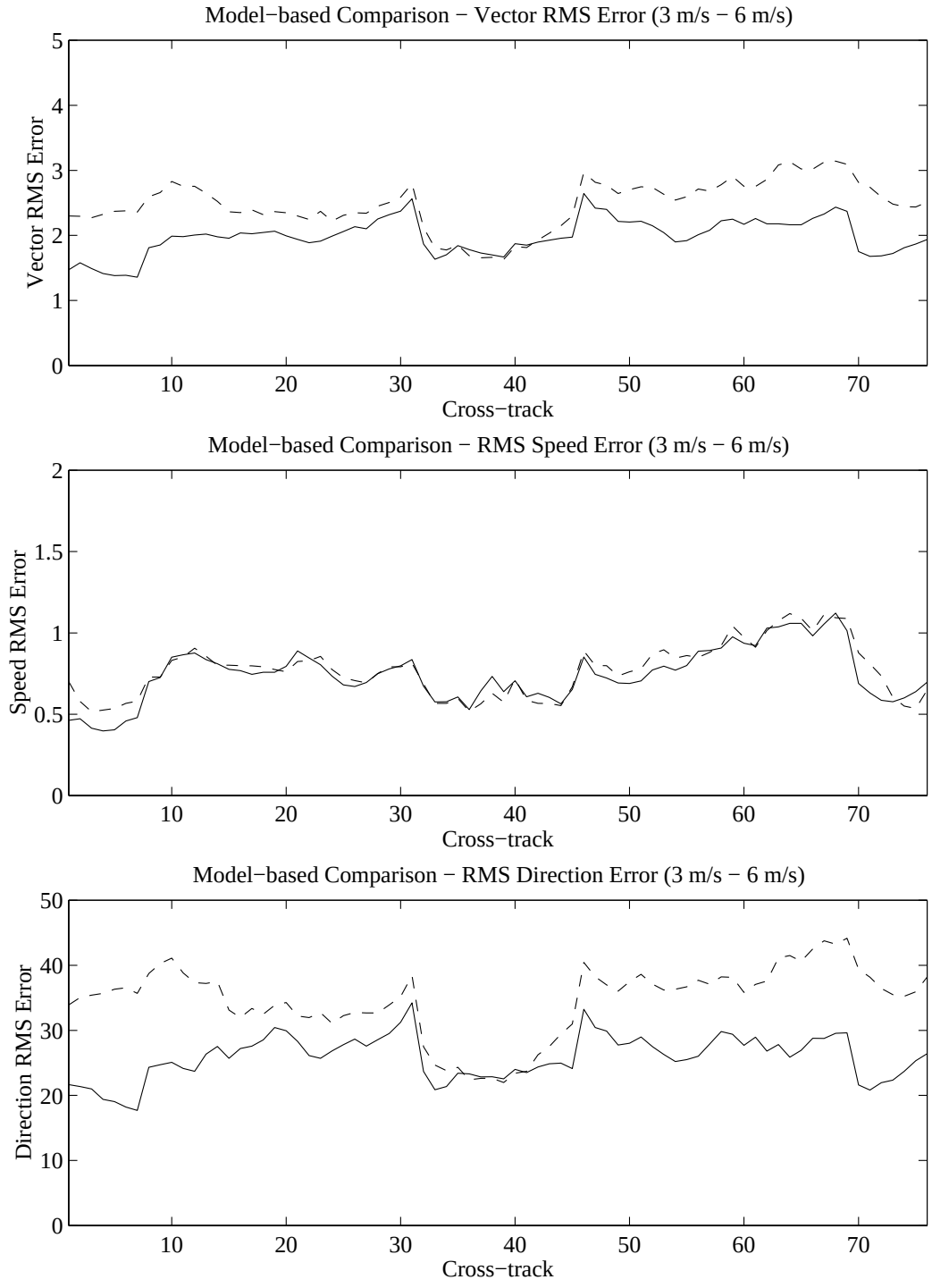

Figure 6.6: *RMS error as a function of the cross-track index for wind with speeds between 3 and 6 m/s. This plot compares field-wise estimation with perfect ambiguity selection to the field-wise estimates using the ambiguity selection algorithm. The solid line represents perfect ambiguity selection while the dashed line includes ambiguity selection errors. These results were generated using interpolated NSCAT winds.*

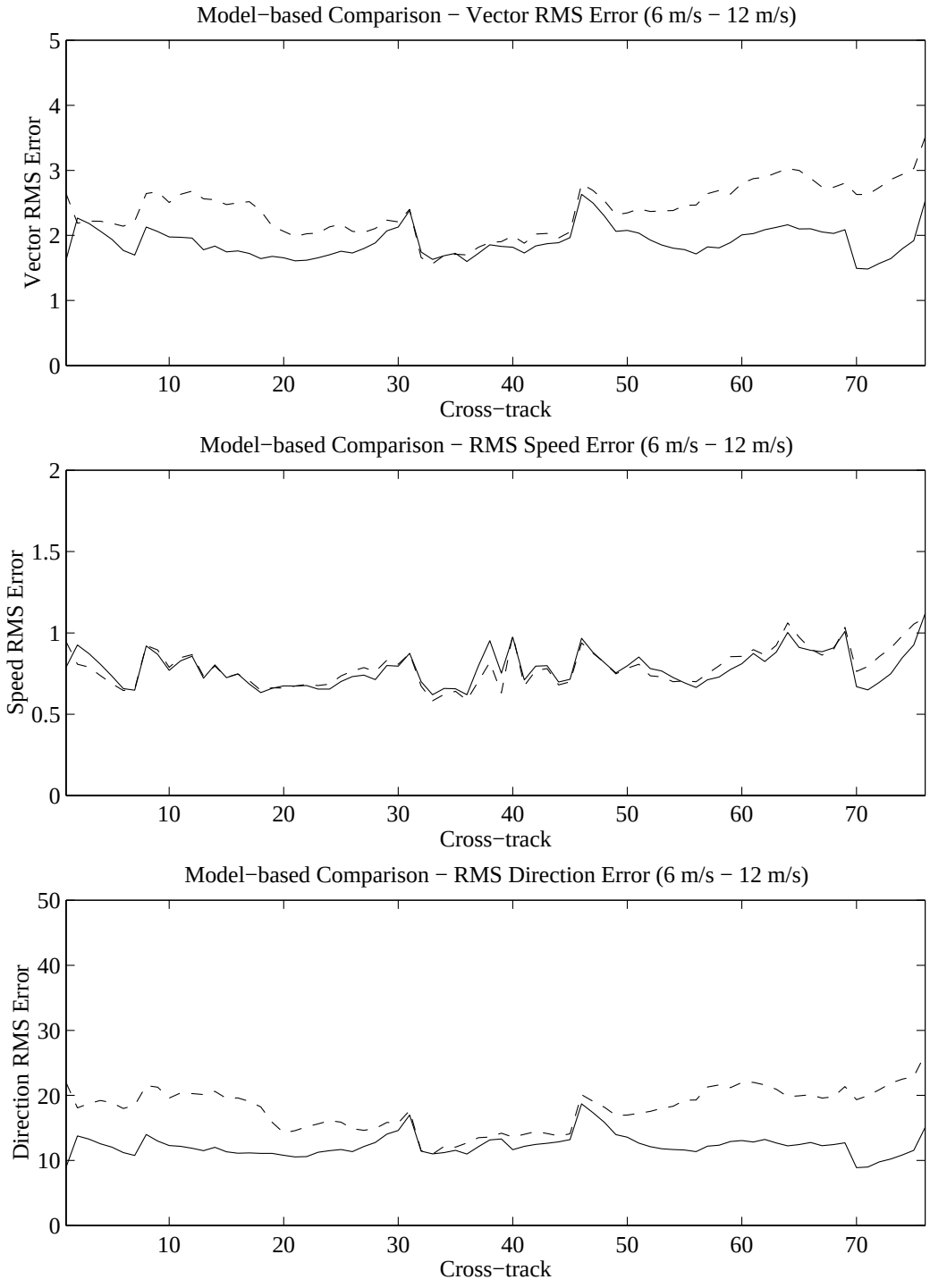

Figure 6.7: *RMS error as a function of the cross-track index for wind with speeds between 6 and 12 m/s. This plot compares field-wise estimation with perfect ambiguity selection to the field-wise estimates using the ambiguity selection algorithm. The solid line represents perfect ambiguity selection while the dashed line includes ambiguity selection errors. These results were generated using interpolated NSCAT winds.*

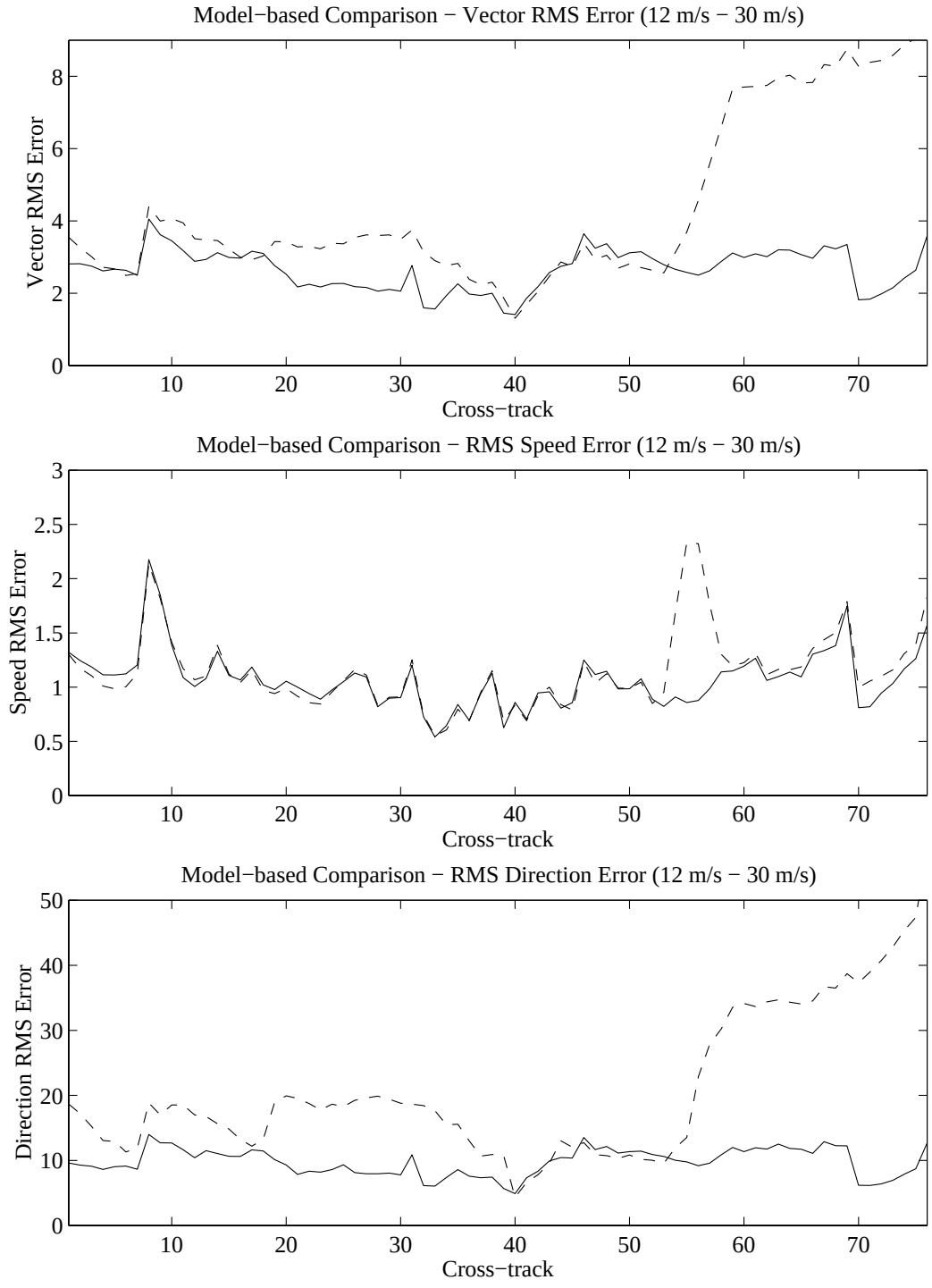

Figure 6.8: *RMS error as a function of the cross-track index for wind with speeds between 12 and 30 m/s. This plot compares field-wise estimation with perfect ambiguity selection to the field-wise estimates using the ambiguity selection algorithm. The solid line represents perfect ambiguity selection while the dashed line includes ambiguity selection errors. These results were generated using interpolated NSCAT winds.*

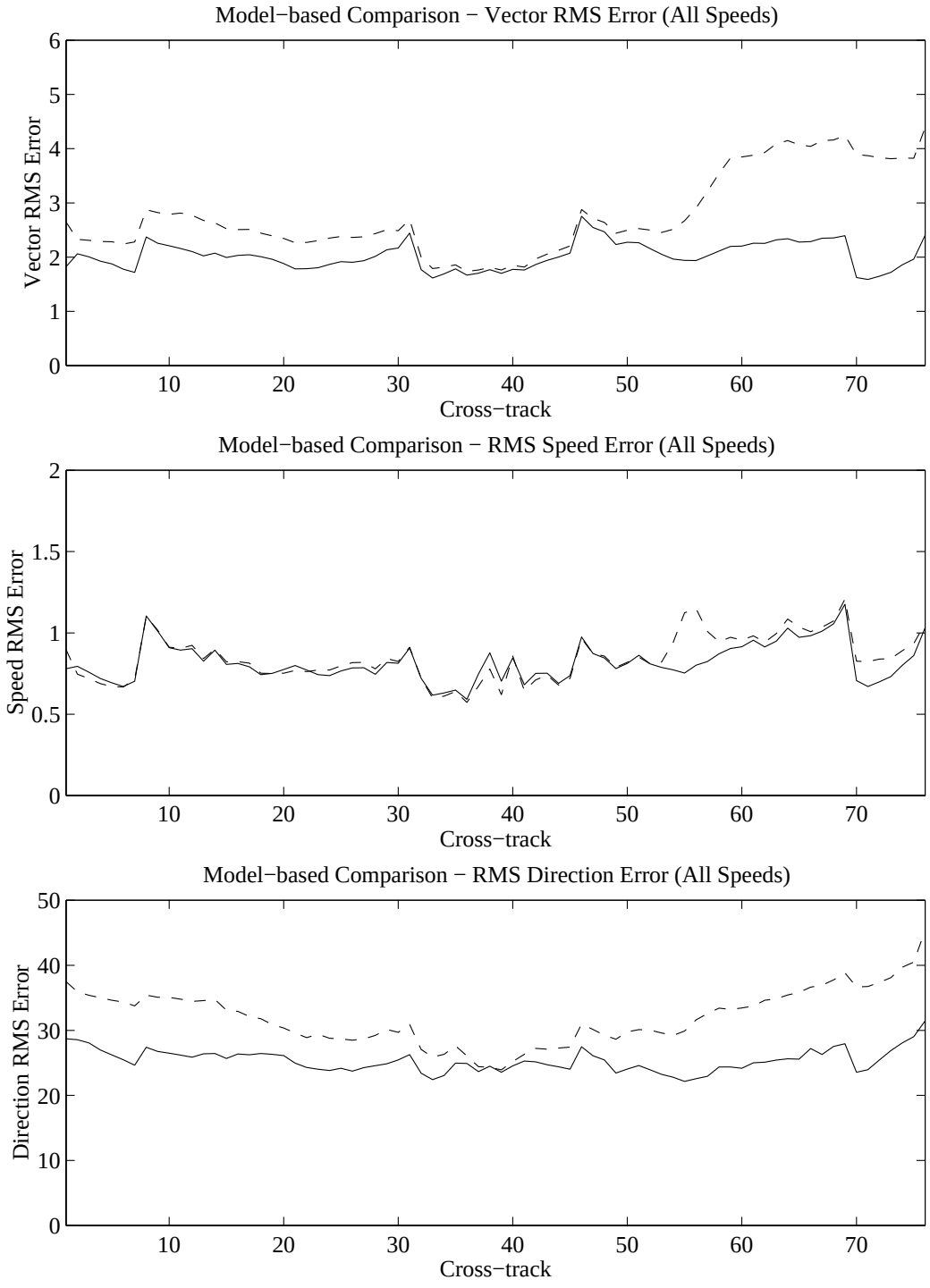

Figure 6.9: *RMS error as a function of the cross-track index for all wind speeds. This plot compares field-wise estimation with perfect ambiguity selection to the field-wise estimates using the ambiguity selection algorithm. The solid line represents perfect ambiguity selection while the dashed line includes ambiguity selection errors. These results were generated using interpolated NSCAT winds.*

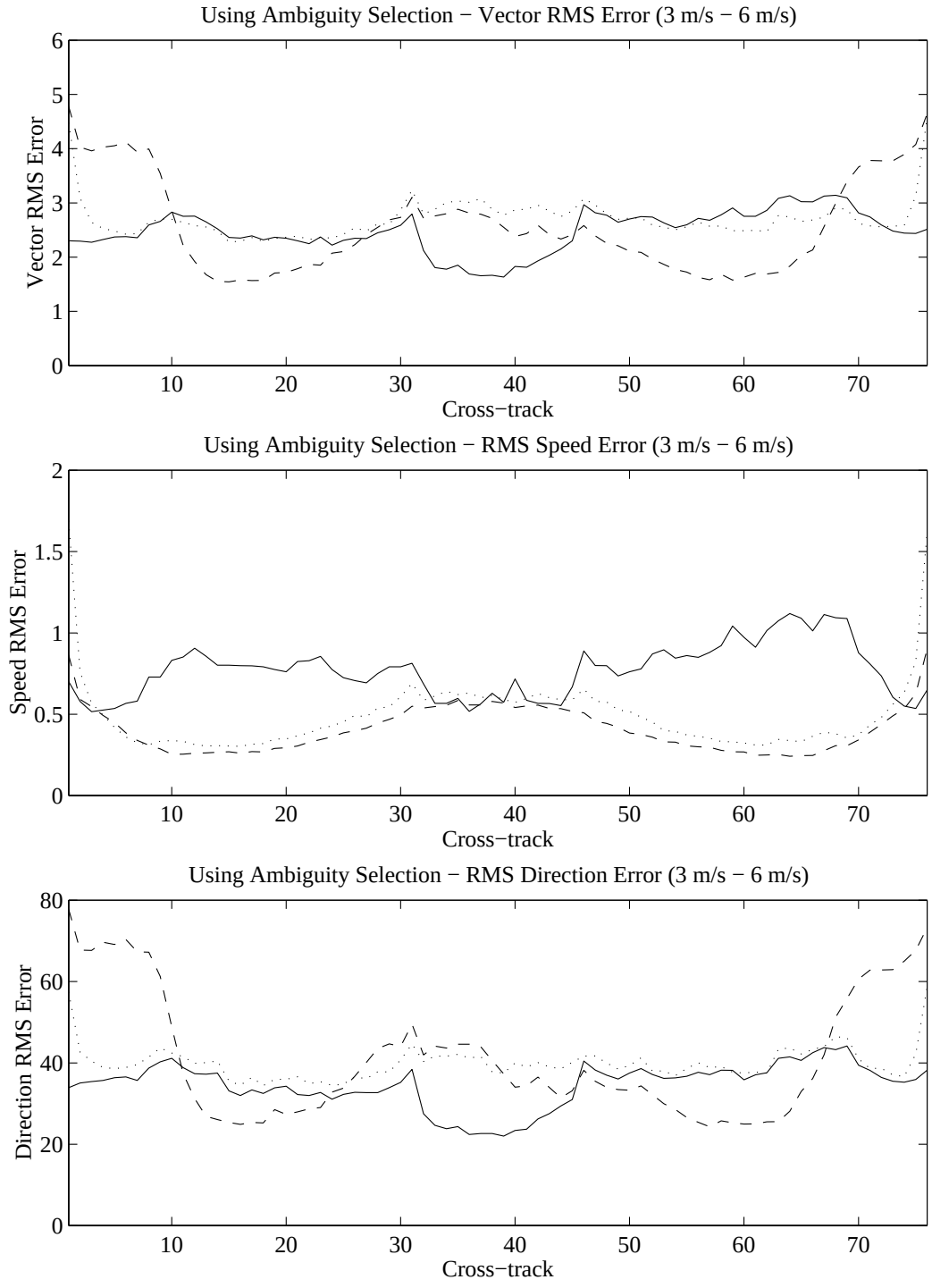

Figure 6.10: *RMS errors for the wind retrieval algorithms where errors from the ambiguity selection are included for winds with speeds between 3 and 6 m/s. The solid line represents the model-based estimate, the dotted line is the point-wise field closest to the model-based and the dashed line is the point-wise median filtered estimate. These results were generated using interpolated NSCAT winds.*

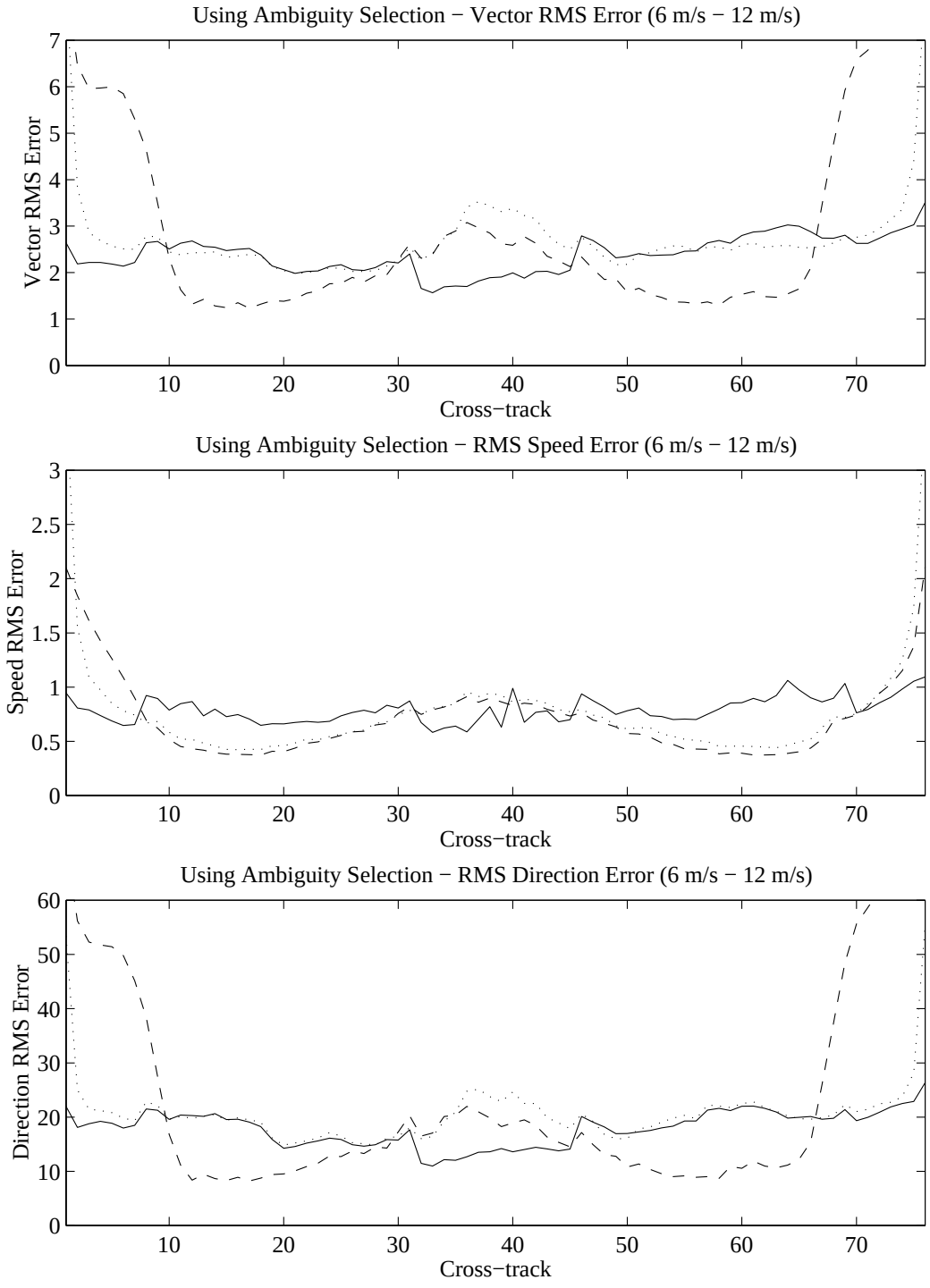

Figure 6.11: *RMS errors for the wind retrieval algorithms where errors from the ambiguity selection are included for winds with speeds between 6 and 12 m/s. The solid line represents the model-based estimate, the dotted line is the point-wise field closest to the model-based and the dashed line is the point-wise median filtered estimate. These results were generated using interpolated NSCAT winds.*

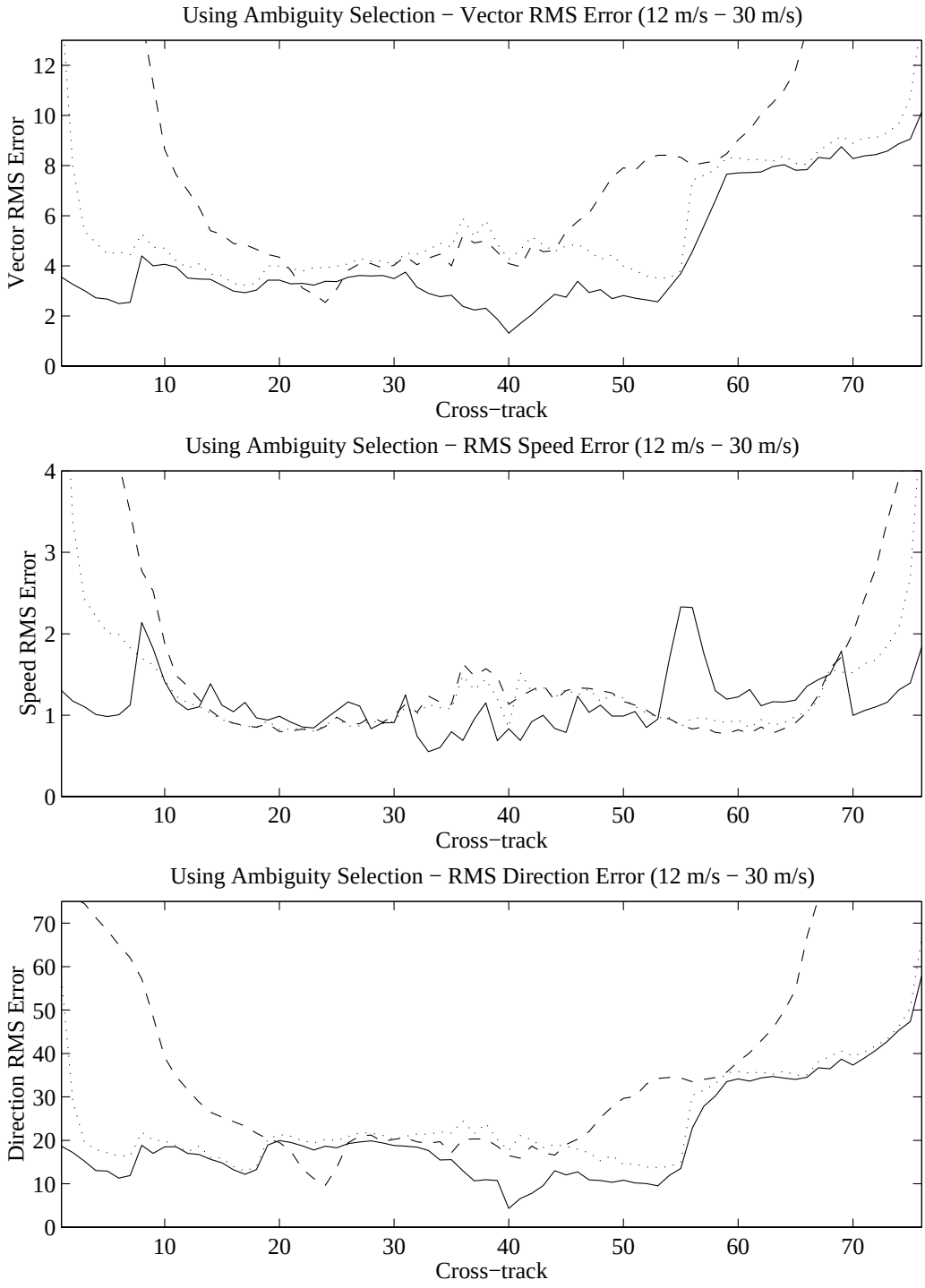

Figure 6.12: *RMS errors for the wind retrieval algorithms where errors from the ambiguity selection are included for winds with speeds between 12 and 30 m/s. The solid line represents the model-based estimate, the dotted line is the point-wise field closest to the model-based and the dashed line is the point-wise median filtered estimate. These results were generated using interpolated NSCAT winds.*

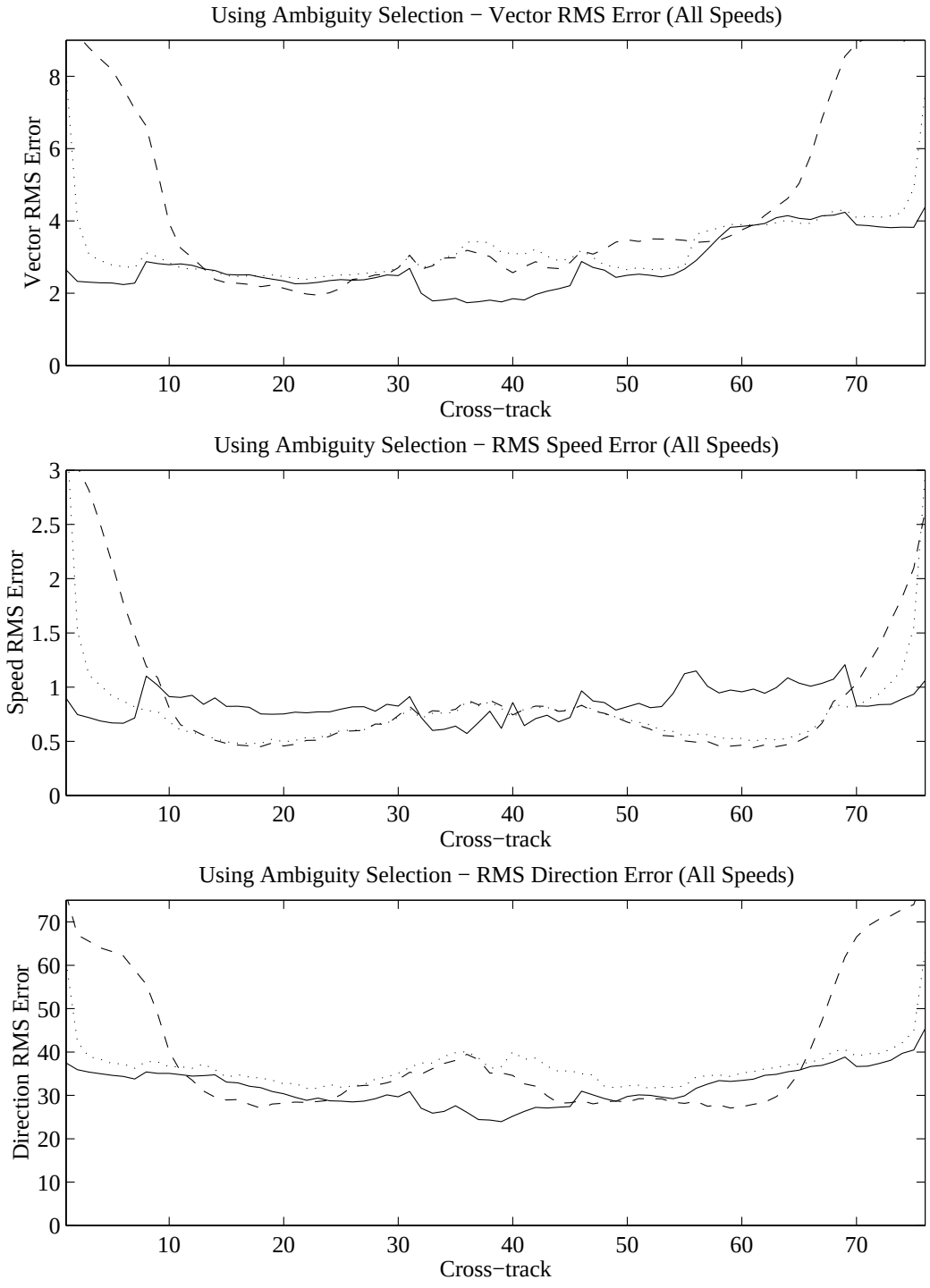

Figure 6.13: *RMS errors for the wind retrieval algorithms where errors from the ambiguity selection are included for winds all wind speeds. The solid line represents the model-based estimate, the dotted line is the point-wise field closest to the model-based and the dashed line is the point-wise median filtered estimate. These results were generated using interpolated NSCAT winds.*

Table 6.1: *The percentage of point-wise vectors closest to the true wind that are also closest to the field-wise estimate for interpolated NSCAT data.*

PW Skill for Interpolated NSCAT Winds		
FW Estimate	All Speeds	Speed > 4 m/s
Using the FWMF	92.3%	95.6%
Perfect Ambiguity Selection	94.1%	96.9%

6.3 Wind Retrieval Performance Using Modeled NSCAT Winds

A second algorithm evaluation is performed using the modeled NSCAT simulated wind fields. Unlike the interpolated NSCAT winds, which have highly variable wind in the regions where the wind is interpolated and smooth winds on the edge and in the gap where the wind is extrapolated, the modeled NSCAT winds have uniform variability across the swath. Because the modeled NSCAT wind fields have uniform variability the error metrics are also more consistent across the swath. The variability of the true wind is very important because it adversely affects the modeling error inherent in model-based estimation. Highly variable winds have large modeling errors when a model is fit to them. Conversely, smooth underlying winds result in less modeling error.

Figures 6.14-6.17 show the cross-track error for the field-wise, point-wise, and point-wise closest to field-wise estimates using perfect ambiguity selection. These plots represent the best estimate that can be achieved using each of the methods. Overall, the field-wise estimates contain less error than do the point-wise. In fact, the field-wise and point-wise results are almost equal in the sweet spot. This suggests that the error for model-base retrieval greater than the point-wise error using interpolated NSCAT winds (Figures 6.2-6.5) is primarily due to modeling error. Again the model-based errors remain nearly constant over all wind speeds groups while the point-wise errors increase.

The field-wise estimates created using the ambiguity selection algorithm are also compared with the estimates created using perfect ambiguity selection in Figures

6.18-6.21. The ambiguity removal consistently works well in the middle of the swath but the edges of the swath have errors very similar to the errors found in Figures 6.6-6.9. In fact, many of the WFRs with ambiguity selection errors are the same as in the previous tests. Most of the errors can be detected by visual inspection of the point-wise field closest to the model based estimate.

The field-wise estimates created using the FWMF are compared with the point-wise estimates generated using the first point-wise median filter and the point-wise field closest to the field-wise estimates in Figures 6.22-6.25. Overall, the field-wise estimate has the smallest RMS vector error. Also note that choosing the point-wise vector closest to the field-wise estimate improves the point-wise estimates. This further supports the notion that the field-wise winds may be a useful point-wise ambiguity selection tool.

The point-wise skill for field-wise estimates from modeled NSCAT data is given in Table 6.2. In spite of ambiguity selection errors the point-wise skill is 96.6% for wind vectors with speeds greater than 4 m/s.

Table 6.2: *The percentage of point-wise vectors closest to the true wind that are also closest to the field-wise estimate for modeled NSCAT data.*

PW Skill for Modeled NSCAT Winds		
FW Estimate	All Speeds	Speed > 4 m/s
Using the FWMF	93.1%	96.6%
Perfect Ambiguity Selection	94.9%	97.9%

6.4 Conclusions

Field-wise wind retrieval is shown to be potentially equal, and in some cases better, than conventional point-wise wind retrieval for SeaWinds data. However, for

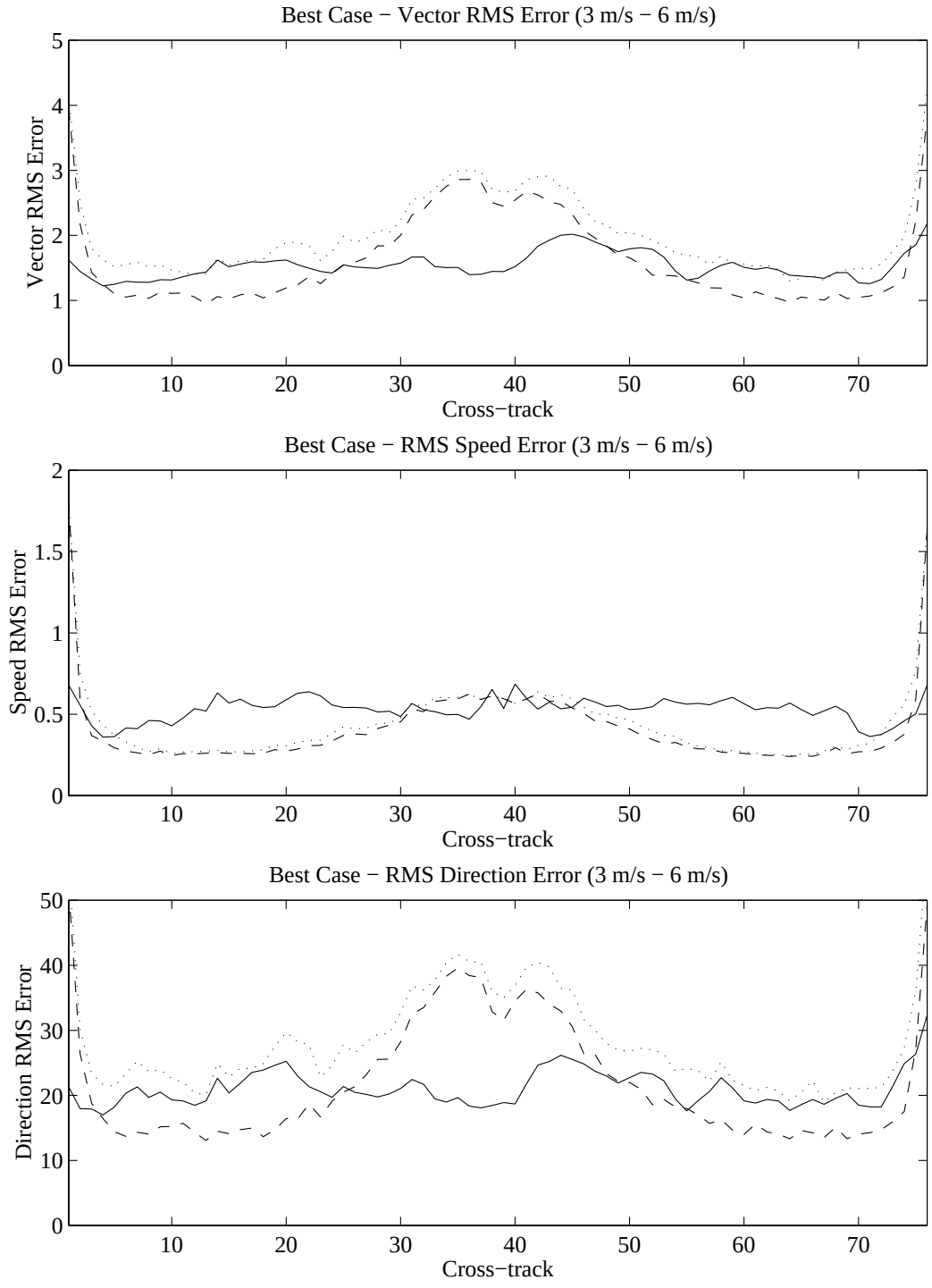

Figure 6.14: *RMS error as a function of the cross-track index for wind with speeds between 3 and 6 m/s. The solid line represents the model-based estimate, the dotted line is the point-wise field closest to the model-based and the dashed line is the point-wise alias closest to the true. These results were generated using modeled NSCAT winds.*

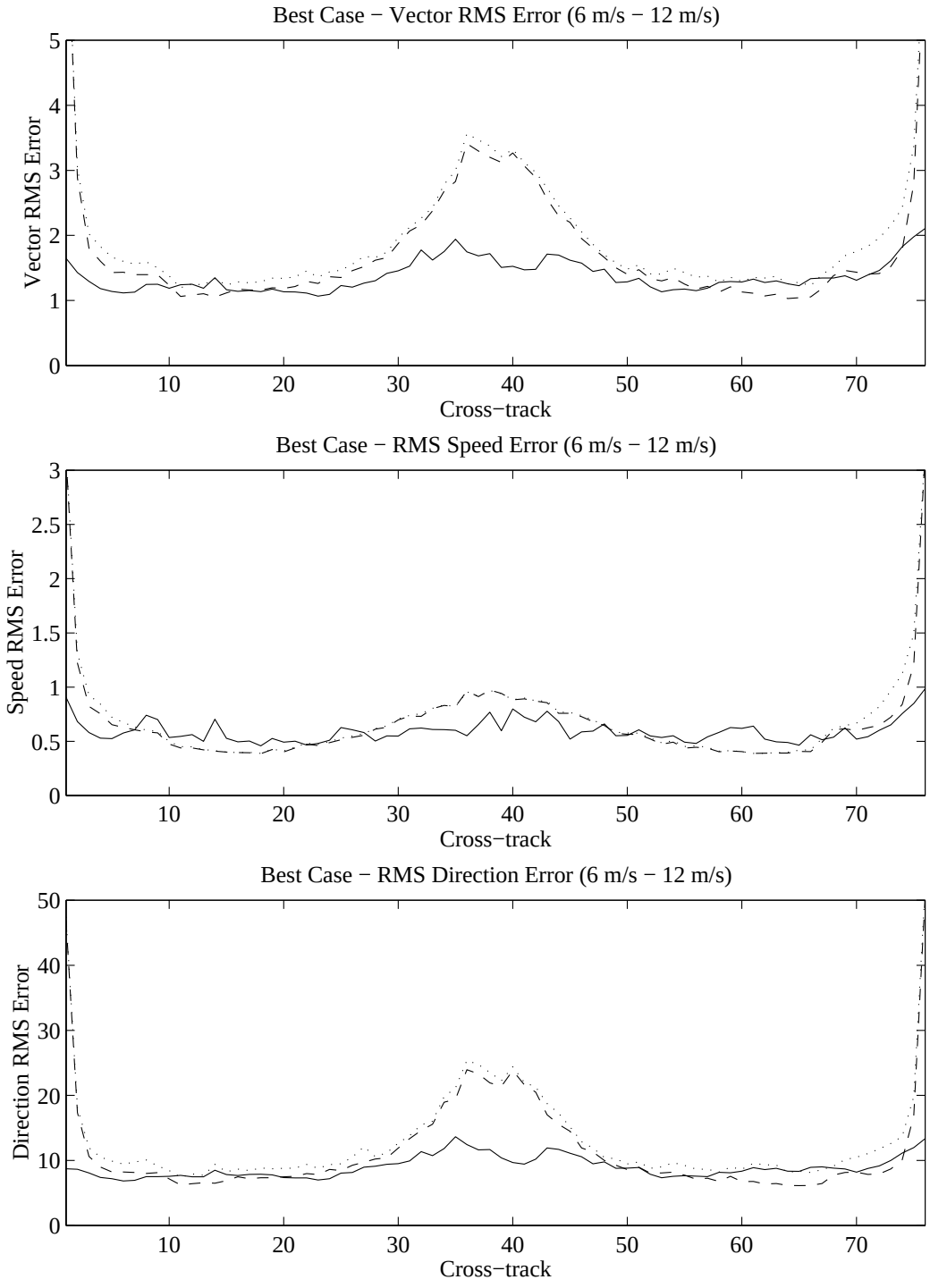

Figure 6.15: *RMS error as a function of the cross-track index for wind with speeds between 6 and 12 m/s. The solid line represents the model-based estimate, the dotted line is the point-wise field closest to the model-based and the dashed line is the point-wise alias closest to the true. These results were generated using modeled NSCAT winds.*

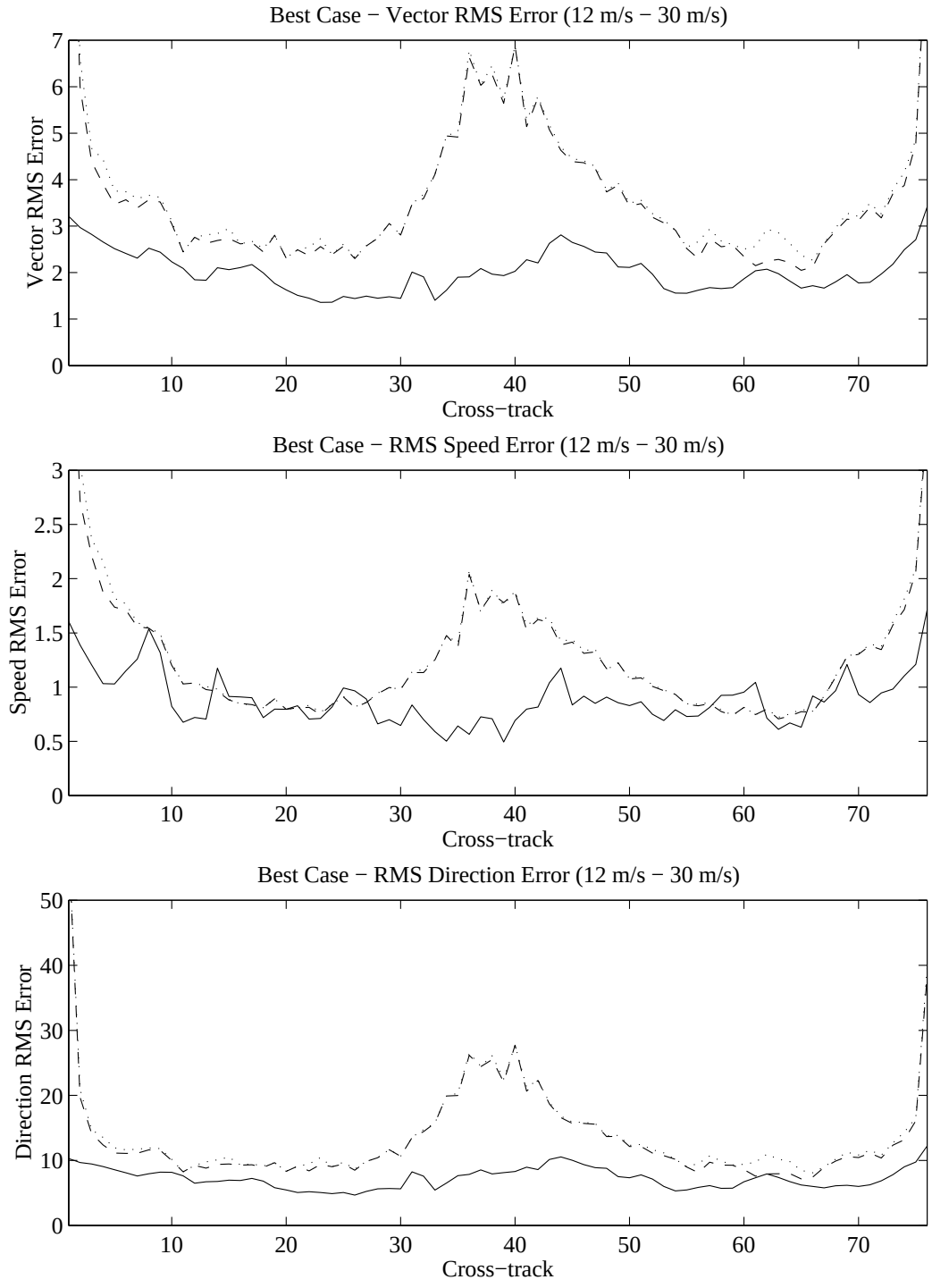

Figure 6.16: *RMS error as a function of the cross-track index for wind with speeds between 12 and 30 m/s. The solid line represents the model-based estimate, the dotted line is the point-wise field closest to the model-based and the dashed line is the point-wise alias closest to the true. These results were generated using modeled NSCAT winds.*

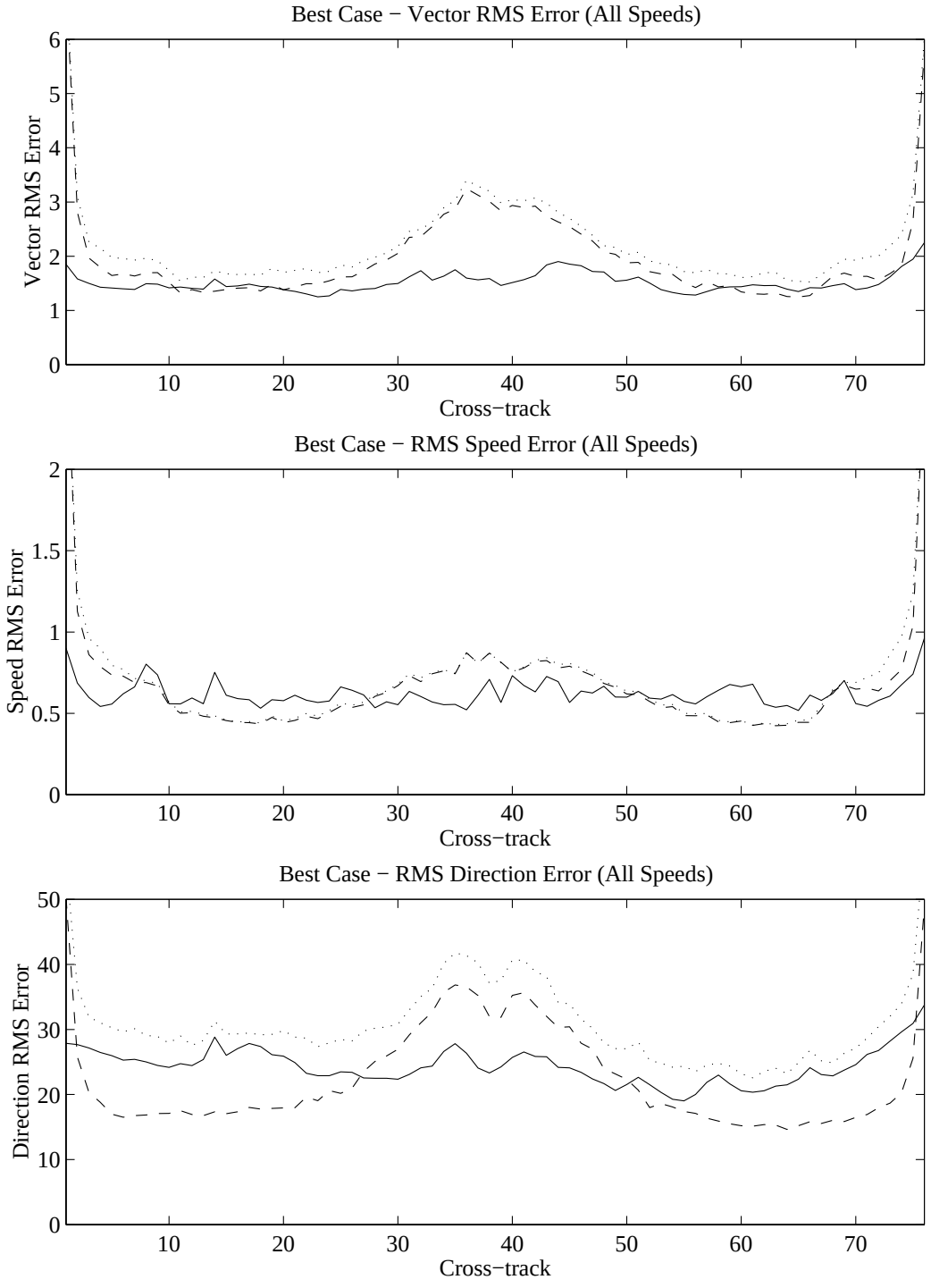

Figure 6.17: *RMS error as a function of the cross-track index for all wind speeds. The solid line represents the model-based estimate, the dotted line is the point-wise field closest to the model-based and the dashed line is the point-wise alias closest to the true. These results were generated using modeled NSCAT winds.*

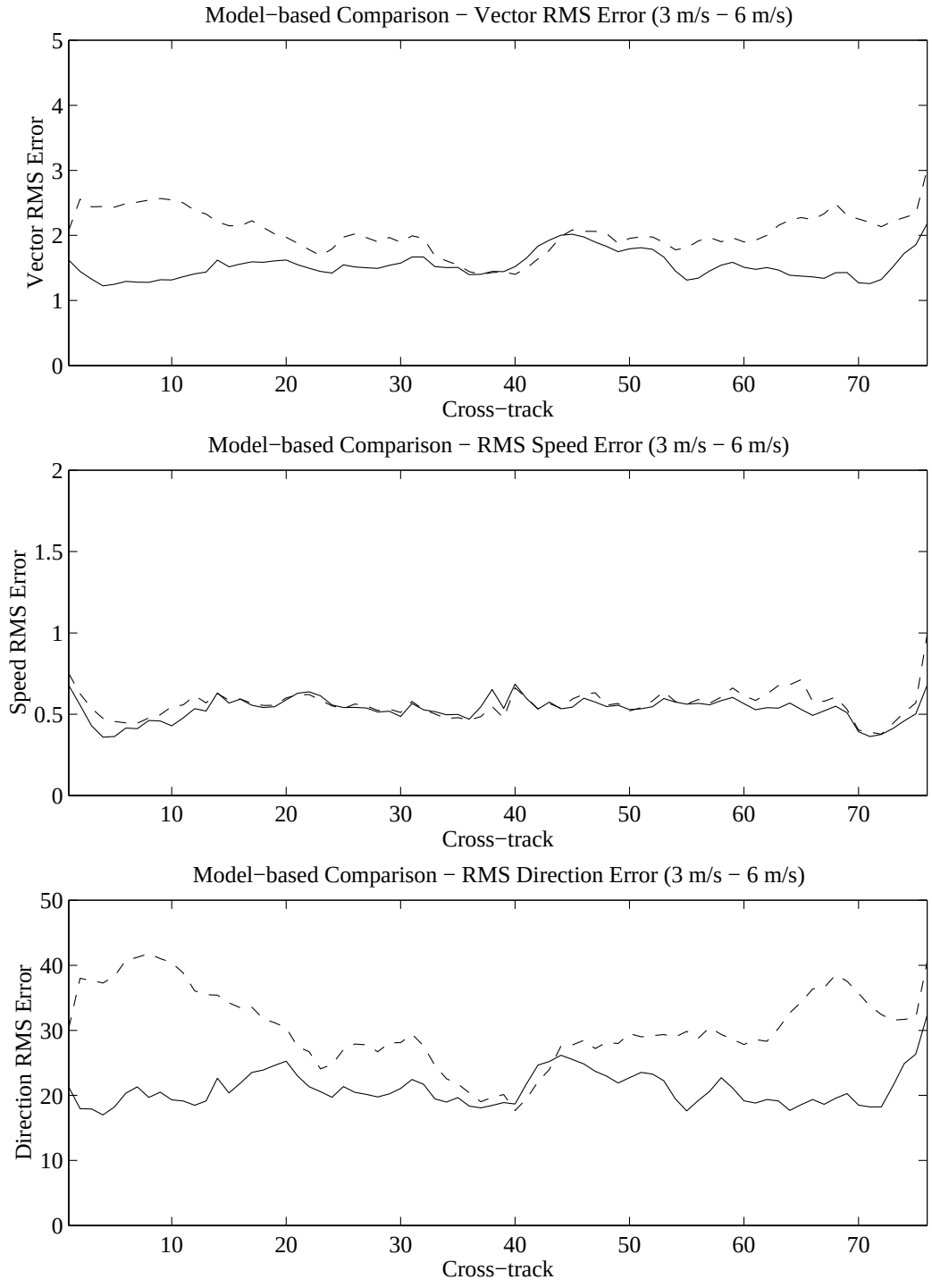

Figure 6.18: *RMS error as a function of the cross-track index for wind with speeds between 3 and 6 m/s. This plot compares field-wise estimation with perfect ambiguity selection to the field-wise estimates using the ambiguity selection algorithm. The solid line represents perfect ambiguity selection while the dashed line includes ambiguity selection errors. These results were generated using modeled NSCAT winds.*

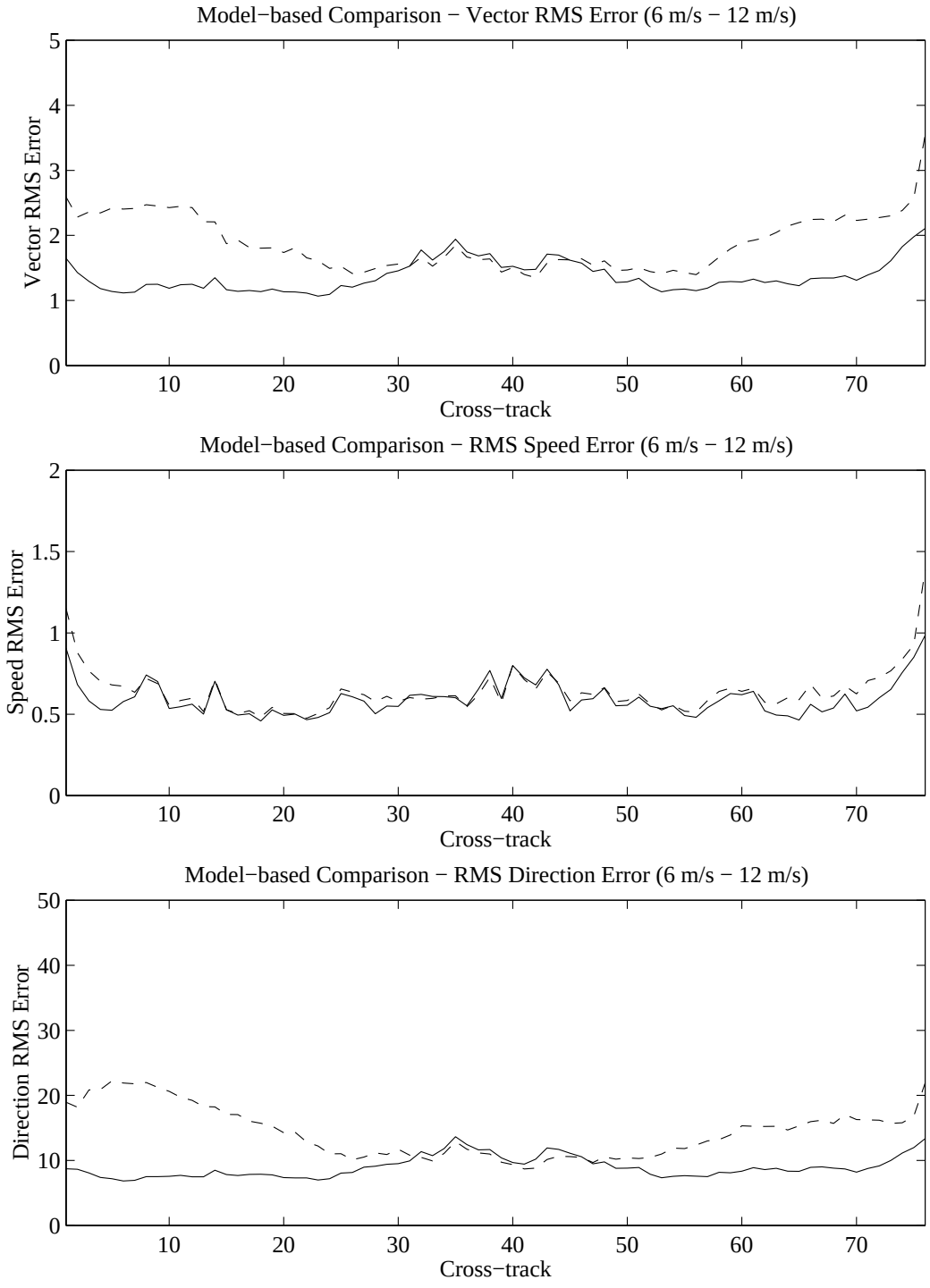

Figure 6.19: *RMS error as a function of the cross-track index for wind with speeds between 6 and 12 m/s. This plot compares field-wise estimation with perfect ambiguity selection to the field-wise estimates using the ambiguity selection algorithm. The solid line represents perfect ambiguity selection while the dashed line includes ambiguity selection errors. These results were generated using modeled NSCAT winds.*

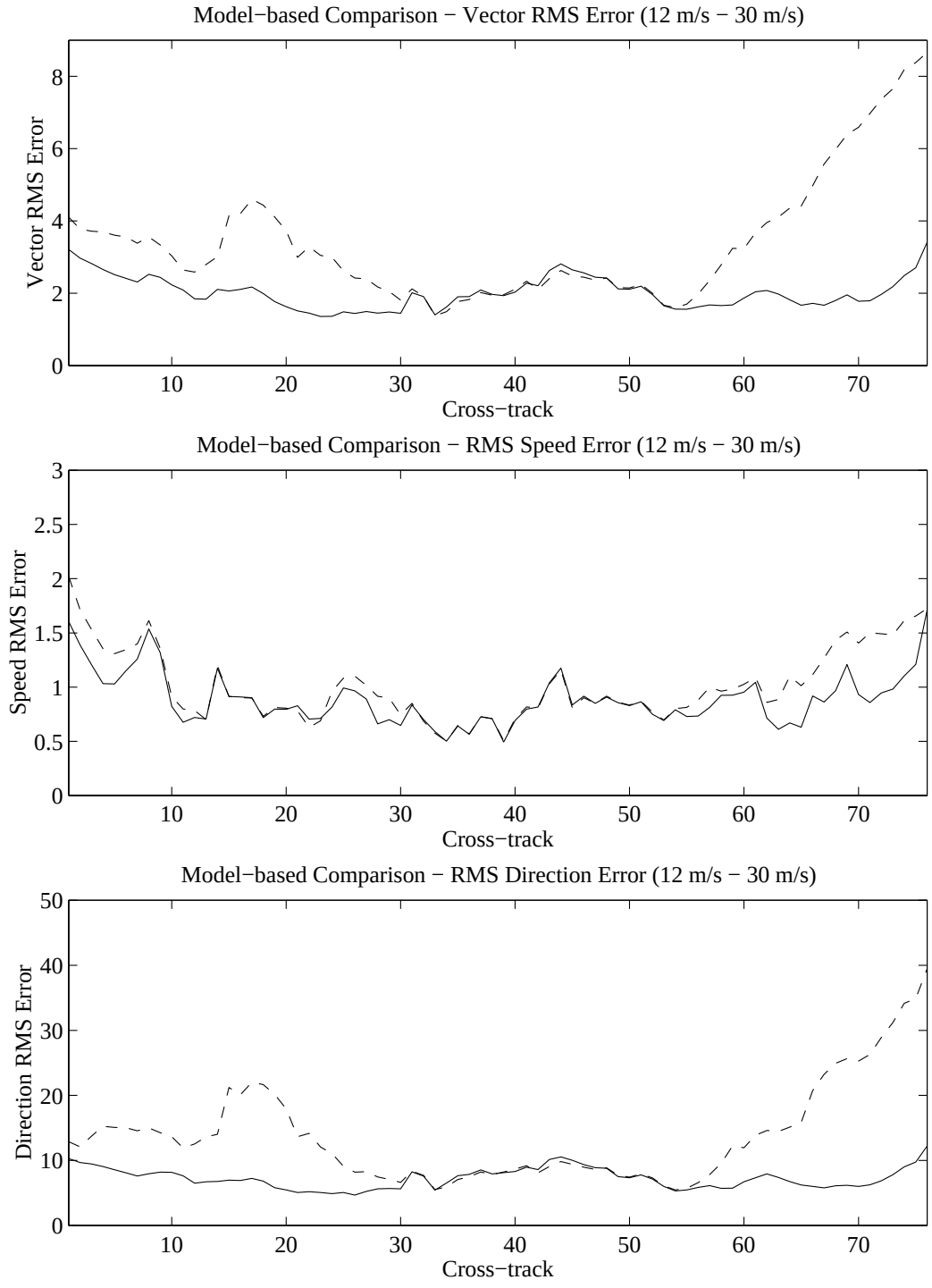

Figure 6.20: *RMS error as a function of the cross-track index for wind with speeds between 12 and 30 m/s. This plot compares field-wise estimation with perfect ambiguity selection to the field-wise estimates using the ambiguity selection algorithm. The solid line represents perfect ambiguity selection while the dashed line includes ambiguity selection errors. These results were generated using modeled NSCAT winds.*

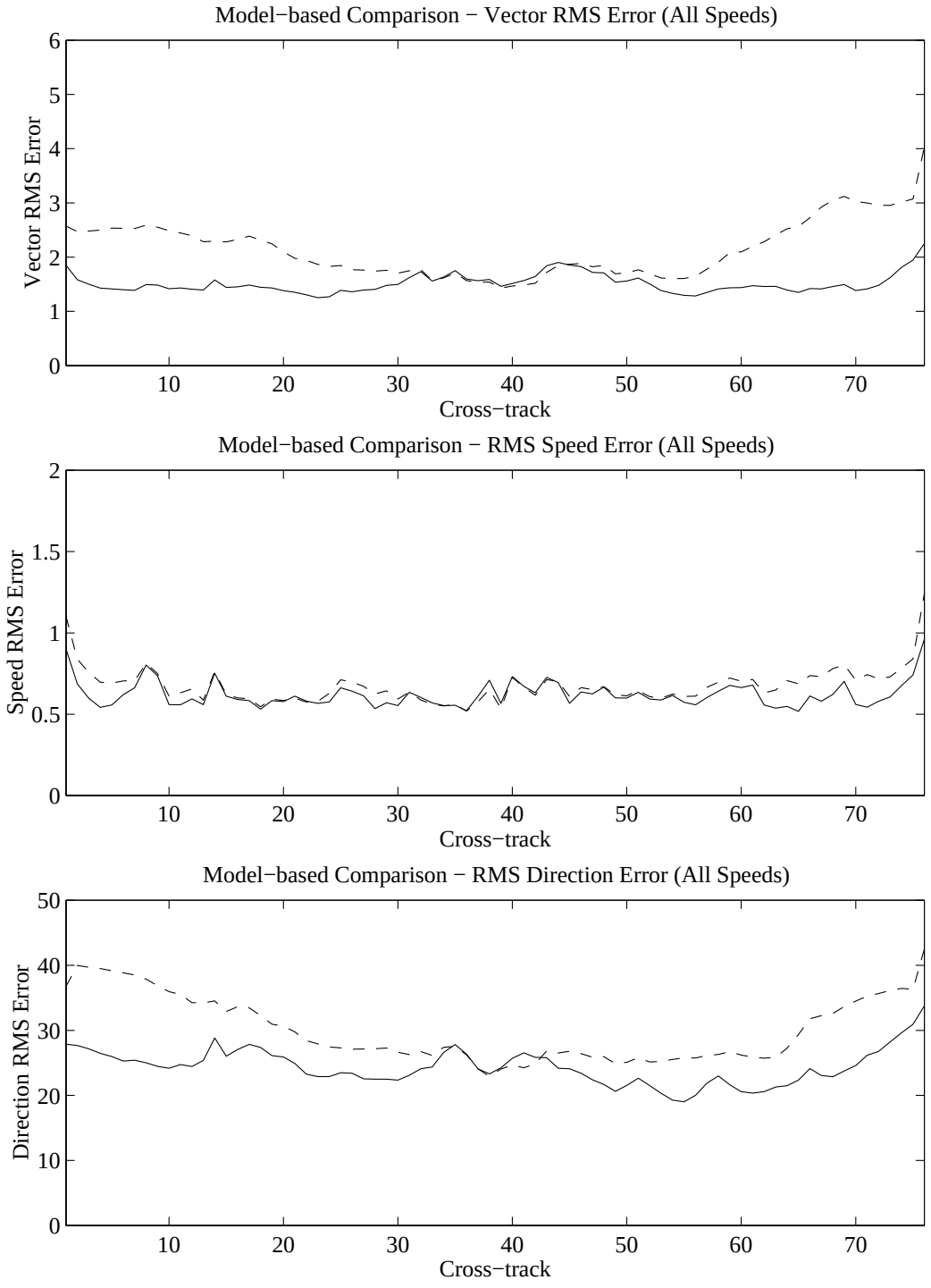

Figure 6.21: *RMS error as a function of the cross-track index for all wind speeds. This plot compares field-wise estimation with perfect ambiguity selection to the field-wise estimates using the ambiguity selection algorithm. The solid line represents perfect ambiguity selection while the dashed line includes ambiguity selection errors. These results were generated using modeled NSCAT winds.*

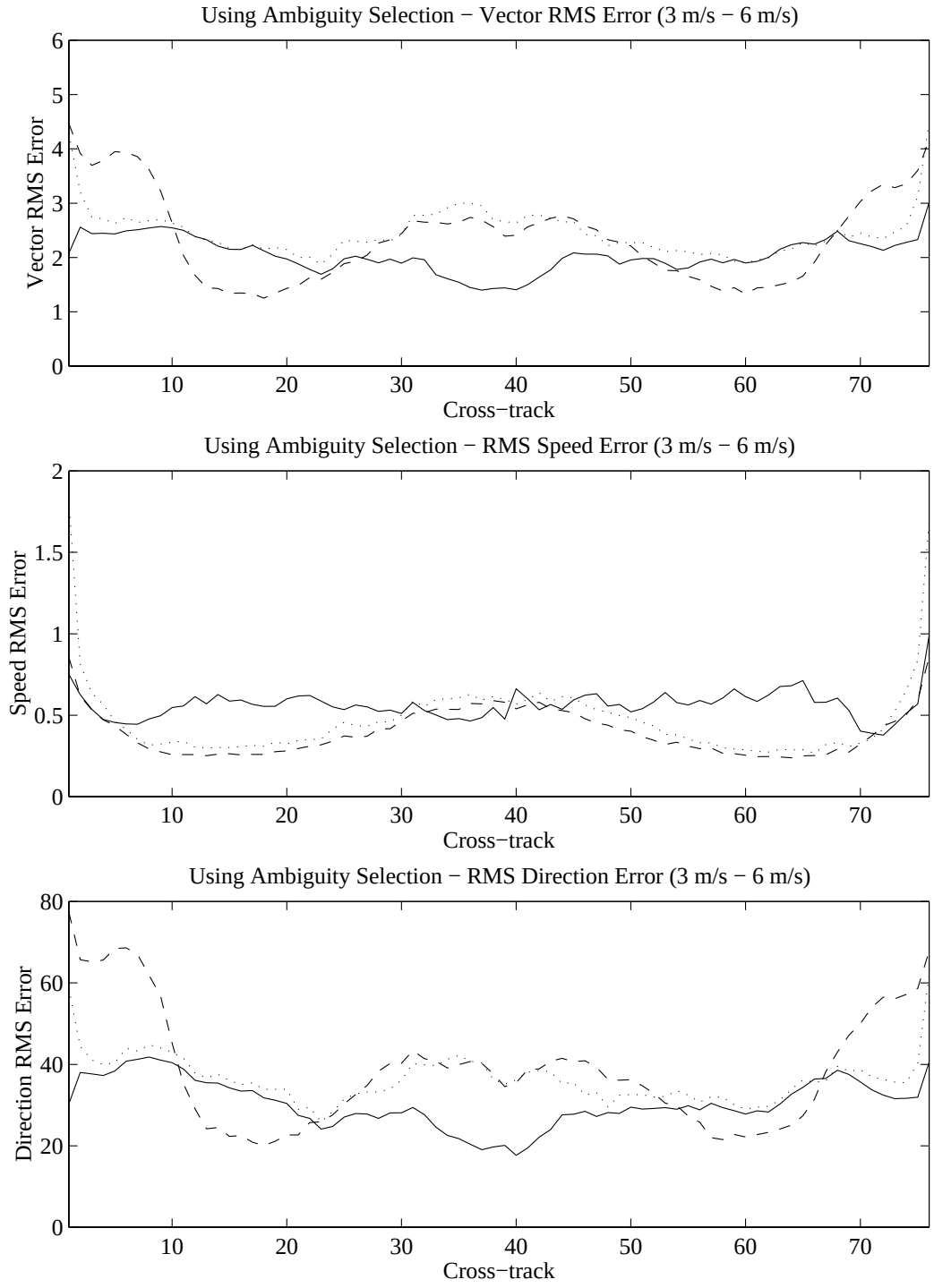

Figure 6.22: *RMS errors for the wind retrieval algorithms where errors from the ambiguity selection are included for winds with speeds between 3 and 6 m/s. The solid line represents the model-based estimate, the dotted line is the point-wise field closest to the model-based and the dashed line is the point-wise median filtered estimate. These results were generated using modeled NSCAT winds.*

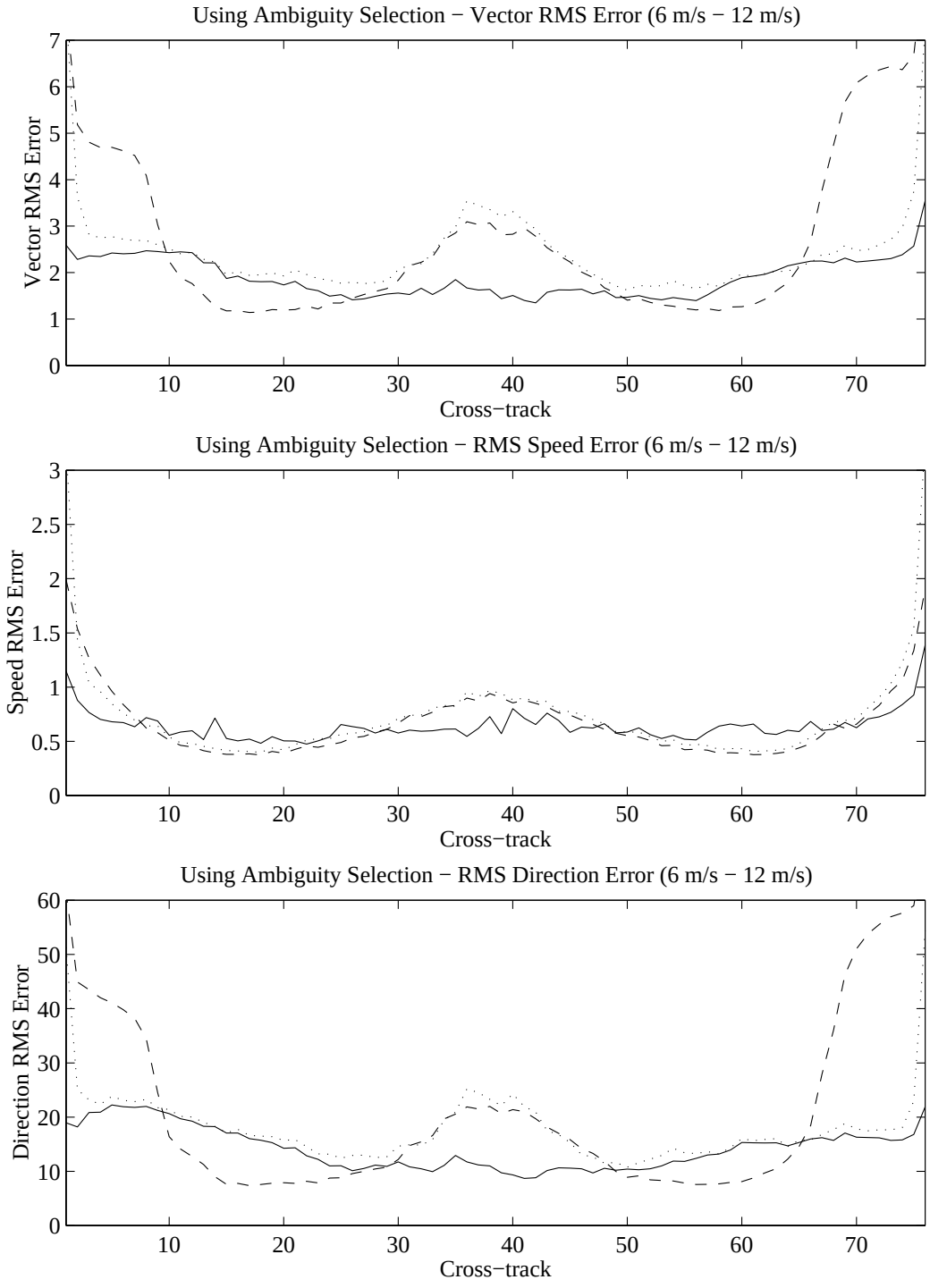

Figure 6.23: *RMS errors for the wind retrieval algorithms where errors from the ambiguity selection are included for winds with speeds between 6 and 12 m/s. The solid line represents the model-based estimate, the dotted line is the point-wise field closest to the model-based and the dashed line is the point-wise median filtered estimate. These results were generated using modeled NSCAT winds.*

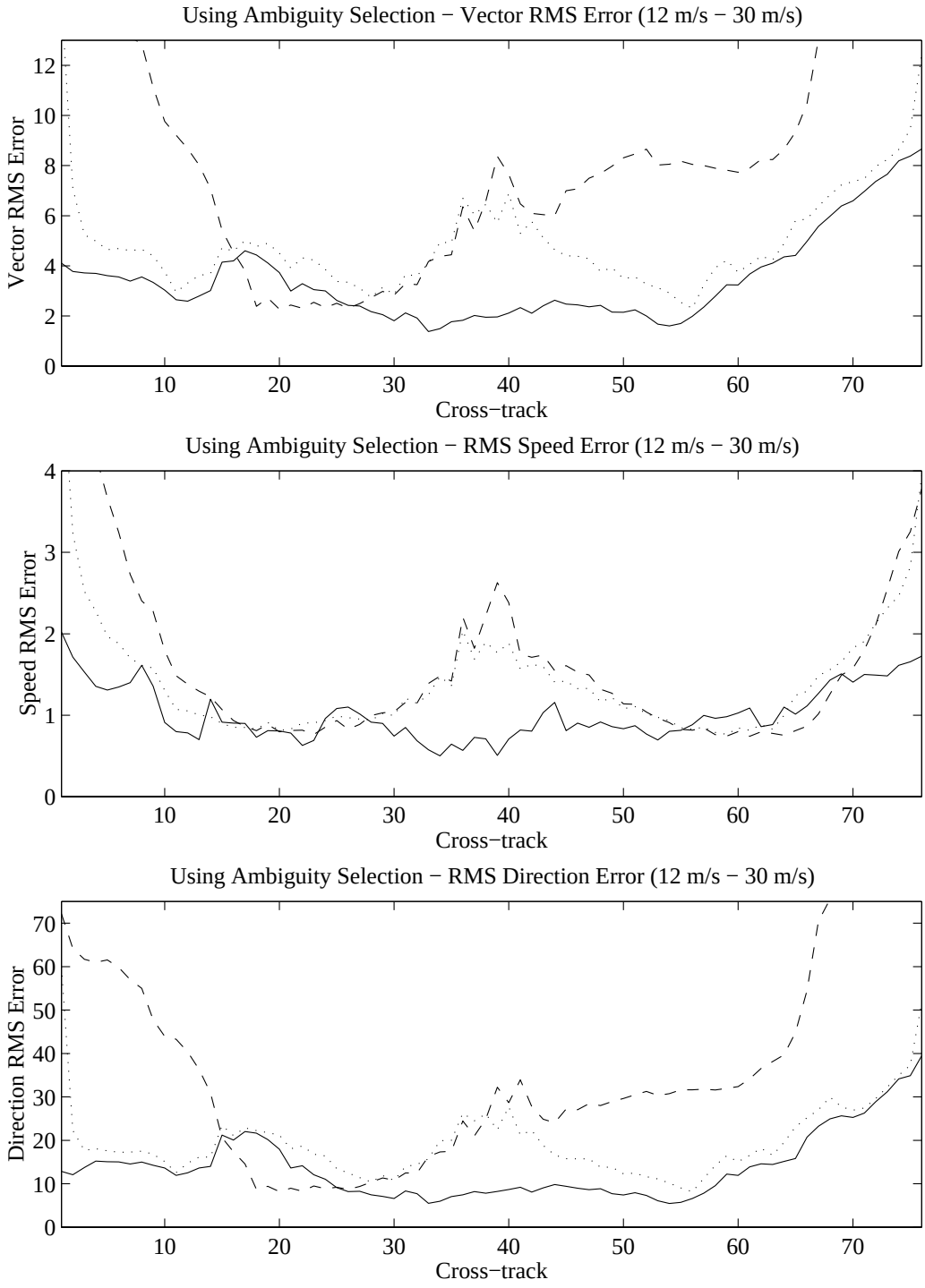

Figure 6.24: *RMS errors for the wind retrieval algorithms where errors from the ambiguity selection are included for winds with speeds between 12 and 30 m/s. The solid line represents the model-based estimate, the dotted line is the point-wise field closest to the model-based and the dashed line is the point-wise median filtered estimate. These results were generated using modeled NSCAT winds.*

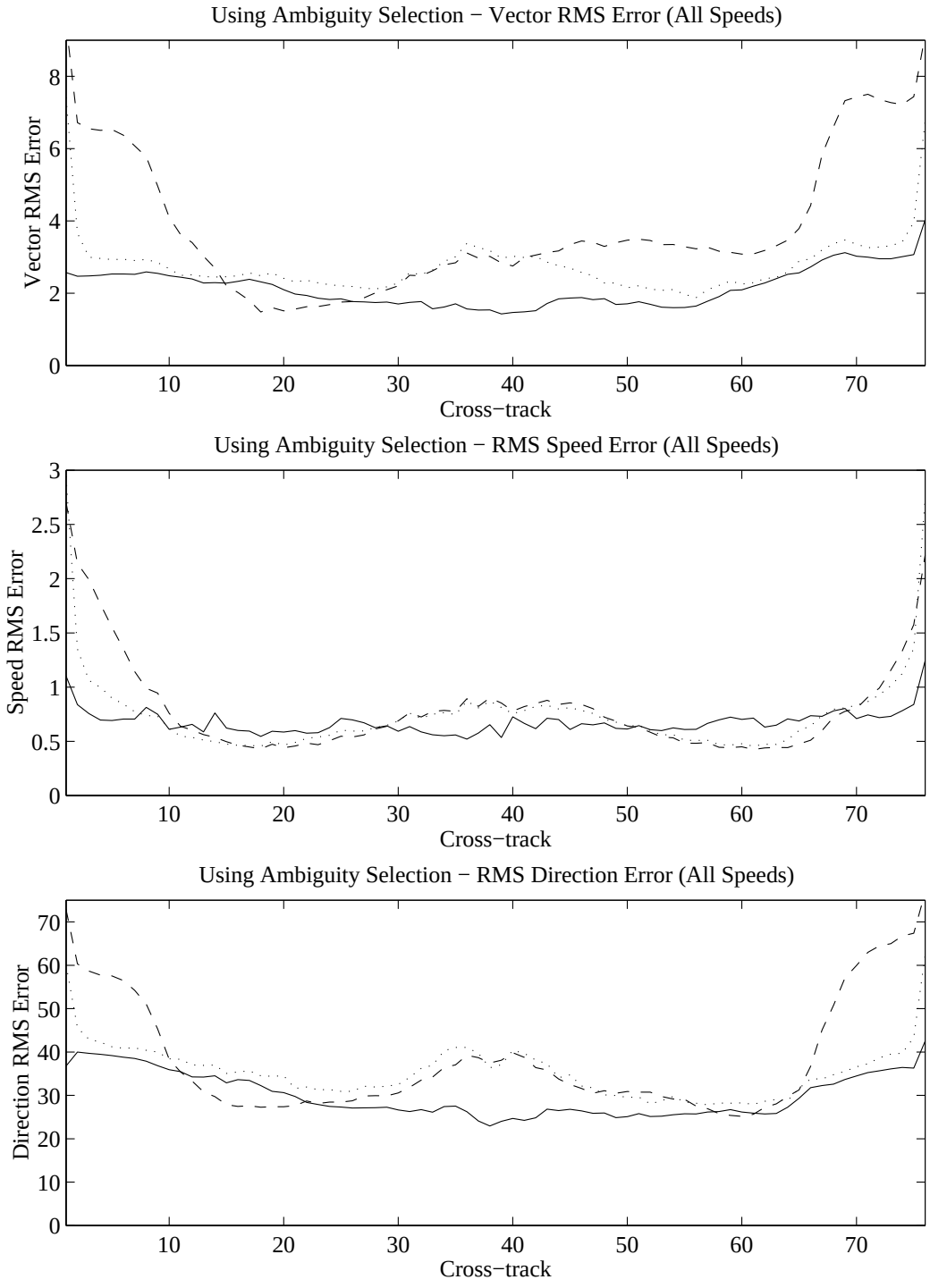

Figure 6.25: *RMS errors for the wind retrieval algorithms where errors from the ambiguity selection are included for winds all wind speeds. The solid line represents the model-based estimate, the dotted line is the point-wise field closest to the model-based and the dashed line is the point-wise median filtered estimate. These results were generated using modeled NSCAT winds.*

field-wise wind retrieval to be accurate enough to become a viable alternative to point-wise retrieval, the ambiguity removal must be improved. The results presented here were generated using a simplistic ambiguity removal technique. It is possible to use more complex algorithms and/or external data to improve the ambiguity removal. It should also be possible to develop an algorithm which detects and corrects ambiguity selection errors after the estimates are generated. With small improvements in the ambiguity selection, the field-wise estimates could be significantly better that the point-wise estimates.

In comparing the results using interpolated NSCAT winds and modeled NSCAT winds the effects of modeling error are shown. The potential accuracy of field-wise estimation is very dependent on the variability of the true wind. The results of field-wise estimation using the modeled NSCAT winds are 0.5 to 1.0 m/s better than field-wise estimates using interpolated NSCAT winds. This difference in error is largely attributed to modeling error. Thus if mesoscale surface ocean winds are believed to be quite smooth the field-wise estimate can be expected to be accurate. If the ocean winds are actually more variable, the estimation error is correspondingly larger.

Finally, the field-wise estimates are shown to be a good tool for point-wise ambiguity selection. With the field-wise ambiguity selection errors included, simply choosing the point-wise alias closest to the field-wise estimate results in 95.8% ambiguity selection accuracy for interpolated NSCAT data and 96.6% accuracy for modeled NSCAT data. As ambiguity selection improves, these numbers approach 96.9% and 97.9% respectively. Thus field-wise estimates have great potential to aid in point-wise ambiguity removal.

Chapter 7

Conclusion

SeaWinds is unique in that it uses a rotating pencil-beam antenna instead of a fixed fan-beam antenna. The rotating antenna results in varying measurement geometries across the swath. As a result, the wind estimation techniques used for processing NSCAT data do not work well with SeaWinds data. This thesis develops a field-wise approach to wind estimation in an effort to improve the overall accuracy of SeaWinds estimates.

7.1 Summary

Before developing a field-wise wind retrieval algorithm, simulated SeaWinds data sets must first be generated so the algorithm may be tested. In this thesis three methods for simulating wind fields are presented. The first uses filtered Gaussian noise to synthesize wind fields with the same spectral characteristics as ocean winds. Another method uses wind field estimates from the NSCAT data sets. These estimates contain realistic phenomenological wind features but cover a smaller area and have missing data points. Thus the NSCAT wind fields must be interpolated to fill a SeaWinds swath. The interpolation is performed using an optimal interpolation based on the autocorrelation of the wind. By interpolating the NSCAT winds, a continuous swath of ocean winds is created. One potential drawback of these winds is that the NSCAT estimates contain noise while the interpolated sections of the field are quite smooth. The final form of simulated wind uses a model fit to the interpolated NSCAT wind fields to further smooth the wind creating a swath of wind with uniform variability across the swath. These winds are referred to as modeled NSCAT winds.

The field-wise approach to wind estimation uses linear wind field models to model the correlation in the wind from measurement cell to measurement cell. This is different than point-wise estimation which only estimates the wind in a single cell independent of data in the surrounding cells. A single field-wise or model-based estimate contains wind speeds and directions for an entire region. The regions used in this field-wise algorithm are comprised of 24×24 wind vector cell fields corresponding to 600×600 km areas of the ocean's surface.

The first stage of the field-wise wind retrieval algorithm is field-wise estimation. This stage takes the σ^o measurements and generates a set of possible wind fields that correspond to the measurements. These possible wind fields, or aliases, are generated when searching the objective function. For SeaWinds data the maximum likelihood objective function is shown to perform better than a constrained objection function and the augmented multi-start search is shown to be a good method for searching the objective function. A test of 1060 regions shows that this objective function and search routine locate the alias closest to the true wind 96% of the time. The 22 parameter KL model is shown to be the best sized wind field model for field-wise estimation because it provides the best tradeoff between modeling error and computational complexity.

Once the set of possible wind field aliases has been generated, the one closest to the true wind must then be selected from the set. This step in the estimation process is known as ambiguity selection. A field-wise median filter (FWMF) is presented which uses many of the same principles behind the point-wise median filter (PWMF) used in NSCAT ambiguity selection. Once the estimate for the entire wind field is generated using the FWMF a point-wise nudging technique is developed to further improve the estimate using information from the point-wise estimates. On a test case

of 1060 regions these two methods used together select good aliases for 95% of the regions.

Last of all, the field-wise estimation and field-wise ambiguity removal algorithms are combined to form an end-to-end field-wise wind retrieval algorithm. This algorithm is tested on several swaths of interpolated NSCAT winds and modeled NSCAT winds to gauge the overall wind estimation performance. Using the interpolated NSCAT winds the field-wise wind retrieval algorithm worked comparably to the performance of the point-wise estimates. Using the modeled NSCAT winds the field-wise performance increases due to smaller modeling error resulting from the smoother simulated wind field. In this case the field-wise estimation is superior to the point-wise results. Overall, the field-wise estimates compare very well with point-wise results and show the potential of being significantly better with improved ambiguity selection.

7.2 Contributions

In developing an end-to-end field-wise wind retrieval algorithm, four major contributions are made to the field of scatterometer-based wind retrieval. The first contribution is the derivation of a specialized interpolation algorithm for interpolating ocean wind fields. This interpolation scheme uses the autocorrelation of the wind in conjunction with linear wind field model to produce a weighted MAP least squares fit to the data. This form of the least squares fit can then be used to project wind fields into regions where there is no data.

The next contribution is the extension of the field-wise techniques, developed by [3] for NSCAT data, to SeaWinds data. The augmented multi-start global optimization is shown to provide the best search over the maximum likelihood (ML) objective function. The ML objection function is also shown to produce more accurate estimates than a constrained objective function. The last extension is the use of 24×24 wind vector cell models which covers an area four times larger that the 12×12 models used in [3]. The 22 parameter 24×24 KL is shown to provide the best tradeoff between modeling error and computational complexity.

In order to perform field-wise ambiguity selection a field-wise median filtering technique is developed. This technique is modeled after the point-wise median filter used in NSCAT ambiguity selection [9], [10]. The FWMF does a very good job of determining the general wind flow using only the field-wise aliases; however, the results are not quite accurate enough to be used in wind estimation. To further increase the performance of the FWMF a nudging technique is developed which uses information from the point-wise estimates. These two techniques used together select a good alias 95% of the time. It is also shown that the performance of the FWMF can be improved if external wind estimates, such as the output of numerical weather prediction models, are used to nudge the wind estimates.

The final contribution is the combination of field-wise estimation techniques with the field-wise ambiguity selection algorithm to form an end-to-end field-wise wind retrieval algorithm which uses only scatterometer data in generating unique wind estimates. The overall performance of this algorithm is evaluated in Chapter 6 and is shown to estimate the wind with accuracy comparable to, and in some cases better than, the point-wise estimates.

7.3 Future Work

As mentioned, the results of this algorithm are comparable to the estimates provided by point-wise wind retrieval. However, in order for field-wise retrieval to become a viable alternative to point-wise retrieval additional improvements must be made.

The primary source of error in this algorithm is in the field-wise ambiguity selection stage. Because the performance of the FWMF is so dependent on the accuracy of the initial field, the best way to improve ambiguity selection performance is to improve the initial values of the FWMF. One way to do this is to choose the initial wind field aliases as the ones closest to numerical weather predictions for the wind at the time the measurements are taken. Doing this ensures that the initial field for the FWMF has consistent flow, improving the ambiguity selection.

Even with numerical models nudging the initial values for the FWMF, ambiguity selection errors are inevitable. In Chapter 5 it is shown that these errors are easily distinguished using the field of point-wise aliases closest to the field-wise estimate of the wind field. Therefore, an ambiguity selection error detection and correction algorithm can be developed using the point-wise fields closest to the field-wise estimates. This algorithm could conceivably use the same principles used by [21] to correct ambiguity selection errors for NSCAT point-wise winds. The detection could also use edge detection algorithms based on the directions of the point-wise aliases closest to the field-wise estimate because ambiguity selection errors are manifest by sudden changes, usually 90° to 180°, in the wind direction.

The next step in creating an operational field-wise estimation algorithm is to obtain actual σ^o data from JPL. This is not yet available but should give the best evaluation of the field-wise estimation performance. Once these data sets are processed they can then be compared directly with the results of the JPL point-wise wind retrieval algorithms.

Bibliography

[1] M. Spencer, C., and D. G. Long, "Tradeoffs in the design of a spaceborne scanning pencil beam scatterometer: Application to SeaWinds", *IEEE Transaction on Geoscience and Remote Sensing*, vol. 35, pp. 115–126, January 1997.

[2] F. Naderi, M. Freilich, and D. G. Long, "Spaceborne radar measurement of wind velocity over the ocean—an overview of the NSCAT scatterometer system", *Proceedings of the IEEE*, vol. 79, no. 6, pp. 850–866, June 1991.

[3] C. G. Brown, "A field-wise wind retrieval algorithm for the NASA scatterometer", Master's thesis, Brigham Young University, September 1998.

[4] F. T. Ulaby, R. K. Moore, and A. K. Fung, *Microwave Remote Sensing*, vol. 2, Artech House Inc., Norwood, MA, 1981.

[5] D. M. Swingle, "Weather radar in the United States army's Fort Monmoth laboratories", in *Radar in meteorology: Battan Memorial and 40th Anniversary Radar Meteorology Conference*, David Atlas, Ed., 1990.

[6] F. Wentz and D. Smith, "A model function for ocean normalized radar cross section at 14.6 GHz derived from NSCAT observations", *in press, Journal of Geophysical Research*, 1998.

[7] T. E. Oliphant, "New techniques for wind scatterometry", Master's thesis, Brigham Young University, August 1996.

[8] P. Johnson, *Uncertainties in Oceanic Microwave Remote Sensing: The Radar Footprint, The Wind-Backscatter Relationship, and the Measurement Probability Density Function*, PhD thesis, Brigham Young University, 1999.

[9] H. Shultz, "A circular median filter approach for resolving directional ambiguities in wind fields retrieved from spaceborne scatterometer data", *Journal of Geophysical Research*, vol. 95, pp. 5291–5303, 1990.

[10] S. J. Shaffer, R. S. Dunbar, S. V. Hsiao, and D. G. Long, "A median-filter-based ambiguity removal algorithm for NSCAT", *IEEE Transactions on Geoscience and Remote Sensing*, vol. 29, no. 1, 1991.

[11] D. G. Long, "Wind field model-based estimation of Seasat scatterometer winds", *Journal of Geophysical Research*, vol. 98, no. C8, pp. 14651–14668, August 1993.

[12] A. K. Jain, *Fundamental of Digital Image Processing*, Prentice Hall, New Jersey, 1989.

[13] M. H. Freilich and D. B. Chelton, "Wavenumber spectra of Pacific winds measured by the Seasat scatterometer", *Journal of Physical Oceanography*, vol. 16, no. 4, pp. 741–757, April 1986.

[14] Y. Feliks, E. Gavze, and R. Givati, "Optimal vector interpolation of wind fields", *Journal of Applied Meteorology*, pp. 1153–1165, 1996.

[15] P. Cervenka and C. de Moustier, "Interpolation and filtering of spatial observations using successive corrections and Gaussian filters", *IEEE Journal of Oceanic Engineering*, pp. 619–29, 1994.

[16] R. F. Stengel, *Stochastic Optimal Control: Theory and Application*, Wiley, 1986.

[17] C. G. Brown, "A MAP estimate for modeled winds", BYU MERS Internal Report, 1997.

[18] J. G. Proakis, C. M. Rader, F. Ling, and C. L. Nikias, *Advanced Digital Signal Processing*, Macmillan Publishing Company, 1992.

[19] A. E. Gonzales, "An assessment of the NASA scatterometer ambiguity removal technique", Master's thesis, Brigham Young University, May 1998.

[20] K. V. Mardia, *Statistics of Directional Data*, New York: Academic, 1972.

[21] A. E. Gonzales and D. G. Long, "An assessment of NSCAT ambiguity removal", *in press, Journal of Geophysical Research*, 1999.